Development and Electronic Phenomena of Etched Bulk-Insulating Topological Insulator Nanowires

INAUGURAL-DISSERTATION

zur
Erlangung des Doktorgrades
der Mathematisch-Naturwissenschaftlichen Fakultät
der Universität zu Köln

vorgelegt von

M.Sc. M.Sc. Matthias E. Rößler

aus Düsseldorf

Köln, 2023

DEVELOPMENT AND ELECTRONIC PHENOMENA OF ETCHED BULK-INSULATING TOPOLOGICAL INSULATOR NANOWIRES

DISSERTATION

Matthias E. Rößler

Faculty of Mathematics and Natural Sciences - University of Cologne

First examiner: Prof. Dr. Yoichi Ando
Second examiner: Prof. Dr. Erwann Bocquillon

Chairman of the examination committee: Prof. Dr. Alexander Altland

Development and Electronic Phenomena of Etched Bulk-Insulating Topological Insulator Nanowires
University of Cologne
Institute of Physics II
Faculty of Mathematics and Natural Sciences
Zülpicher Str. 77, 50937 Cologne, Germany

PREFACE

Long before the completion of this Dissertation titled 'Development and Electronic Phenomena of Etched Bulk-Insulating Topological Insulator Nanowires' it was envisioned to be about the fabrication and evaluation of qubits based on Majorana fermions. Although the topics are linked, the unexpected different learnings presented in this work are just as interesting to me as the initial idea, partly because they serve as an example of how science and maybe life is an endeavour whose final destination is rarely as envisioned, but an endeavour that can bear other totally unforeseen fruit.

Coming from a background that combines materials science and physics, I came to cherish both worlds, the tantalizing theoretical descriptions of physics that describe almost magical manifestations of nature as well as the sometimes challenging but always promising reality of novel quantum materials. Research guided by both enables to aspire to potentially world-changing long-term goals, but at the same time allows to find many exciting surprises along the way. In this sense, the results presented in this work stand in a broad context of Majorana research and topological quantum computation, but actually focus on foundations and findings during the journey, namely electronic phenomena in topological insulator nanowires such as a giant magnetochiral anisotropy. May this work serve other scholars full of curiosity and pioneering spirit as a stepping stone.

Matthias Rößler
Castelvecchio (Pescia), September 2023

Contents

ABSTRACT

Topological quantum matter serves as a fertile ground to study novel transport phenomena as well as fundamental aspects of modern condensed matter physics since about two decades. More recently it was realized that topological insulator nanowires (TINWs) that exhibit quantum-confined topological surface states (TSS) with peculiar spin-physics can, when proximitized by a superconductor, harbour exotic quasi-particles with non-abelian exchange statistics called Majorana bound states (MBS), which are of great fundamental and technological interest [1].

In this work, a TINW platform was developed and experimentally investigated that provides the necessary ingredients to realize next-generation proposals to study and manipulate such quasi-particles. The prepared TINWs were etched from the bulk-insulating 3D topological insulator material $(Bi_{1-x}Sb_x)_2Te_3$ (BST) and have been electrically probed in low temperature transport measurements [2, 3]. In such experiments, after proving the existence of the TSS, manipulation of the TSS enabled the discovery of a non-reciprocal transport effect that occurs due to a large magnetochiral anisotropy (MCA). Furthermore, after proximitizing the TSS with a superconductor, S-TI-S Josephson Junctions on TINWs of varying width have been studied.

Key ingredients for advanced detection and control techniques for MBS are a well-controlled and high material quality, confirmation of the existence and reliable control of the TSS as well as sufficiently robust induced superconductivity in a nanowire platform that is compatible with scalable device designs [4, 5]. While the potential for a larger size of the relevant energy scale in such TINWs compared to other materials makes 3D topological insulators (TI) an attractive material class for studying MBS [6], the preparation of bulk-insulating narrow TINWs with fabrication techniques that are compatible with advanced proposals, which require several deterministically branched and interconnected NWs, has not been reported before [4, 5]. Additionally, inducing robust superconductivity in a reproducible manner is not easily achieved in such bulk-insulating wires [7]. For these reasons, not all the requirements for experiments for an unambiguous

detection of MBS in 3D TINWs had been met before.

To tackle these challenges, here a versatile approach to prepare TINWs etched from bulk-insulating Molecular-beam epitaxy (MBE) grown thin films of the 3D TI BST has been developed which fulfills the aforementioned requirements. From low temperature transport measurements it is shown that narrow NWs prepared in this way maintain the high quality of the as-grown material, are gate-tuneable as well as bulk-insulating and show magnetic-field-dependent electrical resistance oscillations that are consistent with theoretical expectations, a manifestation and proof of the existence of the TSS [3]. Furthermore, a well-controllable rectification effect stemming from magnetochiral anisotropy in the TSS has been discovered that can be quantified by a coefficient $|\gamma| \sim 100000\,\mathrm{A^{-1}T^{-1}}$, an extraordinarily large value for a normal conductor [2]. Additionally, S-TI-S Josephson junctions have been studied to investigate and improve induced superconductivity in such TINWs. Here, in experiments with microwave irradiation a fractional Josephson effect has been observed that reveals transport signatures previously associated with an unconventional 4π-periodic supercurrent contribution that could be indicative of MBS [3, 8].

These results demonstrate that TINWs can be realized by top-down patterning from planar 3D TI BST thin films in a quality at least on par with previously existing preparation techniques, that they can be well used to study novel electronic transport phenomena that arise from discrete TSS and that they can further be successfully proximitized with a superconductor to study unconventional superconducting transport, all of which is interesting from both a fundamental point of view as well as for potential technical applications such as novel diode effects and topological quantum computation [6, 7, 9].

KURZZUSAMMENFASSUNG

Topologische Quantenmaterie dient seit etwa zwei Jahrzehnten als fruchtbarer Boden für die Untersuchung neuer Transportphänomene und grundlegender Aspekte der modernen Physik der kondensierten Materie. In jüngerer Zeit wurde erkannt, dass topologische Isolator-Nanodrähte (TINWs), die quantenbegrenzte topologische Oberflächenzustände (TSS) mit besonderer Spin-Physik aufweisen, exotische Quasiteilchen mit nicht-abelschen Austausch-Statistiken beherbergen können welche als gebundene Majorana Zustände (MBS) bezeichnet werden und von großem fundamentalem und technologischem Interesse sind [1].

In dieser Arbeit wurde eine TINW-Plattform entwickelt und experimentell untersucht, die die notwendigen Zutaten zur Realisierung von neusten Vorschlägen zur Untersuchung und Manipulation solcher Quasiteilchen liefert. Die präparierten TINWs wurden aus dem volumenisolierenden topologischen 3D Isolatormaterial $(Bi_{1-x}Sb_x)_2Te_3$ (BST) geätzt und in Tieftemperatur Transportmessungen elektrisch untersucht [2, 3]. In solchen Experimenten ermöglichte der Nachweis der Existenz und die Manipulation des TSS die Entdeckung eines nicht-reziproken Transporteffekts der aufgrund einer besonders großen magnetochiralen Anisotropie (MCA) auftritt. Darüber hinaus wurden nach der Kopplung des TSS mit einem Supraleiter S-TI-S-Josephson-Kontakte auf TINWs unterschiedlicher Breite untersucht.

Schlüsselkomponenten für Nachweis- und Kontrolltechniken für MBS sind eine gut kontrollierte und hohe Materialqualität, die Bestätigung der Existenz und die zuverlässige Kontrolle der TSS sowie eine ausreichend robuste induzierte Supraleitung in einer Nanodrahtplattform, die mit skalierbaren Probendesigns kompatibel ist [4, 5]. Während die größere relevante Energieskala von TINWs sie im Vergleich zu anderen Vorschlägen zur Untersuchung von MBS zu einer attraktiven Materialklasse macht [6], so ist die Herstellung von volumenisolierenden schmalen TINWs mit Fertigungstechniken die mit fortschrittlichen Experimenten kompatibel sind, die mehrere deterministisch verzweigte und miteinander verbundene NWs erfordern, bisher nicht gelungen [4, 5]. Weiterhin ist es

nicht einfach robuste Supraleitung in reproduzierbarer Weise in solchen volumenisolierenden Drähten zu induzieren [7]. Aus diesen Gründen waren bisher nicht alle Anforderungen für Experimente für einen eindeutigen Nachweis von MBS in TINWs erfüllt.

Um diese Probleme anzugehen wurde in dieser Arbeit ein vielseitiger Ansatz zur Herstellung von TINWs entwickelt, die hier aus Molekularstrahlepitaxie (MBE) gewachsenen Dünnschichten des volumenisolierenden 3D TI BST geätzt wurden und die die oben genannten Anforderungen erfüllen. Anhand von Tieftemperatur-Transportmessungen wird gezeigt, dass die auf diese Weise hergestellten schmalen NWs die hohe Qualität des gewachsenen Materials beibehalten, gate-tune-fähig sowie volumenisolierend sind und magnetfeldabhängige elektrische Widerstandsoszillationen zeigen, die mit den theoretischen Erwartungen übereinstimmen - eine Manifestation und ein Beweis für die Existenz der TSSs [3]. Darüber hinaus wurde ein gut kontrollierbarer Gleichrichtereffekt entdeckt der aufgrund einer magnetochiralen Anisotropie in den TSS entsteht und durch einen Koeffizienten $|\gamma| \sim 100000\ \mathrm{A}^{-1}\mathrm{T}^{-1}$ quantifiziert werden kann, ein außerordentlich großer Wert für einen normalen Leiter [2]. Abschließend wurden S-TI-S Josephson-Kontakte untersucht um die induzierte Supraleitung in solchen TINWs unterschiedlicher Breite zu studieren und zu verbessern. Hier wurde in Experimenten mit Mikrowellenbestrahlung ein fraktionierter Josephson-Effekt beobachtet der Transportsignaturen offenbart die zuvor mit einem unkonventionellen 4π-periodischen Superstrombeitrag in Verbindung gebracht wurden, ein möglicher Hinweis auf MBS [3, 8].

Diese Ergebnisse zeigen, dass TINWs durch Top-Down Strukturierung planarer 3D TI BST Dünnschichten in einer Qualität realisiert werden können die mindestens gleichwertig mit der der bisher existierenden Präparationstechniken ist. Des Weiteren wurden solche TINWs erfolgreich zur Untersuchung neuartiger elektronischer Transportphänomene verwendet die aufgrund der diskretisierten TSS entstehen, und können außerdem erfolgreich mit einem Supraleiter proximitiert werden um unkonventionellen supraleitenden elektrischen Transport zu untersuchen. All dies ist von großem Interesse sowohl für die Grundlagenforschung als auch für potenzielle technische Anwendungen wie neuartige Diodeneffekte oder topologische Quantencomputer-Technologie [6, 7, 9].

Chapter 1

INTRODUCTION

The dawn of topological effects in low-temperature electrical transport experiments caused a paradigm shift in the understanding of modern condensed matter physics. Topological insulators (TIs), a material class with a bulk-insulating interior and metallic surface states, are a prime example of quantum matter that enabled pioneering studies of the manifestations of topology in nature in the last two decades. More recently, considerable interest shifted towards the idea that topologically non-trivial electronic states can host quasi-particles with unconventional exchange statistics. Originally proposed by Ettore Majorana in 1937, Majorana fermions are described as particles that are their own antiparticles, meaning that they obey the quasiparticle operator relation $\hat{\gamma}_s = \hat{\gamma}_s^\dagger$ [10]. While such particles have not yet been observed in nature, emergent quasiparticle excitations that mimic their properties could potentially be realized by inducing superconducting pairing into the spin-momentum locked topological surface states (TSS) of TIs and TI nanowires (NW) [1, 6, 11, 12]. If such particles are spatially localized and their ground state lies at zero energy the system's excitations are called Majorana zero-modes (MZM) or Majorana Bound States (MBS). Apart from fundamental interest, well-separated pairs of such states can be used to form a quantum-bit which enables applications in topologically protected quantum computation that benefit from their unconventional non-Abelian exchange statistics and non-locality [4, 5, 13, 14].

The observation of signatures consistent with the understanding of localized Majorana states at that time has been reported for various systems, such as atomic chains of ferromagnetic iron on the surface of superconducting lead [15] and proximitized quantum anomalous Hall insulators [16], but most importantly for semiconductor nanowires with strong spin-orbit coupling, i.e. InAs and InSb [17, 18]. These results triggered excitement for technological application as in particular hybrid systems of III-V semiconductors and also 2D TIs based on HgTe [19] could be well-compatible with scalable fabrication techniques required for

large scale utilization in topological quantum computing [5, 14]. In recent years however, some results in these systems have been put to debate [20–22].

Nanowires made from 3D TIs have been proposed to host MBS that are comparably stable due to the large relevant energy scales involved [6]. Such TINWs, whose TSS exhibit a characteristic Dirac-nature as well as spin-momentum locking, have been realized in various ways in the past such as by Vapour-Liquid-Solid (VLS) growth [23–27], exfoliation of a bulk single crystal [28, 29], sandwiching between different materials [30], selective-area-growth (SAG) [31, 32], and top-down etching of a 2D film [33, 34]. Among them, the SAG and top-down etching techniques offer a large design flexibility and hence are particularly appealing for quantum devices and advanced theoretical proposals [4]. However, early binary TI compounds commonly exhibit a significant residual bulk-transport contribution that can complicate the unambiguous interpretation of measurement results and there has been no report of a successful tuning of the chemical potential to the charge neutrality point in NWs fabricated with these methods [7]. When coupled to a superconductor, a fractional Josephson effect can be observed in transport measurements on S-TI-S Josephson Junctions that are subject to microwave-irradiation. In the presence of Majorana states a 4π periodic supercurrent contribution is expected that can be reflected in a suppression of the so-called Shapiro steps in such measurements. This indeed has been observed successfully in planar HgTe and SAG 3D TI junctions [34–40]. Only recently however a first report addressed the question of how such transport signatures would change in narrow TINWs subject to a parallel magnetic field, which is required to manipulate the TSS to study MBS [34], and the role of large residual bulk-carrier contribution in many of the previous reports remains unclear. In any case, existing experiments cannot provide unambiguous evidence for MBS for which reason TINWs compatible with next-generation detection proposals are desired [41].

In this work the successful preparation of bulk-insulating TINWs etched from provided Molecular-beam epitaxy (MBE) grown $(Bi_{1-x}Sb_x)_2Te_3$ thin films as well as an experimental study of electronic transport phenomena both in normal-state and superconducting transport on such wires is presented. This was achieved by careful study and tuning of the relevant nanofabrication parameters of electron-beam lithography, Ar- and wet-etching to minimize adverse effects on the material during the preparation process. After testing various interface cleaning

recipes, buffer layers and superconductors to proximitize such TINWs, the detrimental role of surface oxidization was tackled by prompt ex-situ capping of the as-grown material with Al_2O_3. A procedure for timely and non-damaging removal of this capping was developed that allows to minimize the exposure of the TI surface to ambient conditions to only a few minutes while still benefiting from the versatility of widely available ex-situ fabrication techniques.

From low-temperature measurements on such TINWs it is shown that the developed easily accessible and flexible preparation procedure preserves the pristine quality of the as-grown BST thin film. In contrast to most previous reports, such NWs are bulk-insulating, the chemical potential can be tuned easily to the CNP by electrostatic gating and characteristic periodic oscillations in electrical resistance both as a function of externally applied magnetic-field and gate-voltage are observable. Although these oscillations show irregularities that likely stem from coulomb disorder, they are unambiguous evidence for the formation as well as control of the TSS of interest and allow for a comprehensive characterization of the NWs.
When studying induced superconductivity in such TINWs, a successfully induced supercurrent across S-TI-S Josephson junctions on wires of varying width revealed signatures of a 4π periodic supercurrent contribution in Shapiro measurements, something that in previous reports has been associated with the formation of MBS [8, 34, 40, 42].
Additionally, a previously unexpected manifestation of the TSS in TINWs was discovered, the occurrence of a giant magnetochiral anisotropy (MCA). Following a theoretical prediction, a non-reciprocal transport effect in TINWs that is characterized by an outstandingly large MCA rectification coefficient $|\gamma| \sim 100000$ $\mathrm{A}^{-1}\mathrm{T}^{-1}$ was confirmed experimentally in low-temperature measurements. This effect is highly controllable by gate voltage and magnetic field, both which are responsible for the underlying manipulation of the spin polarized subbands that give rise to this effect.

As non-reciprocal responses in quantum materials touch on fundamental aspects of modern condensed matter physics such as broken symmetries, topology, quantum confinement and correlations, MCA based on an intriguing combination of these aspects points to an unexplored playground to substantially enhance the size of non-reciprocal transport effects. Furthermore, for the first time a TINW

preparation protocol provides all the ingredients required to experimentally explore advanced detection and control proposals for MBS - preparation of bulk-insulating TINWs with well-controlled TSS from material grown in large scale and with reliable quality, that can be successfully proximitized and that can be patterned in planar branched structures [4, 5, 14]. Therefore in conclusion, these results give evidence that etched 3D TINWs are a versatile and scalable platform to investigate highly interesting novel transport phenomena such as Majorana states and (potentially superconducting) diode effects [6, 9]. Thereby the presented work serves as a steppingstone to enable further fundamental research on TINWs and their technical applications in for example rectifiers and topological quantum computation.

The contents of this work are structured as follows: First, in Chapter 2, a few theoretical concepts to introduce 3D TIs and more specifically TINWs are briefly reviewed to explain the underlying mechanisms of the observed transport effects. From a generalization of the considerations of topological classification derived from the Quantum Hall-effect, in systems with strong spin orbit coupling topological surface states can arise due to the bulk-boundary correspondence. When a 3D TI is formed into a nanowire, the resulting discrete surface state subbands with characteristic Dirac-nature and helical spin polarization due to spin momentum locking can give rise to interesting transport phenomena, especially when coupled to a superconductor, as studied in this work.

In Chapter 3 practical context is given on the used material and some of its defining properties as well as on key nanodevice-fabrication and low-temperature measurement techniques. $(Bi_{1-x}Sb_x)_2Te_3$ is a compensated 3D TI that can be grown as a thin film by MBE and with well-controlled quality, but that is also adversely effected by intrinsic disorder from charge compensation. When patterning such a surface-transport-dominated material treatment conditions need to be adjusted carefully to not harm the quality of the surface states. In this regard relevant technical developments during this work are described and the used low-temperature setups for transport measurements are introduced.

In Chapter 4 the successful preparation of etched bulk-insulating TINWs as well as the experimental study of electronic transport phenomena both in normal-state and superconducting transport across S-TI-S Josephson junctions on such wires is presented. It is shown that the developed easy to adapt preparation procedure preserves the pristine quality of the as-grown BST thin film and that in

contrast to most previous reports, such NWs are bulk-insulating. In the NWs prepared here, the chemical potential can be tuned easily to the CNP by electrostatic gating and characteristic periodic oscillations in electrical resistance both as a function of externally applied magnetic-field and gate-voltage are observable, both consistent with expectations and proof for the formation of TSS. Additionally, transport across S-TI-S Josephson junctions on such wires of varying width gives rise to signatures of a 4π periodic supercurrent contribution in Shapiro measurements. This has previously been considered evidence for the presence of Majorana Bound States, but trivial explanations need to be ruled out carefully [8, 34, 40–44].

In Chapter 5, a previously unexpected manifestation of the TSS in TINWs is reported, the occurrence of a MCA. After theoretical prediction and consecutive experimental confirmation, non-reciprocal transport in TINWs that is characterized by a outstandingly large MCA rectification coefficient $|\gamma| \sim 100000\ \mathrm{A}^{-1}\mathrm{T}^{-1}$ is investigated. Though this effect is only observed at low temperatures, in TINWs it is highly controllable via gate voltage and magnetic field, and serves as yet another example of the good theoretical understanding achieved for TINWs.

In the end, a brief summary and outlook is given in Chapter 6 which covers challenges and perspectives for the here presented TINW platform. Further supplementary information can be found in the Appendix in Chapter 7.

Chapter 2

THEORETICAL CONCEPTS

The contents of this work cover some topics that are commonly only briefly touched upon in typical condensed matter physics coursework. Therefore the purpose of this chapter is to provide a basic understanding of the relevant concepts. Since it is aimed at non-expert undergraduate and graduate researchers, the extent of review is limited and should serve as guidance for further study. More extensive discussion can be found in a number of specialized references [41, 45–51].

In the first section 2.1 the most important aspects of topological matter are briefly introduced, with a focus on the properties of 3D topological insulators (TIs). Section 2.2 reviews the consequences of size quantization in low temperature transport experiments when such a TI is formed into a nanowire (NW). This includes the existence of characteristic resistance oscillations in the presence of varying magnetic field and electrostatic-gating as well as a giant magnetochiral anisotropy, all evidence for topological surface subband states. A plethora of interesting effects has been predicted to arise from combining such TINWs with a superconductor, most strikingly the potential presence of Majorana bound states. Therefore basic concepts of superconductivity relevant in the context of this work and phenomena that are necessary to understand the experimental findings will be reviewed briefly in section 2.3.

2.1 Topological Insulators (TI)

In this section, after a brief contextualization, basic concepts of Topology and developments leading to the discover of 3D TIs are discussed. Their most fundamental features are introduced, including the guaranteed presence of a topological surface state characterized by spin-momentum locking and a linear Dirac dispersion, which serves as a baseline to understand effects that arise specifically in TINWs discussed later.

2.1.1 Band theory and quantum Hall effect

The understanding of the electronic transport properties in solids is governed by band theory, one of the most fundamental concepts in condensed matter physics. Pioneered by Bloch, it is based on the idea that in a periodic crystal-lattice the overlapping orbitals of individual atoms form bands in which electronic states can be unevenly distributed and charge carriers experience collective excitations. If electrons occupy all states up to the Fermi-energy E_f and if the next available states are separated by an energy gap electronic transport is not easily possible. This provides a profound explanation why materials such as metals conduct well while some others, e.g. insulators such as quartz, do not and is at the heart of extensive research on how to control electronic transport that caused tremendous technological progress in the past century. In 1980, however, the previously established understanding was challenged by the discovery of the integer quantum Hall (QH) effect. Von Klitzing et al. found that edge channels with an exactly quantized Hall conductivity of $\sigma_{xy} = n \times e^2/h$ with $n \in \mathcal{N}$ can arise in perpendicular high magnetic fields and at low temperatures in a two-dimensional electron system though its bulk remains insulating. This exact quantization based on fundamental constants is striking as it points at a fundamental macroscopic origin of this quantum phenomenon [52, 53], a finding that was awarded with a Nobel Prize only a few years later.

2.1.2 Topology

TKNN, Chern number and connection to the quantum Hall effect

In 1982, Thouless, Kohmoto, Nightingale, and den Nijs (TKNN) realized that the QH-effect was a result of topological properties of the electron's wavefunctions

[54]. In mathematics, topology deals with the properties of objects by characterizing whether they are invariant under smooth deformations. Objects can be classified for example by a topological invariant called genus g, which is commonly introduced by considering whether an object can be smoothly transformed into another while preserving a defining property, e.g. a hole. Similarly other systems like the electronic bands of a TI can be classified by an integer topological invariant $n \in \mathbb{Z}$ called Chern number which specifies whether they can be continuously deformed into one another. In general, the availability of such invariants is determined by the dimensions and the symmetry class of a system, which depends on the presence of e.g. time-reversal and crystal symmetries, and are of either integer value $\mathbb{Z}$, even integer $2\mathbb{Z}$ or binary value $\mathbb{Z}_2$ [55, 56]. The associated Chern number can be intuitively understood as a geometric phase acquired from moving a vector $\mathbf{k}$ associated with a Bloch-wavefunction $|u_m(\mathbf{k})\rangle$ around a closed loop in a parameter space, e.g. the Brillouin zone boundary [57, 58]. When $\mathbf{k_i}$ is moved from the north pole of a sphere via a closed path P while keeping its direction fixed southwards, upon arriving back at the north pole this results in an additional rotation of $\mathbf{k_i}$ by a geometric phase angle Φ. A quantum mechanical analogue proposed by Berry is called Berry phase and can be expressed by the line integral of the Berry connection $\mathcal{A}_m = i \langle u_m | \nabla_k | u_m \rangle$, from which also a surface integral called Berry flux $\mathcal{F}_m = \nabla \times \mathcal{A}_m$ can be calculated [57]. The Chern number then is the total Berry flux in the whole Brillouin zone calculated via

$$n_m = \frac{1}{2\pi} \int d^2\mathbf{k} \mathcal{F}_m \tag{2.1}$$

where n_m is an integer and the total Chern number being the sum over all occupied bands, $n = \sum_{m=1}^{N} n_m$. TKNN realized that the QH-effect can be described in a Hilbert space whose topological invariant also called TKNN invariant or filling factor $\nu \in \mathcal{Z}$ is intimately related to the Chern number. This factor ν allows to distinguish topologically trivial insulating regions (ν = 0) from topologically non-trivial regions ($\nu \neq 0$) and is linked to N of the quantized Hall conductance σ_{xy}, thereby revealing the effect's connection to concepts of topology.

Generalization to quantum spin Hall effect

Topological phenomena can also occur in the absence of an external magnetic field, for example being driven by the electron's motion and the associated spin-orbit coupling (SOC). Around 2005, first Kane and Mele [59, 60] and later Bernevig and Zhang [61] proposed generalizations that allowed to predict the existence of edge states in 2D materials, leading to concrete proposals for a quantum spin Hall

insulator. A key breakthrough was to recognize that a non-trivial $\mathbb{Z}_2$ topology can be present in ordinary insulators without breaking time-reversal symmetry (TRS) by a magnetic field. This eventually lead to the experimental observation of edge-state transport in CdTe/HgTe/CdTe quantum wells that resembled that of the one-dimensional channels with quantized conductance known from the QH-effect, but this time in zero magnetic field. This made the first observation of the QSH-effect a milestone in exploring topological effects in nature [62, 63].

Although historically effects stemming from topology were first discovered in quantum materials, understanding these effects has begun to influence many other fields of physics like photonics [64–67], microwave systems [68], classical electronics [69], cold atoms [70, 71], acoustics [72] or mechanics [73]. In the following the discussion will be focused on strong 3D TIs as well as key features of relevance for transport experiments in this work. Several in-depth reviews are recommended for further study to understand why topological order is of such fundamental and growing interest, especially in the context of dissipationless transport and emergent particles with fractional charge or peculiar exchange statistics [1, 46–48].

2.1.3 3D Topological Insulators

The underlying topological classification of the aforementioned 2D systems can be generalized to 3D TIs where a set of four $\mathbb{Z}_2$ topological invariants $(\nu_0; \nu_1, \nu_2, \nu_3)$ calculated from bulk properties is required [1]. In a time-reversal symmetric electronic system, energy eigenstates come in Kramers pairs, i.e. bands where the $+k$ and $-k$ states are at the same energy. At specific positions in the periodic Brillouin Zone (BZ) (called TR-invariant momenta (TRIM)) these eigenstates are degenerate. In the case of a non-trivial $\mathbb{Z}_2$ invariant the Kramers pairs have to "switch partners" at the BZ-boundary which leads to a guaranteed crossing of the surface or edge states with the Fermi energy inside the bulk gap, resulting in the appearance of topologically-protected metallic surface states with an odd number of crossings (Figure 2.1 a). As a consequence, at all interfaces to an ordinary (i.e. topologically trivial) insulator, e.g. the vacuum, n-dimensional TIs are necessarily associated with (n-1)-dimensional gapless metallic spin-non-degenerate surface/edge states (Figure 2.1 b).
The energy dispersion of these gap-crossing eigenstates resembles the linear dispersion of a single 2D Dirac cone with helical spin polarization, which means that the direction of the surface state's spin is locked perpendicular to the momentum k, thereby also termed spin-momentum locking (Figure 2.1 c). At low energy

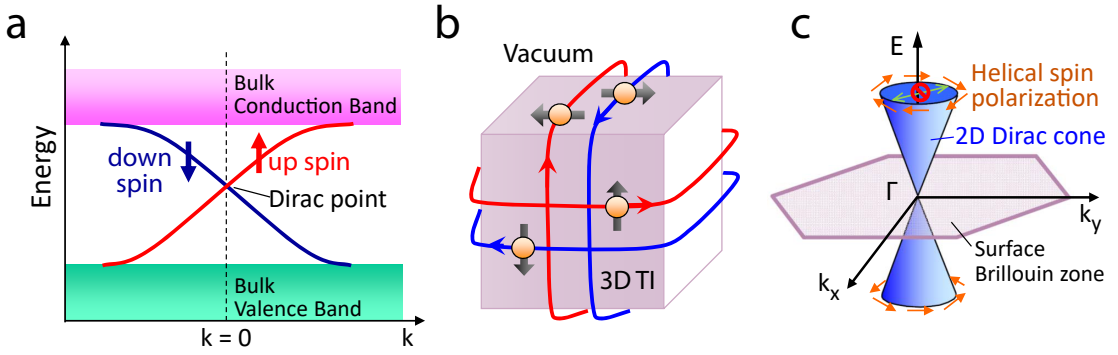

Figure 2.1: Topological surface states due to bulk-boundary correspondence. a, Illustration of the energy dispersion of the spin non-degenerate edge states of a 2D TI forming a 1D Dirac cone **b,** Schematic of the 2D helical surface state in real-space at the interface between a 3D TI and a trivial insulator, e.g. the vacuum. **c,** Energy dispersion of the spin non-degenerate surface state of a 3D TI forming a 2D Dirac cone at the Γ-point of the surface Brillouin-zone. Adapted with permission from Ref. [1] (c) (2013) The Physical Society of Japan.

this dispersion can be approximated by the Dirac equation for free particles and results in energy eigenvalues of $E = \pm c\sqrt{\mathbf{p}^2 + m^2c^2}$, thereby resembling the behaviour of relativistic Dirac particles. Notably, particles acquire a Berry phase of π upon full rotation on the Fermi surface so that interference of time-reversed scattering paths is altered, for example causing antilocalization or a band gap opening at the Dirac point in the case of quasi-1D nanowire systems, as will be discussed later.

It is noteworthy that in 3D TIs, when the chemical potential is far away from the Dirac-point, deviations from linear dispersion and second-order effects can take place that lead to for example hexagonal warping of the Fermi surface, as visualized by angle-resolved photoemission spectroscopy [74]. Furthermore, TSS are commonly associated with a vague notion of topological protection. First, as governed by the $\mathbb{Z}_2$ topology, the gapless surface states are not allowed to vanish as long as TRS is preserved, making them robust against impurities and distortions, e.g. from physical surface treatments. Also scattering from carriers with momentum k into the $-k$ state is suppressed due to the helical spin polarization and thereby spin mismatch, see Figure 2.1 c (though the probability for backscattering to other states remains finite). Additionally the π-Berry phase associated with the Dirac-like nature of the carriers affects destructive self-interference, thereby reducing weak localization of time-reversed paths.

Fundamental interest in the aforementioned properties as well as the hope for applications from spintronics to topological quantum computation caused a surge in research on 3D TIs in the past two decades [7]. In particular, TINWs prepared from such TIs are of special interest as will be discussed in the following.

2.2 Topological Insulator Nanowires (TINW)

In condensed matter physics, interesting phenomena can arise when the dimensionality of a system is reduced or size-quantization effects start to play a role, as for example in the case of 2D electron gases, Graphene or quantum dots, all which enabled the observation of groundbreaking new physical phenomena [75–77]. As done with III-V semiconductor NWs and carbon nanotubes, quasi-1D TINWs are a natural next step to explore the properties of topological surface-states (TSS). In such TINWs, discrete TSS arise from size-quantization which allow for novel transport effects. In particular, for electrons on the TI surface an axial magnetic flux can cause a topological phase transition and the interplay of strong spin-orbit coupling together with inversion symmetry breaking can facilitate a gate-tuneable giant magnetochiral anisotropy effect. Both will be outlined in the following.

2.2.1 Size quantization of topological surface states

Given the exotic properties of TIs, it is appealing to consider the consequences that arise when the 2D surface states of a 3D TI are reduced to quasi-1D. This can be achieved by various techniques including vapour-liquid-solid (VLS) growth [23–27], exfoliation from a bulk single crystal [28, 29], sandwiching between different materials [30], selective-area-growth (SAG) [31, 32] and top-down etching of a 2D film [33, 34]. Owing to a combination of a reduced bulk-to-surface ratio and the use of compensated TIs like $(Bi_{1-x}Sb_x)_2Te_3$ (BST) such TINWs show surface-dominated transport and behave analogous to a quasi-ballistic metal-ring [78] or a hollow metallic cylinder [79]. In such TINWs where phase coherent transport is maintained around the perimeter of the NW the surface states are confined, resulting in a quantized circumferential momentum $k_\perp$ which leads to discrete surface state subbands with an energy-level spacing that depends on the perimeter [6, 80, 81]. Here, the presence of an axial magnetic field $B_\parallel$ causes charged particles on the surface to pick up a phase when encircling a magnetic

flux, leading to Aharonov-Bohm (AB) or Altshuler-Aronov-Spivak (AAS) interference effects [82]. A unique feature of TINWs is that the helical spin-texture of the spin-momentum locked surface states dictates that a particle travelling along the axial direction $k_{\parallel}$ picks up a Berry phase of π in case it encircles the circumference, which is due to a 2π rotation of the spin. In the absence of symmetry breaking and for an idealized cylindrical TINW, although generalizable to an arbitrary cross-section [83, 84], this results in a TSS subband energy dispersion given by

$$E_{\ell}(k) = \pm\hbar v_{\mathrm{F}}\sqrt{k^2 + \left(\frac{\ell - (\Phi/\Phi_0)}{R}\right)^2}, \tag{2.2}$$

where v_{F} is the Fermi velocity, R is the wire radius, and $\Phi_0 = h/e$ is the flux quantum in the presence of an axial magnetic flux Φ threading along the nanowire [6, 7]. Figure 2.2 a shows a schematic of the resulting subband structure, which is particularly interesting when the flux is modulated. In the absence of $B_{\parallel}$ or for a flux $\Phi = n\Phi_0$, with $n \in \mathbb{N}$, the above expression eq. (2.2) results in the formation of spin-degenerate surface state subbands indexed by $\ell = \pm\frac{1}{2}, \pm\frac{3}{2}, \ldots$ with ℓ the angular momentum quantum number. These surface subbands are then gapped by an energy that depends on the perimeter of the NW, as visualized in Figure 2.2 a. In contrast, a half-integer flux $\Phi = (n+1)\Phi_0/2$ gives rise to a topologically protected non-degenerate gapless 1D mode with $k_{\perp} = 0$ crossing the Dirac-point due to the AB-phase cancelling the Berry phase. Therefore, depending on integer multiples of $\Phi_0/2$, a spin-non-degenerate 1D mode is present or absent that can close the bulk band gap. This 1D mode is of special interest as it is predicted to host fermionic Majorana states when proximitized by a superconductor [6, 85].

2.2.2 Characteristic resistance oscillations

Since a change in axial magnetic flux can drive periodic topological transitions by closing as well as reopening the energy gap via a gapless mode, this can modulate the available density of states (DOS). Thereby the resistance maxima of the AB oscillations (ABO) occur at either integer $\Phi = n\Phi_0$ (0-ABO) or half-integer $\Phi = (n+1)\Phi_0/2$ (π-ABO) multiples of Φ_0, depending on the location of the Fermi level [82]. This characteristic π-phase shift of the ABO in TINW as a function of μ, which is varied by the gate-voltage, is demonstrated in Figure 2.2 b. It shows a colormap of the normalized change in the resistivity, $\Delta\rho/\Delta\rho_{\max}$ as a function of both axial magnetic flux Φ (normalized by Φ_0) and the carrier density n_{den} near the CNP (normalized by the value n_0 at the edge of the first subband) as expected

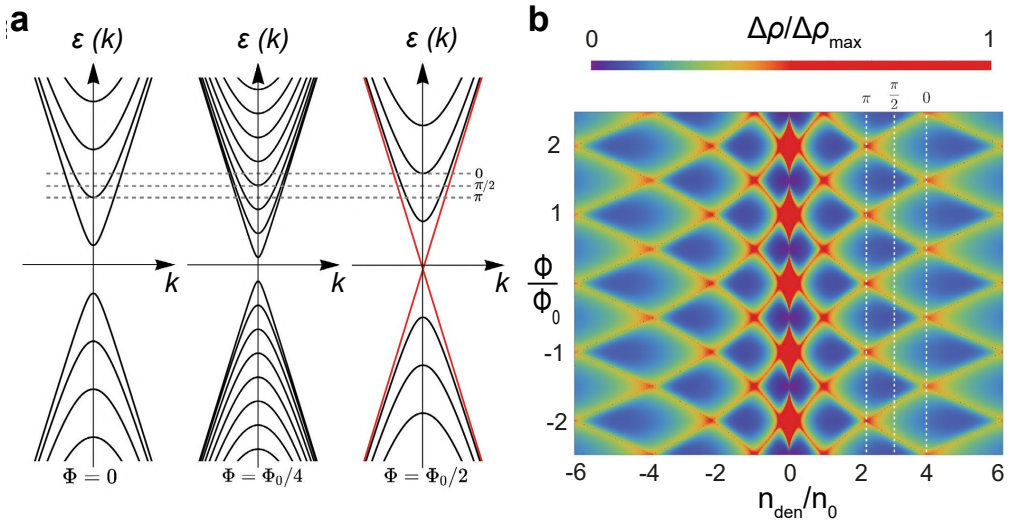

Figure 2.2: Discrete topological surface state subbands in a TINW. **a,** Schematic of the quantized topological surface state energy subbands formed in a TINW as a function of momentum k for an axial magnetic flux Φ of 0, $\Phi_0/4$, and $\Phi_0/2$. Red lines indicate a gapless spin-non-degenerate 1D mode. Dashed horizontal lines mark characteristic positions of Fermi energy E_F relevant for a peak in the resistance oscillations. **b,** Color mapping of the normalized change in the resistivity, $\Delta\rho/\Delta\rho_{\mathrm{max}}$, expected from theoretical calculations as a function of both axial magnetic flux Φ (normalized by Φ_0) and the carrier density n near the CNP (normalized by the value n_0 at the edge of the first subband). n is controlled by variation of the chemical potential μ via electrostatic gating. White vertical dotted lines denote the three positions of E_F marked in panel **a**. At a fixed E_F, $\Delta\rho$ oscillates with Φ. The oscillation phase shifts depending on n, in total causing a checker-board-like pattern.

from theoretical calculations. For these calculations the surface states of the wire are described by the 2D Dirac equation and disorder is taken into account by adding a small density of randomly located local scattering potentials so that by using a T-matrix approximation resistivities could be obtained in a fully analytical way [26]. The oscillations observed in Figure 2.2 b are then mainly the result of the increased scattering rate that arises at the minimum of a subband due to the van-Hove singularity, a divergence in the density of states at k-points where an extremum of the dispersion relation $E(\boldsymbol{k})$ takes place.

A consequence of this band structure is that characteristic oscillations in resistance R also occur as a function of the chemical potential μ, i.e. as a function of gate-voltage V_G. The positions of the maxima and minima in $R(V_G)$ relative to the charge-neutrality point depend on the charge density $n \propto \mu^2$ and follow

a characteristic quadratic trend in the gate voltage $\Delta V_G = (V - V_{CNP})$. These positions can be determined from the expected subband spacing, which is set by the perimeter, and the gate-induced change in chemical μ that depends on the gate-capacitance C. Although the spacing of gate-voltage resistance oscillations is sensitive to a good estimate of C, it can be argued that C can be modelled well by an electrostatic model that includes the dielectric environment, thanks to the simple slab-like geometry of the thin-film based devices. C can then be obtained by solving the Laplace equation using a finite element method and only two simple assumptions need to be made, that the nanowire can be modelled as a perfect metal and that effects of quantum capacitance can be neglected in such a wire geometry [26].

By combining the analysis of magnetic-field dependent AB-oscillations and gate-modulated subband resistance oscillations, consistency can be checked conveniently by i) comparing the cross-sectional area of the device obtained from imaging to the area expected from the experimentally obtained ABOs, and ii) by comparing the perimeter of the NW from imaging to the expected perimeter resulting from oscillations in $R(V_G)$, together allowing to obtain a comprehensive insight into the TINW's properties.

2.2.3 Magnetochiral Anisotropy

Chirality denotes that an object or system is not mirror-symmetric and cannot be superimposed on their mirror image by any translation or rotation, as in the case of hands or certain molecules. This property is of great relevance in various scientifc contexts, e.g. in the questions on why there is a homochirality of life on earth. Magnetochiral anisotropy (MCA) describes the interplay between chirality and magnetic fields and was first observed as a difference in the behaviour of unpolarized light in chiral media in a magnetic field. Later it was also found in a variety of other experiments e.g. with sound propagation, photo- as well as electro-chemistry [86]. Anisotropic electronic transport is of great technical relevance and more specifically in TINWs, MCA arises as a consequence of the confined topological surface states, thereby serving as a tool to study them.

In electrical transport, which is commonly well described by Ohm's law, $V = IR_0$, for small currents I the voltage drop across a material is proportional to a constant resistance R_0. An unconventional additional contribution from MCA can be described by an expansion term second order in current to the electrical

resistance

$$R = R_0(1 + \gamma BI), \tag{2.3}$$

with B being the magnitude of an external magnetic field and γ being the size of the rectification stemming from non-reciprocal transport. Such an effect is usually observed in systems that explicitly break inversion symmetry, so that a difference $R(+I) \neq R(-I)$ arises when a current flow in opposite directions is compared. The most well-known example of this is a semiconductor pn-junctions, a type of rectifier with great technological importance. However, a much greater degree of control over the rectification effect can be achieved when a similar non-reciprocity of resistance exists as a property of the material itself. To achieve such a non-reciprocity necessitates that the inversion symmetry of the material is broken and in materials where such symmetry breaking resulted in strong spin-orbit coupling (SOC) [87–94], large non-reciprocal effects were observed. However, the fact that SOC is always a very small energy scale limits the possible size of any rectification effect.

In heterostructures of topological materials it is possible to artificially break inversion symmetry and to significantly enhance the size of non-reciprocal transport effects [84]. In particular in quasi one-dimensional bulk-insulating three-dimensional TINWs it is possible to artificially break the inversion symmetry along the wire, for instance, by application of a gate-voltage from the top of the TINW [26, 33, 84]. Such a gate voltage induces a non-uniformity of charge density across the nanowire cross-section which breaks the subband degeneracy and results in a splitting of the subband at finite momenta. An additional consequence is that the subband states develop finite spin polarization in the plane perpendicular to the nanowire axis (i.e. yz-plane) with the states with opposite momenta being polarized in opposite directions such that time-reversal symmetry is respected. When a magnetic field is applied, the subbands can be shifted in energy via the Zeeman effect (Figure 2.3 a) and MCA can be measured [2].

This can be explicitly shown by using the Boltzmann equation [91, 92, 94]. For MCA of the vector product type $\gamma \propto \boldsymbol{P} \cdot (\hat{\boldsymbol{B}} \times \hat{\boldsymbol{I}})$ with the characteristic vector $\boldsymbol{P}$ in the yz plane, the rectification effect $\gamma_\ell(\mu)$ of a given subband pair $\eta = \pm$ labelled by $\ell > 0$ can be calculated as

$$\gamma_\ell = \gamma_\ell^+ + \gamma_\ell^- \approx \frac{e^3}{(\sigma^{(1)})^2 hB} \sum_{\eta=\pm} \tau^2 \left[\mathcal{V}_\ell^\eta(k_{\ell,R}^\eta) - \mathcal{V}_\ell^\eta(k_{\ell,L}^\eta)\right]. \tag{2.4}$$

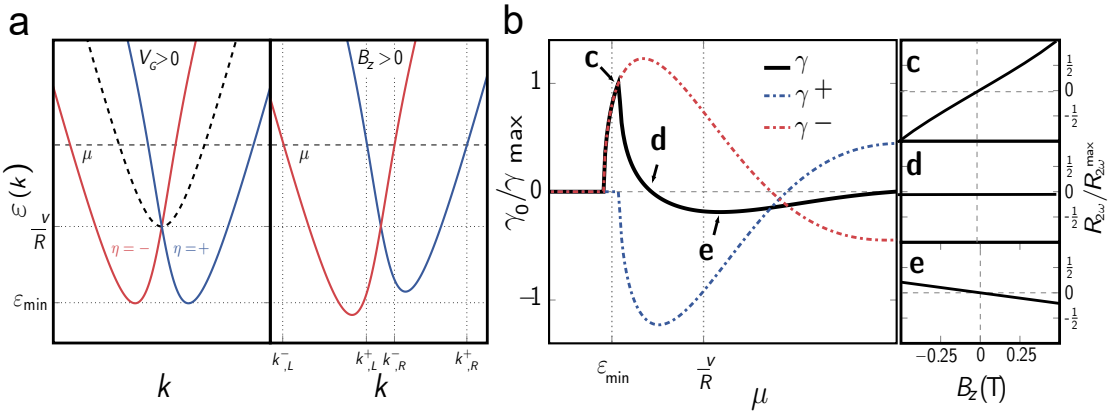

Figure 2.3: Topological surface state subband splitting in a TINW. **a,** Surface state subbands with finite spin polarization in yz-plane. Subband degeneracy (dashed line) is broken because an applied gate-voltage V_g causes a non-uniformity of the charge density across the nanowire cross-section and thereby breaks inversion symmetry. An additional applied magnetic field B out of plane causes a Zeeman-shift of the spin-polarized subbands. **b,** Size of the MCA rectification γ_ℓ as a function of chemical potential μ within a subband pair. Anisotropic spin-polarization results in a giant MCA with a characteristic sign-change as a function of μ. Panels c-e show the theoretically expected magnetic-field dependence of the 2nd harmonic resistance $R_{2\Omega}$ at the chemical potentials indicated in the main panel. Reproduced with permission from Springer Nature from [2].

Here e is the elementary charge, h is the Planck constant, $\sigma^{(1)}$ is the conductivity in linear response, τ is the scattering time, $\mathcal{V}^\eta_\ell(k) = \frac{1}{\hbar^2}\partial^2_k \epsilon^\eta_\ell(k)$ with $\epsilon^\eta_\ell(k)$ is the energy spectrum in the presence of symmetry breaking terms and finite magnetic field B, and $k^\eta_{\ell,R(L)}$ is the right (left) Fermi momentum of a given subband [2]. Due to the non-parabolic spectrum of subbands, $\mathcal{V}^\pm_\eta(k)$ is large for a TINW, so that a giant MCA can be expected where the quantities γ^+_ℓ and γ^-_ℓ are the contributions of the individual subbands. Interestingly, the behaviour of γ_ℓ as a function of chemical potential μ, shown in Figure 2.3 b, is as such, that when μ is tuned through a subband pair, γ_ℓ will change sign depending on the chemical potential. This makes the rectification effect due to the MCA highly controllable by both magnetic field direction and by the chemical potential μ within a given subband pair, which can be experimentally adjusted by a small change in gate voltage. Strikingly, for reasonable experimental parameters a theoretically expected size of the rectification is found to easily reach giant values $\gamma \sim 5 \times 10^5\ \mathrm{T^{-1}A^{-1}}$, much larger than in typical materials with a rectification coefficient $|\gamma| \lesssim 1\ \mathrm{A^{-1}T^{-1}}$ [89–93]. This motivates to investigate MCA in TINWs as done in chapter 5.

2.3 Proximity-induced Superconductivity in TINWs

Superconductivity is one of the most exciting phenomena in physics and understanding its quantum-nature laid the foundation for tremendous technological progress. A particularly interesting idea in the context of this work is to combine superconductivity with topological properties of for example a 3D TINW by coupling it to a s-wave superconductor. This raised much excitement due the possible formation of Majorana bound states (MBS) in such a hybrid system. MBS are of great interest due to both their anyonic properties as well as due to their potential use in topologically protected quantum computation technology. "We shall not describe here the vast amount of theoretical results, which has been derived from these equations" as renowned expert in superconductivity and Cologne emeritus Gert Eilenberger put it already in 1968 [95], but rather give a concise recapitulation of a few basic key concepts of superconductivity to understand the experimental results of this work. This includes a brief recap of BCS theory, the superconducting proximity effect in the context of BTK theory, consequences for SNS Josephson junctions as well as the Josephson relations, which eventually allows to discuss the RCSJ-model to explain the observation of a fractional Josephson effect in the presence of a 4π-periodic supercurrent contribution. More comprehensive specialized reviews are recommended for further reading [46–51].

2.3.1 BCS Theory

After first astonishing experiments on superconductivity [50, 51, 96–98], a phenomenological description that reproduced essential features was provided 1935 by the London equations [99]. Nevertheless it took about half a century since the first observation of superconductivity until the BCS theory proposed by Bardeen, Cooper and Schrieffer established a microscopic picture in 1957 [100, 101]. Here, the notion of quantum coherence and an associated length scale parameter lead to a theory of energetically favourable pair condensation that results from attractive phonon-mediated interactions. In consequence so-called Cooper pairs, which are bosonic particles comprised of two carriers with opposite spin, form due to electrostatic attraction when they interact with the ions of the crystal lattice. If energetically favourable, at typically low temperatures the Cooper pairs' bosonic nature allows them to condense into a lowest energy ground state due to

the absence of the Pauli exclusion principle, which results in a macroscopic superconducting state described by a single wave function. This pair formation opens an energy gap $\Delta \sim 1.75\, k_b T_c$ (with T_c the critical temperature) in the fermionic excitation spectrum which is equivalent to the energy needed to excite a quasiparticle out of the ground state of the condensate. Within this gap, all electrons are bound in cooper pairs so that the thereby freed-up single particle states manifest in tails in the DOS just outside the gap. These superconducting correlations take place on a length scale that depends on the largest available phonon frequency (Debye cutoff frequency $\omega_{\mathrm{D}} \sim 10^{-13}$s) and the electrons' Fermi velocity $v_F \sim 10^6$ ms^{-1}, which results in a coherence length $\xi_0 = \frac{\hbar v_F}{\pi \Delta}$ on the order of ∼100 nm for typical metallic superconductors. An early success of BCS theory was to estimate the scaling of T_c in various materials via $T_c = 1.14\Theta_D \exp\left[-1/\left[UD(E_F)\right]\right]$ where $D(E_F)$ is the electronic density of states at the Fermi level, U is an electron-phonon coupling strength (depending on lattice site mass), and Θ_D the Debye temperature. Experimental confirmation of this scaling for elemental superconductors and isotopes in first approximation implies that properties of the superconducting phase like the transition temperature depend on the carrier concentration n which explains why semiconductors with orders of magnitude lower n compared to metals are rarely superconducting, a fact relevant in the context of proximity-induced and gate-tuneable superconductivity. Cooper pairing leads to an energy dispersion similar to that of free particles but with an extra pairing potential Δ. In the case of excitations smaller than Δ, all cooper pairs remain in the same macroscopic quantum state with a joint total momentum k, resulting in a zero-resistance supercurrent. Another important consequence is that the description by a single wave function can lead to quantization effects, e.g. in a superconducting ring. Here the wavelength $\sigma = h/p$ must obey $n\sigma = 2\pi r$, i.e. fit exactly n = 0,1,2... times into the confining ring to form a standing wave. From this follows that a magnetic flux $\phi = h/2e$ must be quantized when threading a superconducting ring [50].

Further theoretical descriptions exist, like the phenomenological Ginzburg-Landau (GL) theory that deals with superconductivity especially close to phase transitions in terms of free energy and a complex order parameter, or the generalized mean-field theory Bogoliubov–de Gennes equations for inhomogeneous superconductors that are particularly useful to describe the interplay of topology and superconductivity. However, discussion here is limited to theory directly relevant for the later reported experiments and in-depth reviews are presented in more appropriate detail elsewhere [50, 51, 102].

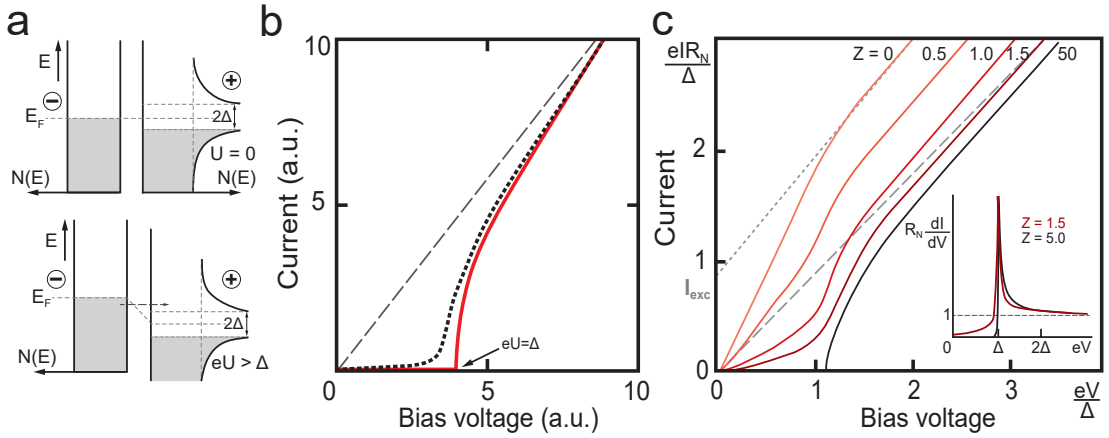

Figure 2.4: Transport in a NIS tunnel-junction. a, Semiconductor model description of a NIS tunnel-junction. Density of states versus energy for two scenarios of external bias U=0 and $U > \Delta/e$. Shading indicates occupied states. **b,** I-V characteristic where a bias $U = \Delta/e$ causes an abrupt tunnel current onset (red line) that can be smeared by finite temperature thermal excitation (dotted line) and for $eU \gg \Delta$ approaches regular ohmic behaviour (dashed line). **c,** Exemplary I-V response for different interface scattering parameter Z. Inset shows corresponding dI/dV response. Figures adapted from [103, 104].

2.3.2 Andreev reflection and BTK theory: The superconducting proximity effect

Given the notion of a gap Δ in the density of states (DOS) around E_F, similarities to the semiconductor band model become apparent. Consider two bands, a conduction and a valence band, that are separated by a gap which in superconductors is just small (typically $\Delta \sim 1$ meV) compared to that in semiconductors (typically $\Delta \sim 1$ eV). When the superconductor (S) is connected to a normal metallic lead (N) via a small insulating barrier (I) to form a NIS tunnel-junction, only when a threshold bias $eU > \Delta$ is applied E_f is shifted in a way that allows carriers to fill the accessible states above the gap in the superconductor such that a current proportional to the tunnel rate and available DOS can flow (see Figure 2.4 a). This steep onset can be smeared by finite temperature thermal excitation and for $eU \gg \Delta$, the I-V characteristic asymptotically approaches regular ohmic behaviour (Figure 2.4 b).

When reducing the picture to an unbiased NS-interface, due to the superconducting gap single particle transmission is not allowed and consequentially incident carriers are either elastically reflected or, more interestingly, a process named Andreev-reflection (AR) can take place that enables charge transfer across the

junction, the supercurrent. Blonder, Tinkham and Klapwijk realized in the early 1980s in their BTK theory that by AR an incident electron (hole) is reflected back into the normal region as a hole (electron) with opposite spin and momentum while in the superconductor a charge-2e spin-singlet called cooper pair is formed [50, 103]. This process is spin-dependent and can be inhibited by spin-polarization, e.g. in ferromagnetic materials, an effect that is used for example in point contact spectroscopy techniques like spin-polarized STM [105]. Ideal AR doubles the conductance across the N-S interface, but in realistic systems near-unity transparency of the interface is difficult to achieve. In non-ideal interfaces a considerable amount of ordinary reflection takes place which can be modelled by introducing a Dirac delta function tunnel barrier $H\delta(x)$ with H the strength of the barrier [106]. An associated scattering parameter $Z = H/\hbar v_f$ related to the probability of such normal reflection at the interface is connected to the transmission coefficient called transparency T with

$$T = \frac{1}{1+Z^2} \tag{2.5}$$

which governs the $I-V$ response and the diverging differential conductance dI/dV of the junction outside of the superconducting gap caused by the large DOS-tail (Figure 2.4 c). Even in low transparency junctions, an excess current I_{exc} commonly defined as the zero-bias voltage intersection of a linear fit to the $I-V$ curve above a bias of 2Δ is an indication of a finite contribution from AR [103].

2.3.3 Andreev bound states in SNS-junctions

The limit of a low barrier strength is naturally obtained for a thin conducting but not superconducting weak-link. When extending the system to consist of a normal (N) metal, semiconductor or TI sandwiched between two superconductors, i.e. an SNS junction, particles can be trapped in the resulting quantum well formed by total Andreev reflection against the superconducting regions [103]. As AR happens in series, similar to a particle in a box situation discrete-energy states called Andreev-Bound States (ABS) emerge, in the simplest case an ABS doublet of ground and excited state, that carry the supercurrent (Figure 2.5 a). These states are in the most conventional form described by

$$E(\phi) = \pm\Delta\sqrt{1 - T\sin^2\frac{\phi}{2}} \tag{2.6}$$

with a transmission coefficient T. Thereby they usually exhibit (for $T \neq 1$) a 2π periodic current-phase relation (CPR) dependent on the phase difference $\Phi =$

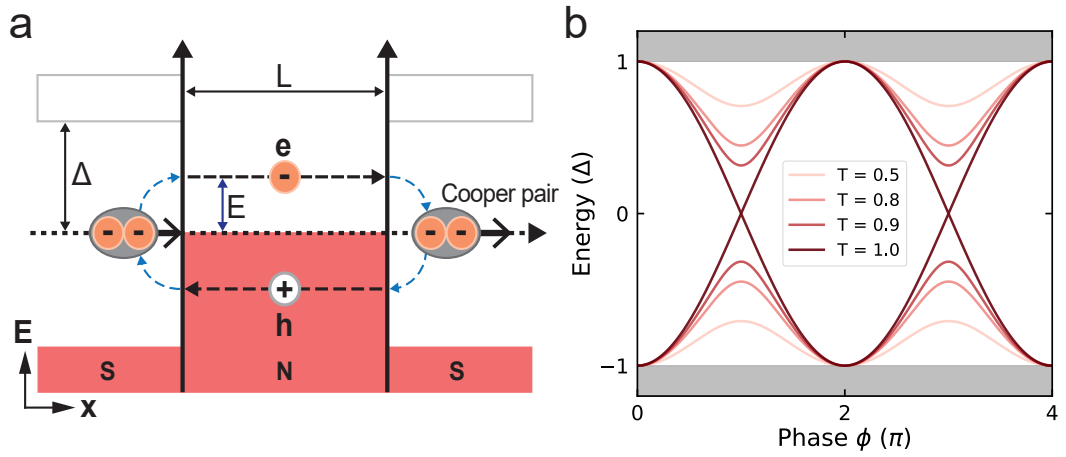

Figure 2.5: Andreev bound states in SNS-junctions. a, Illustration of superconducting transport via the formation of Andreev levels. A cooper pair incident from a superconducting lead with an energy gap 2Δ transfers to the opposite electrode by successive Andreev reflections of carriers in the normal region of length L. **b,** Conventional Andreev bound states with different transmission coefficients T. Quasiparticle poisoning at points close to continuum states (grey) or nonadiabatic interband transitions can alter periodicity.

$\Phi_1 - \Phi_2$ between the two superconductors and an excitation spectrum within the superconducting energy gap Δ with a minimum gap $\Delta_{ABS} = 2\Delta\sqrt{1-D}$ at ϕ_n = (2n+1)π emerges (Figure 2.5 b). Together, the intimate connection between AR and phase-coherent propagation in the normal region can thereby be seen as the microscopic origin of a proximity effect – an induced finite pairing potential giving rise to superconductivity in the normal region. This pairing occurs over a distance that depends on parameters such as transparency and the superconducting coherence lengths η_S and η_N in the superconducting leads as well as the normal region where the latter can be estimated as $\xi_{\mathrm{N}} = \sqrt{\hbar D/\Delta_{\mathrm{ind.}}} = \sqrt{E_{\mathrm{Th}} L^2/\Delta_{\mathrm{ind.}}}$, with $D = v_f l_e/2$ the average diffusion constant of supercurrent-carrying electrons, the induced gap $\Delta_{\mathrm{ind.}}$, l_e the mean free path, v_f the Fermi velocity, L the length of the junction and the Thouless energy $E_{\mathrm{Th}} = \hbar D/L^2$ [106].
Additionally, if a DC bias $V < 2\Delta$ is applied and the inelastic scattering length in the normal region $l_\Phi > L$, particles can undergo multiple Andreev reflections (MAR) and hereby acquire energy when traversing the junction. This allows them to overcome the superconducting gap and form additional dissipative conduction channels. Thereby, MAR explain the experimentally observed sub-gap structures in the differential conductance dI/dV that appear at the bias voltage $V_n = \frac{2\Delta}{ne}$ with $n \in \mathbb{N}$ [107, 108].

SNS junctions are commonly classified by comparing the length L of the normal weak link to its mean free path l_e and coherence length ξ_n. A junction is defined to be in the short (long) junction regime for $L \ll \xi_n$ ($L \gg \xi_n$) and ballistic (diffusive) for $L \ll l_e$ ($L \gg l_e$). A ballistic junction results in a discrete ABS spectrum with $\xi_n = \frac{\hbar v_f}{\Delta}$, whereas a diffusive junction has a less well-separated potentially even quasi-continuous spectrum of ABS. [109–111].

2.3.4 Majorana Bound states in proximitized TIs

It is intuitively clear that the induced superconducting state must be influenced by the properties of the weak link of the planar Josephson Junction, e.g. the topological properties of a TI. In fact, spin-momentum locking in the TI dictates that although the commonly used s-wave superconductors provide cooper pairs of two opposite-spin-$\frac{1}{2}$ particles the induced superconductivity must be p-wave-like or "spinless" because only one spin-configuration is allowed for a specific momentum k [11, 48, 49]. In a Josephson junction with a finite 2D extension on a 3D TI, a number $N = W/\lambda_f$ of Andreev doublets carry the supercurrent, with W the width of the channel. Due to the Dirac nature and the finite spatial extension of the weak link the transmission coefficient T_θ written as

$$T_\theta = \frac{\cos^2\theta}{1 - \frac{\sin^2\theta}{1+Z^2}} \tag{2.7}$$

is angle-θ-dependent, with Z being the scattering parameter. In consequence the ABS spectrum is given by equation (2.6) with a T_θ indexed by θ, with cos(θ)= $\sqrt{1 - \frac{k_y^2}{k_F^2}}$ [41, 112]. In such a system an intrinsic single 4π-periodic Andreev doublet with perfect transmission occurs at transverse momentum $k_\mathrm{y} = 0$ ($\theta = 0$) since here $T_{\theta=0} = 1$ for any Z. This 4π mode, together with additional trivial lower transmission oblique modes with $k_y \neq 0$ that are not protected from backscattering but still subject to spin-momentum locking (thereby called helical), carries the supercurrent across the junction. In the 1D-limit ($\theta = 0$, $T_{\theta=0} = 1$) and presence of p-wave pairing for bound states generically described by

$$E(\phi) = \pm\Delta\sqrt{T_\theta}\sin\frac{\phi}{2}, \tag{2.8}$$

consequently back-scattering is forbidden and the resulting 4π-periodic state can be identified to be a Majorana bound state, a hybridization of Majorana states at each S-TI interface [11, 12, 113, 114]. Complications to this simplified picture,

which depend on microscopic details, exist, for example from an increased number of transport channels and scattering in long diffusive junctions or quasiparticle poisoning. However, key features, especially the 4π-periodicity, are theoretically quite robust.

Considering not a planar junction but a NW formed from a TI and coupled to a superconductor, the interplay of discrete degenerate surface state subbands and an axial magnetic flux discussed in section 2.2 as well as the induced superconductivity can result in the appearance of a proximitized spin-non-degenerate gapless 1D mode. Here, in particular at integer multiples of the flux $\phi_0/2$ only a single pair of nondegenerate Fermi-points exists for any chemical potential μ inside the bulk-band gap, which is typically $\sim$300 meV. Superconducting pairing in this flux-tuneable mode is expected to give rise to Majorana states at the system's boundaries under a wide range of conditions. This marks a distinct advantage in terms of stability and control of MBS in comparison to alternative platforms like for example InAs with a relevant energy scale of $\sim$1 meV and is a central motivation to study proximitized 3D TINWs [6, 85].

Observing the discussed gapless states in a TI-superconductor hybrid system is of high interest as they are characteristic evidence for unconventional superconducting pairing that potentially enables the realization of Majorana fermions, which are interesting due to their peculiar non-abelian exchange statistics and promise for applications in topologically protected quantum computation [4]. For a comprehensive discussion the reader is referred to some of the many more detailed reviews [6, 11, 41, 49, 114, 115].

2.3.5 Josephson equations

In transport across a weak link SNS junction the supercurrent is subject to the Josephson effect which is a manifestation of the macroscopic quantum nature of superconductivity. Consider the superconducting leads A and B to each have a Ginzburg-Landau order parameter $\psi_{A/B} = \sqrt{n_{A/B}}e^{i\phi_{A/B}}$ (with carrier densities $n_{A/B}$) that reflects the condensates' wave functions, then the supercurrent I_s across the junction can be shown to be described by the two Josephson relations [51, 116, 117]

$$I_s(t) = I_c \sin(\varphi(t)) + \sum_{m=2}^{\infty} I_m \sin(m\varphi(t)) \tag{2.9}$$

$$\frac{d\varphi}{dt} = \frac{2eV(t)}{\hbar} \tag{2.10}$$

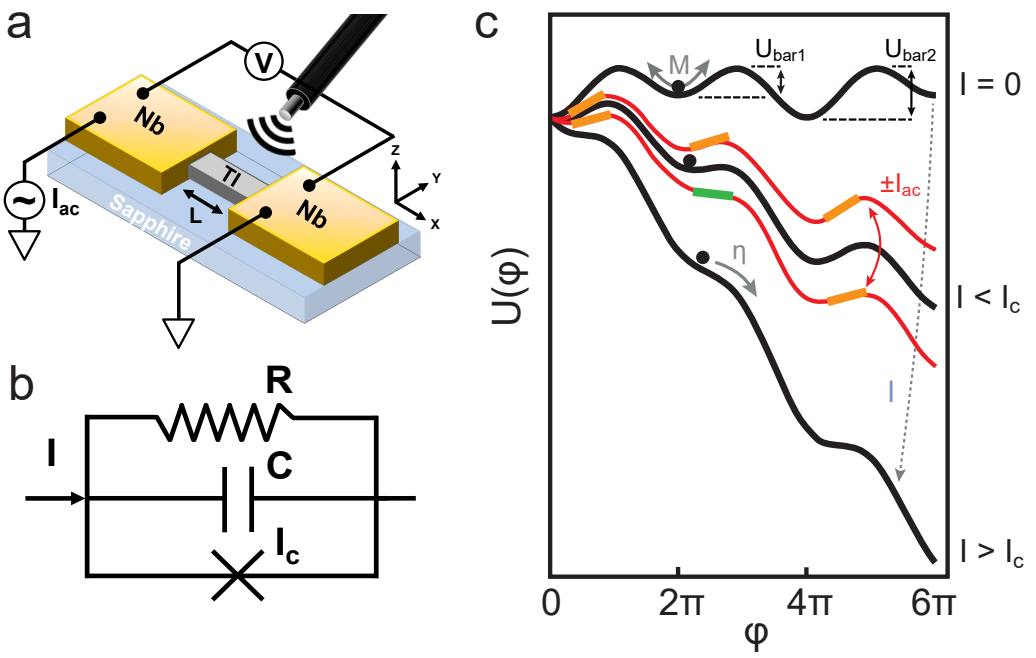

Figure 2.6: RCSJ model an washboard potential in of S-TI-S junction. a, Schematic of the measurement setup of a TINW Josephson junction with wiring and microwave antenna. **b,** RCSJ circuit diagram consisting of a resistor R, a capacitor C and a Josephson junction with a critical current I_C. **c,** RCSJ washboard potential $U(\varphi)$ as a function of φ for different values of current I labelled $I = 0$, $I < I_c$ and $I > I_c$ for a particle of mass M with damping η. 2π and 4π periodic current contributions result in varying potential barrier height $U_{bar1,2}$. Increasing the I results in tilting of the potential, which can further be varied by ac-driving I_{ac} that influences the periodic trapping from the varying potential slopes where yellow (green) bars demotes $\partial U/\partial\varphi > 0$ (< 0).

with $V(t)$ and $I(t)$ the voltage across and current through the Josephson junction as well as I_C the critical current. In most cases, particularly in the weak coupling limit, the second higher order term in the first relation can be neglected. The DC Josephson effect described by the first expression is characterized by a non-dissipative tunnel current across the junction with a 2π-current phase relation (CPR) that is proportional to the sine of the phase difference across the barrier, interestingly even in the absence of a external electromagnetic field. The AC Josephson effect on the other hand arises as a consequence of the second Josephson relation, which states that in the presence of a fixed voltage across a Josephson Junction, i.e. in case of $I > I_c$, the phase-difference $\varphi(t)$ will change linearly with time, which in turn results in an AC-current with a frequency proportional to the applied voltage.

2.3.6 RCSJ-model and the fractional Josephson effect

A realistic and reasonably easy to compute description of the key I-V characteristics of a Josephson Junction, e.g. on a TINW (Figure 2.6 a), under experimental conditions of AC and DC driving is the resistively (R) and capacitively (C) shunted Junction (RCSJ)-model (Figure 2.6 b) [41, 50, 51]. Considering the Josephson relations (2.9) and (2.10), the total current I_{tot} across the junction then results from the individual contributions of supercurrent I_S, normal-state contribution I_N and displacement current I_D given by:

$$I_{tot}(\varphi) = I_S + I_N + I_D = I_c \sin\varphi + \frac{\hbar}{2eR}\frac{d\varphi}{dt} + \frac{\hbar C}{2e}\frac{d^2\varphi}{dt^2} \tag{2.11}$$

with R_N the normal-state resistance and C the geometrical capacitance.
Two practically relevant limits can be distinguished by introducing the Steward McCumber-parameter

$$\beta_c := \frac{2e}{\hbar} I_c R_n^2 C. \tag{2.12}$$

which when considering the circuit's resonant behaviour can be seen as a measure of the quality factor Q. When C is vanishing, the circuit is called overdamped ($\beta_c < 1$) and the junction's I-V curve shows no hysteretic behaviour. In the underdamped case ($\beta_c > 1$), I-V curves exhibit a hysteretic response, meaning that when the excitation current is reduced below I_c the voltage only drops to zero once a retrapping current I_R is reached. When introducing the Josephson energy $E_J = I_C \frac{\hbar}{2e}$, the non-linear differential equation (2.11) can be expressed as

$$\left(\frac{\hbar}{2e}\right)^2 C\frac{d^2\varphi}{dt^2} + \left(\frac{\hbar}{2e}\right)^2 R^{-1}\frac{d\varphi}{dt} + \frac{d}{d\phi}(E_J(1 - \cos\varphi - \frac{I}{I_c}\varphi) = 0 \tag{2.13}$$

and resembles that of a driven harmonic oscillator of the form

$$M\frac{d^2x}{dt^2} + \eta\frac{dx}{dt} + \nabla U = 0 \tag{2.14}$$

with mass M and damping η in the potential U also called washboard potential (WP) [51]. Particles in such a washboard potential can reside in stable equilibrium points with vanishing phase-change and thereby a vanishing average voltage drop $\overline{\mathrm{V}}$ when considering the second Josephson equation (2.6) (Figure 2.6 c). An increase of I above I_c, however, makes the particle slide down the WP along intervals of varying slopes as the local minima vanish. This can further be modulated by an external AC driving I_{ac} which eventually can lead to plateaus at integer n multiples of $\hbar\omega_{\mathrm{ac}}/2e$ called Shapiro steps that depend on the interplay of external AC- and DC-driving, as shown in the following [118].

Consider that the response of the system must be equal to the external driving, i.e. $I_{ext}(t) = I_S(t) + I_N(t) + I_D(t)$. In the situation that the junction (temporarily) exhibits a finite voltage in the case of $I_{ext} > I_C$, part of the current obviously has to result from normal or displacement current contributions. This however causes a time variation in I_S based on the second Josephson relation so that for fixed I_{ext} normal and displacement current must respond accordingly. These interdependent changes results in a time-dependent voltage $\overline{\mathrm{V}}(t)$ and a non-trivial response of the Josephson current. For a Josephson junction driven by an AC- and DC-source given as

$$V(t) = V_{\mathrm{dc}} + V_{\mathrm{ac}} \cos(\omega_{\mathrm{ac}} t), \tag{2.15}$$

in the simplest case of $\beta_C \ll 1$ an integration of the second Josephson equation results in

$$\varphi(t) = \varphi_0 + \frac{2e}{\hbar} V_{\mathrm{dc}} t + \frac{2e}{\hbar} \frac{V_{\mathrm{ac}}}{\omega_{\mathrm{ac}}} \sin \omega_{\mathrm{ac}} t \tag{2.16}$$

so that

$$I_{tot}(t) = I_c \sin \left\{ \varphi_0 + \frac{2e}{\hbar} V_{\mathrm{dc}} t + \frac{2e}{\hbar} \frac{V_{\mathrm{ac}}}{\omega_{\mathrm{ac}}} \sin \omega_{\mathrm{ac}} t \right\}. \tag{2.17}$$

Thereby the total current and its frequency are determined by an interplay of both the constant contribution $\omega_{\mathrm{dc}} = \frac{2e}{\hbar} V_{\mathrm{dc}}$ and the sinusoidal phase variation. By converting this expression to a Fourier series with a Bessel function it can be shown that

$$I_{tot}(t) \propto \sin \left[\varphi_0 + (\omega_{\mathrm{dc}} - n\omega_{\mathrm{ac}}) t \right]. \tag{2.18}$$

Thereby it follows that in the case of $\omega_{\mathrm{dc}} = n\omega_{\mathrm{ac}}$ or

$$V_{\mathrm{dc}} = V_{\mathrm{n}} = n \frac{\hbar}{2e} \omega_{\mathrm{ac}} \tag{2.19}$$

with $n \in \mathbb{N}$ the AC-driving ω_{ac} can cause a time-independent response termed Shapiro step [51, 118]. Such AC-driving is typically performed with a microwave source at $\omega_{\mathrm{ac}}/2\pi \sim 1 - 10$ GHz so that steps appear in an experimentally well accessible constant spacing of $\sim \mu V$. Since interestingly this only depends on external driving frequency and universal constants, Shapiro steps are in fact used to define the voltage-standard [51].

Washboard potential with 4π-periodic contribution: Suppression of odd Shapiro steps

It has been suggested that an additional 4π-periodic supercurrent contribution, that in the case of a topologically non-trivial Josephson junctions potentially

stems from gapless MBS, causes a total $I_S(\varphi) = I_c^{2\pi}\sin(\varphi) + I_c^{4\pi}\sin(\varphi/2)$ which could be reflected in the junction's Shapiro response [8, 114, 119]. Again neglecting capacitive contributions (as in most cases justified in experiments), in a 2S-RSJ model with two supercurrent contributions the washboard potential gets slightly modified such that consecutive potential barriers $U_{bar\,1,2}$ vary in height (Figure 2.6 c). Hereby the particle may only be trapped at every second potential minimum so that integer Shapiro steps at twice the separation voltage are dominant and odd steps can vanish [8, 119]. The typical time scale for the phase to adapt to a drive current change is the phase relaxation time $\tau_{\mathrm{J}} = \frac{\hbar}{2eRI_{\mathrm{c}}}$ which results in a cutoff frequency $1/\tau_{\mathrm{J}}$. Thereby Shapiro steps should theoretically appear in the condition of $f_{\mathrm{rf}}\tau_{\mathrm{J}} < 1$ [38]. This intuitively shows that I_cR_N of a Josephson junction must be sufficiently large and the absence of clear step-like features can correlate with the junction quality. Further, with separating $\tau_{\mathrm{J}}^{2\pi} = \frac{\hbar}{2eRI_c^{2\pi}}$ and $\tau_{\mathrm{J}}^{4\pi} = \frac{\hbar}{eRI_c^{4\pi}}$, in total $f_{\mathrm{rf}}\tau_{\mathrm{J}}^{2\pi} < f_{\mathrm{rf}}\tau_{\mathrm{J}}^{4\pi} < 1$ and thereby a sufficiently large 4π-periodic contribution is required to influence the junction dynamics in a way that odd steps are suppressed. Theoretically this effect is robust in the case that f_{rf} and rf power are sufficiently low. Evidence for a 4π-contribution can further be complemented by studying the residual supercurrent at the first resistive node that correlates with $I_c^{4\pi}$ [38]. In cases where coupling to the junctions is difficult to achieve at low rf power Josephson emission experiments can be an alternative [19, 120].

Suppression of the first Shapiro step only

In many previously reported experiments on topological systems where a 4π-periodic contribution was expected only a first missing Shapiro step was observed however [3, 30, 34–38, 40, 121, 122]. In underdamped Josephson junctions, this was shown to be related to hysteresis from capacitive effects [123]. In overdamped junctions, as the case in this work, the 2-RSJ model can be extended to account for thermal effects from Joule overheating to explain this persistence of higher order odd Shapiro steps [38]. Hereby, quasiparticle poisoning (QP), that means parity switching events stemming from interaction with especially unpaired continuum states outside the superconducting-gap that affect many superconducting technologies, is thermally activated. Signatures of a 4π-periodic contribution, despite being expected, can then vanish because the responsible bound state itself that relies on parity conservation is adversely affected. QP and other dynamical transitions particularly at symmetry points close to other bound states or the bulk continuum may alter the phase periodicity and thereby $I_{2\pi}$ and $I_{4\pi}$ in the case that the quasiparticle poisoning time $\tau_{QP} \sim \mu s$ is similar to the

junctions phase relaxation time τ_J [5, 8, 38, 41, 114, 119, 124–127]. Via an increase of the effective quasiparticle temperature T_{qp}, poisoning of the 4π mode from stochastic parity changes then suppresses all but the first step for $\tau_{QP} \lesssim \tau_J$. Estimating the dissipated power in the junction, which was suggested to be an explanation for the varying amount of suppressed odd Shapiro steps seen in different experiments [38], allows qualitative comparison to other works. To improve, QP poisoning could potentially be reduced by breaking time-reversal symmetry via a Zeeman contribution from an out of plane B-field or magnetic impurities, e.g. from Vanadium electrodes, so that the QP continuum gets separated from the sub-gap states by a small magnetic field dependent gap δ_{QP} [38, 128]. Further problematic complications by large parallel capacitance in backgated substrates have been reported, too [129], so careful experimental design is required to mitigate unfavourable effects.

Non-topological origins of missing Shapiro steps

Apart from topological reasons, also some trivial mechanisms have been reported to cause missing Shapiro steps. For instance, simple hysteresis effects in the I-V response due to Joule heating can suppress or hide low order steps. This however can be accounted for by measuring at elevated temperatures [30, 37, 38, 130]. In the case of near unity-transparency, uncommon in experiments with 3D-TI Josephson junctions, non-adiabatic Landau-Zener transitions (LZT) especially at the anti-crossings at ϕ_n = (2n+1)π between in other cases usually well-gapped ABS can cause a response that mimics a 4π periodicity [131]. Particularly in high transparency high mobility InAs the observation of missing Shapiro steps, some consistent with the 4π periodicity of a topologically non-trivial junction, have been reported although the measured system was undoubtedly in a topologically trivial phase [43, 44, 131]. This has been suggested to be caused by mode-to-mode coupling effects governed by spin-orbit coupling and can potentially be suppressed by magnetic fields [44]. In long diffusive SNS junctions with a much denser ABS-spectrum, LZT could in a similar fashion affect the periodicity in unexpected ways [132].

In conclusion, the absence of Shapiro step features is not strictly linked to a 4π-periodic CPR nor, even if such a relation is present, necessarily linked to unconventional physics like MBS. As some alternative explanations exist, reviewed in more detailed elsewhere [41, 43, 133], such experiments can never give conclusive proof, partly because they are based on the hypothesis that $I_{4\pi}$ is unaltered during the experiment, which however could not be true e.g. due to QP poisoning.

Nevertheless, careful considerations can rule out many of the trivial explanations. This motivates why dynamical driving such as Shapiro experiments carried out in the low frequency and power limit serve as a helpful technique to search for evidence for the existence of gapless 4π-periodic bound states in superconductor-TI hybrid devices.

2.3.7 Magnetic field effects: Fraunhofer pattern

Besides microwave irradiation, also magnetic fields can be used to alter the junction dynamics. Due to the finite size of a Josephson junction, particles traversing the junction can pick up a different phase when a magnetic flux is threaded out of plane perpendicular to the current direction. When assuming a homogeneous current distribution, the resulting critical current can be described by the expression:

$$I_c(B) = I_c(0) \cdot \left| \frac{\sin\left(\frac{\pi\Phi}{\Phi_0}\right)}{\frac{\pi\Phi}{\Phi_0}} \right| \tag{2.20}$$

with $\Phi = (2\lambda_L + L) \cdot W \cdot B$, $\Phi_0 = h/2e$ the flux quantum, L the channel length of the junction, W the width of the junction and λ_L the London penetration depth [51]. Minima occur when the junction area A_{eff} encloses one magnetic-flux quantum Φ_0, i.e. $A_{eff} = \Phi_0/B_\perp$, and this pattern called Fraunhofer pattern resembles the optical diffraction phenomena of a slit (see Figure 2.7). This allows insight into the expected and effective junction area and the current-distribution inside the Josephson junction, that is whether it is homogeneously distributed, more SQUID-like with distinct edge-channels or inhomogeneous due to local fluctuations like interface transparency, material inhomogeneities or junction length [108]. Unconventional features like a non-zero first minimum or suppressed odd-index lobes could theoretically also stem from a nonsinussoidal current phase relation and the presence of Majorana zero-modes [134, 135].
Applying a magnetic field in other directions can lead to further interesting consequences such as effects stemming from the topological surface states in TINWs as discussed earlier, finite-momentum cooper pairing [136, 137] or a superconducting diode effect in the presence of strong spin-orbit coupling [9, 138, 139], all which however are beyond the scope of this work.

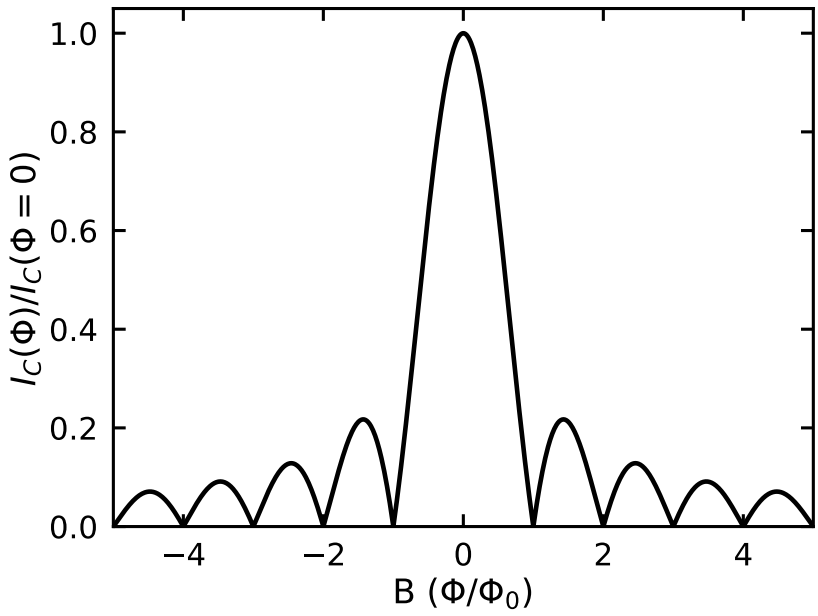

Figure 2.7: Fraunhofer pattern. a, Dependence of the critical current $I_C(\Phi)/I_C(\Phi = 0)$ of a Josephson junction subject to an out of plane magnetic field B in units of the flux quantum Φ_0 showing a characteristic Fraunhofer interference pattern.

Chapter 3

EXPERIMENTAL METHODS

Preparing nanodevices of a delicate quantum material and measuring their quantum transport properties at ultra low temperatures is a feat that requires advanced nanofabrication tools and experimental machinery. This chapter provides a basic understanding of the material and tools used in this work, which is required to understand which challenges have been overcome. This gives a practical context to better understand the later presented experimental results. Further information can be found in dedicated literature on these topics [1, 7].

First the compensated 3D TI material $(Bi_{1-x}Sb_x)_2Te_3$ (BST) and some of its properties are introduced. Since careless patterning of such a surface-transport-dominated material could harm the quality of the surface state and since interface cleaning is necessary for proximitization with a superconductor, treatment conditions as well as some key fabrication techniques used for the preparation of etched TINW devices are discussed. In the end the chapter closes with a concise description of the low-temperature measurement setups used in this work.

3.1 The 3D-TI $(Bi_{1-x}Sb_x)_2Te_3$

Paramount to the success of most solid state physics experiments is the material platform, the physical realm that manifests the effects to be studied. Hence, to evaluate measurement results, thorough understanding of the material is important. In the following, a brief description of the prototypical 3D-TI $(Bi_{1-x}Sb_x)_2Te_3$ (BST) used in this work is given and some remarks on its general electronic transport properties as well as coulomb-disorder are made.

Ternary 3D topological insulator $(Bi_{1-x}Sb_x)_2Te_3$

To obtain a topological insulator, strong spin–orbit coupling is required to cause a band inversion across the bandgap. This suggests that heavy-elements and small-bandgap semiconductors are promising material candidates. Following a ground-breaking proposal of Fu and Kane [140] in 2007, the first experimentally identified 3D-TI was $Bi_{1-x}Sb_x$, studied by angle-resolved photoemission spectroscopy (ARPES) [141]. Following these developments and further theoretical work [142, 143], the Bi-based binary chalcogenides Bi_2Se_3, Bi_2Te_3, and Sb_2Te_3 were predicted to be 3D TIs, too. This was soon confirmed by seminal experimental studies that gave evidence for the existence of the key features of topological insulators - a bulk energy gap together with spin-polarized metallic surface states in a Dirac-like band structures - with various experimental techniques such as ARPES, scanning tunnelling microscopy/spectroscopy (STM/STS) as well as magneto-transport experiments [1]. However, the surface state contribution to transport compared to that of the bulk was low, typically only a few percent for Bi_2Se_3, Bi_2Te_3 or their early successors like Bi_2Te_2Se. Therefore, to advance, it was desired and explored to minimize bulk carriers by doping, thinning, nanostructuring and electrical gating [1]. A key step forward was intermixing alloys of Bi_2Te_3 and Sb_2Te_3 to grow $(Bi_{1-x}Sb_x)_2Te_3$ (BST), a practicable effort considering both compounds have the same tetradymite crystal structure and similar lattice constants [1]. The underlying idea is the following: As shown schematically in Figure 3.1 a, as-grown Bi_2Te_3 is n-type due to antisite defects in the crystal, has a buried Dirac point in the BVB and a Fermi level (E_F) residing in the bulk conduction band (BCB). Sb_2Te_3 however is p-type, with its Dirac point within the bulk gap and E_F in the BVB due to hole-type bulk carriers induced by Sb–Te anti-site defects (Figure 3.1 b). But when combining the two to grow the ternary chalcogenide $(Bi_{1-x}Sb_x)_2Te_3$ (Figure 3.1 c), this allows for beneficial band engineering to shift the Fermi energy E_F and Dirac point into the bulk gap by systematically

compensating donors and acceptors by tuning the ratio of bismuth and antimony [1, 144]. The resulting band structure has been visualized by ARPES for example by Kong et al. [145]. In Figure 3.1 d, when the Sb content is increased to about x = 0.5, both the Dirac point and E_F lie unburied within the bulk energy gap. Typical broad electronic spectra originating from the bulk states together with the single Dirac cone that forms the topological surface state band (SSB) can be seen, the latter indicated by the sharp linear dispersion in the band spectra and the hexagram Fermi surfaces inherited from pure Bi_2Te_3 [74, 146, 147]. In Figure 3.1 e it gets apparent how this depends on the exact composition. When increasing the concentration of Sb added to Bi_2Te_3, E_F exhibits a systematic downshift from the BCB to the BVB via a bulk insulating state. This also has notable consequences for the electronic transport properties, as shown in Figure 3.2 and discussed further below. For a more detailed review of TI materials, established literature is recommended [45–47, 148].

Structural features

$(Bi_{1-x}Sb_x)_2Te_3$ is commonly grown by molecular-beam epitaxy (MBE) as a thin film and consists of covalently bonded quintuple layers with a thickness of about 1 nm where individual layers are weakly coupled via van der Waals force in c-direction with a lattice constant of about 3 nm (Figure 3.1 c). Low roughness, absence of pin-holes stemming from crystal defects and well developed triangular terraces of individual BST-quintuple layers are qualitative indications of good quality material [148, 150]. In this work thin films MBE-grown on (0001) sapphire substrates of about 0.5×0.5 to 2×2 cm^2 have been used. Also (111) Si/SiO_2, (111) SrTiO3, (111) InP or (111) GaAs can be used as epitaxially compatible growth substrates and considerations on which to grow usually center around the resulting quality, i.e. low carrier density and low defect density reflected in higher mobility. However, also the need for backgating (possible on InP, Si/SiO_2) or concerns on unintentional doping (with Si substrates) can be taken into account. Although not atomically flat like the surface of TI-flakes exfoliated from single crystals, the material quality and thickness of wafer-scale MBE-grown TI thin films is very well-controlled, homogeneous and reliable which makes them a first choice for applications at scale. For in-depth discussions on the MBE-growth of BST, especially the material used in this work, References [148, 150] are recommended.

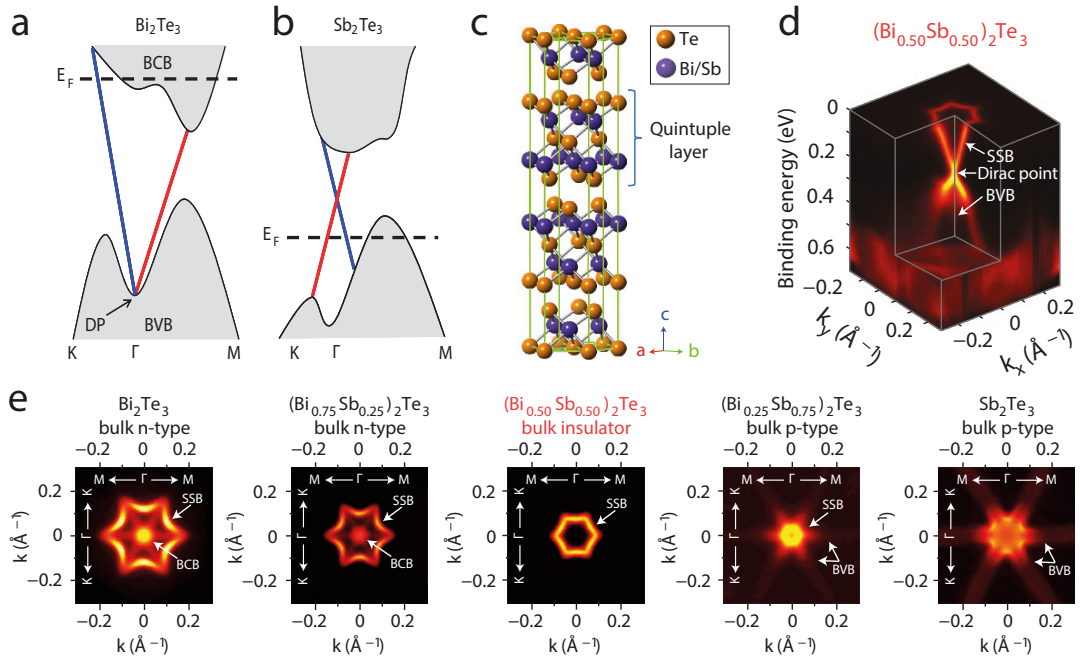

Figure 3.1: Composition dependent bandstructure of $(Bi_{1-x}Sb_x)_2Te_3$. **a,** Schematic of the bandstructure of Bi_2Te_3 with a buried Dirac Point and E_F in the bulk-conduction-band. **b,** Schematic of the bandstructure of Sb_2Te_3 with the Dirac Point in the bulk-band-gap and E_F touching the bulk-valence-band. **c,** Schematic visualization of the tetradymitetype-type BST quintuple layer (thickness $\sim$1 nm) stacking order. **d,** Three-dimensional illustration of the band structure of $Bi_{0.5}Sb_{0.5})_2Te_3$. The topological surface state band forms a single Dirac cone with a characteristic hexagram Fermi surface. **e,** ARPES Fermi surface maps along the K-Γ-M points of $(Bi_{1-x}Sb_x)_2Te_3$ bulk single crystals with increasing ratio of Sb to Bi. E_F exhibits a systematic downshift from the BCB to the BVB via a bulk insulating state at around x = 0.5. Panel a,b, adapted with permission from Springer Nature from [144], Panel c,d,e, from [149].

Coulomb disorder

Throughout the tremendous progress achieved since the advent of TIs, growth and composition related disorder in TI-alloys was considered a challenge that can affect transport experiments. For conceptual reasons mentioned above achieving well-compensated TIs via donor-acceptor-compensation comes hand in hand with the formation of electron-hole puddles that cause Coulomb disorder [151–154]. Similar effects are known in ordinary semiconductors and graphene for many years [155–159] and in TIs, for example for the quaternary compound

$BiSbTeSe_2$ (BSTS2), it has been put forward that from theory considerations potential fluctuations of ∼10 meV could arise just from such coulomb impurities [160]. For BST-NWs, if considering a concentration of Coulomb impurities of $N \geqslant 10^{18}$ cm^{-3}, the coulomb potential fluctuation Γ is claimed to be potentially on the order of Δ_{sub}, with Δ_{sub} being the NW's subband gap [154]. Experimentally, electron-hole puddles have been observed by STM for example in Mn- and Ca-doped Bi_2Te_3, Bi_2Se_3 [161] and in BSTS2, where from optical spectroscopy bulk-puddles have been found to have a size of 0.1–3 μm [162, 163]. In cleaved BSTS2 crystals studied by STM, Knispel et al. found surface potential fluctuations on a length scale of ∼50 nm with Γ = 8-14 meV at 5.5 K [164]. However, most of these reports focus on bulk crystals, and for thin films and more so nanowires, the situation is expected to be much more favourable. Due to the different aspect ratios and reduced bulk-contribution as well as additional screening effects caused by the metallic surface state, puddle formation is anticipated to be suppressed [165] and in devices for transport studies, metallic gates and electrodes are expected to further screen such potential fluctuations favourably [154]. Nevertheless, defect chemistry and engineering remain important topics in TI research that need to be taken into account [45].

Electronic transport properties

In total, the non-trivial defect landscape in TIs is eventually reflected in their mesoscopic transport properties. Considering the electron mobility for example, in BST on sapphire it usually doesn't exceed $\mu \sim 1200$ cm^2/Vs in the commonly available material, with ℓ_Φ ∼120 nm as found by Yang et al. [166, 167]. In Bi_2Se_3, one of the most well-ordered materials of the Bi-compound family, one can find $\mu \leqslant 2000$ cm^2/Vs, ℓ_{mfp} ∼50 nm and a phase coherence length of ℓ_Φ ∼1 μm. For the most insulating TI to date BSTS2, a surface mobility $\mu \sim 2900$ cm^2/Vs was achieved with a surface carrier density of $n_{2D} = 1.5 \times 10^{11}$ cm^{-2}. Typically found carrier densities of $n_{2D} \leqslant 1 \times 10^{13}$ cm^{-2} are considered bulk insulating, which can be derived from band calculations, while $n_{2D} \leqslant 1 \times 10^{12}$ cm^{-2} has not been observed for BST so far, likely due to residual carriers originating from aforementioned impurity states [165].

A practical way to judge on how dominant the topological surface state contribution is to the total transport is to look at the temperature dependence of the electrical conductivity. For bulk-insulating TIs, at low temperatures the contribution of the bulk should be suppressed since E_F resides within the bulk-band gap. When considering the total sheet conductance to be a sum of a thermally activated bulk

conductance and a metallic surface conductance $G^{total}(T) = G^{bulk}(T) + G^{sur.}(T)$ with $G^{bulk}(T) = t\sigma_{0,b} \exp\left(-\frac{E_g}{k_B T}\right)$, with thickness t of the TI, $\sigma_{0,b}$ as the high temperature conductivity of the bulk, E_g the bulk gap, Boltzmann constant k_B and temperature T, G^{total} is dominated by $G^{sur.}$ for low temperatures $k_b T < E_g$ [168]. This results in the typically observed flat to increasing resistance during cool-down found in bulk insulating TIs like BST and BSTS2 and allowed to show that the surface state contribution e.g. in BSTS2 dominates strongly in samples of <100 nm thickness and at low temperatures [151, 169–171].

These transport properties, important to be considered when selecting material for device fabrication, usually depend strongly on the exact stoichiometric composition. For BST, Zhang et al. for example showed how different Sb-contents change the position of the Dirac point (DP) with respect to BVB and E_F (Figure 3.2 a,b), which results in a change of the systems sheet-resistance by up to a factor of 4 (Figure 3.2 c) [144]. This most dominantly originates from a change in the carrier density n_{2D} by more than one order of magnitude (Figure 3.2 d), but also electron mobility μ increases significantly when E_F is close to a well unburied DP (Figure 3.2 e). Figure 3.2 f shows the $R(T)$-behaviour of various compositions. As discussed above, the flat to increasing resistance upon decreasing temperature occurs because thermally activated bulk-carriers are frozen out, in stark contrast to a metallic composition where R would just decrease with decreasing temperature due to reduced electron–phonon scattering. This serves as good evidence for surface-dominated transport in these compositions [144, 167].

The abovementioned properties are usually obtained for thin films with a thickness $6 \leqslant t \leqslant 30$ nm. This is not too thick, which would unnecessarily increase the bulk-to-surface ratio and roughness, but also not too thin, since for ultrathin films surface-state hybridization starts to come into play which can cause the material to become a conventional insulator or a two-dimensional quantum spin Hall system [80, 172]. Appearance and transport properties of a typical piece of pristine bulk-insulating BST thin film deemed promising for device fabrication are shown in the supplementary information of chapter 4. Good material shows a morphology with characteristic well-developed quintuple layer step-terraces of ∼1 nm as well as a temperature dependence of the sheet resistance R_{xx} that shows the typical mostly flat but towards low temperature increasing behaviour expected for bulk-insulating TIs. From the magnetic-field dependence of the Hall resistance R_{yx}, typically a carrier density of $n \sim 1.8 \times 10^{12}$ cm^{-2} as well as a mobility $\mu \simeq 600$ cm^2/Vs can be calculated from dR_{yx}/dB at B = 0 T and T = 2 K.

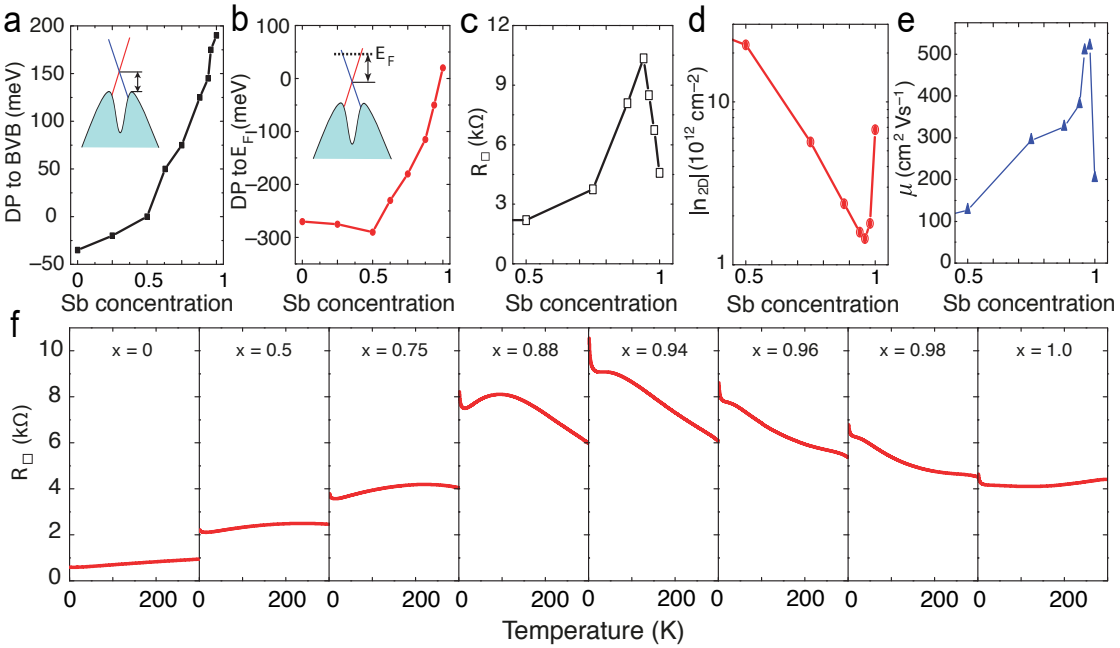

Figure 3.2: Composition-dependent transport properties of $(Bi_{1-x}Sb_x)_2Te_3$ near the Γ point. a Varying relative position of the Dirac point (DP) with respect to the BVB and **b** position of E_F with respect to the Dirac point depending on the composition of $(Bi_{1-x}Sb_x)_2Te_3$. **c,** Sheet-resistance changes by up to a factor of $\sim$4 depending on the Bi-Sb-ratio. **d,** Carrier density n_{2D} can vary by more than one order of magnitude depending on the composition. **e,** Electron mobility μ can be strongly increased depending on Sb-composition and amount of surface-dominated transport. **f,** $R(T)$-curves of various compositions with increasing Sb content from x = 0 to 0.94, highlighting the characteristic behaviour of increasing resistance with decreasing temperature due to the freezing out of bulk-carriers in well bulk-insulating samples. Adapted with permission from Springer Nature from [144].

3.2 Nanodevice-Fabrication techniques

Creating nano-devices from novel materials enables many interesting ways to explore their properties, e.g. by manipulating aspect ratios, probing nanostructures such as NWs or by enabling more complex experiments by adding experimental tuning knobs or physical ingredients, for example when realizing superconducting hybrid devices and asymmetric SQUIDs. This section contains information on device fabrication procedures to prepare top-down etched TINWs from MBE-grown $(Bi_{1-x}Sb_x)_2Te_3$ thin films. The knowledge presented here has been accumulated and refined by both the author as well as various senior members of

Ando-Lab and is subject to continuous further improvement. First, a general fabrication workflow is described, followed by remarks on fabrication related deterioration of TIs. The third section contains key procedures to prepare normal-state as well as superconducting TINW devices. For a full list of fabrication parameters, see the Appendix 7.1.1.

3.2.1 Fabrication process in general

In general, the fabrication work flow to prepare the top-down etched TINW devices reported in this thesis evolves around the steps depicted in schematic Figure 3.3. After obtaining suitable quality BST on sapphire (Figure 3.3 a), cleaning, electron-beam lithography (EBL) as well as wet- and dry-Ar-etching were used to pattern and etch the NWs and trenches that separate individual bond pads (Figure 3.3 b). Next, contact leads were patterned via EBL and Pt/Au or various superconductors are deposited via thermal or sputter deposition after gentle contact cleaning procedures that are described in detail in the next section (Figure 3.3 c). In the case of top-gated devices, the sample was furthermore covered with a protecting dielectric (Al_2O_3) (Figure 3.3 d) and optical laser lithography or EBL and wet-etching was used to open up the contact pads as well as to pattern and deposit the top-gate (Figure 3.3 e). An exemplary result, a normal-state-transport TINW device before topgate deposition is shown in Figure 3.4. Such devices have contacts with a smaller area contacting the NW, here called *finger-contacts*, which usually show higher parasitic capacitive contributions to the contact resistances, but allow to probe shorter channels due to the high accuracy possible when placing them via EBL. Such contacts are suspected to dope the local surroundings with electrons and were found to reduce the gating-efficiency, probably by Fermi-level-pinning [173]. Contacts here called *film-contacts* in comparison have a large contact area between contact-metal and TI film and are far away from the NW, while the NW itself is connected via leads of remaining TI-film. These TI leads are formed by etching and are therefore subject to more strict design limitations, but allow for lower-resistance contact interfaces with vanishing capacitive contributions. Critical fabrication steps are discussed in the next subsection while more general notes on the used standard nano-fabrication processes can be found in section 7.1.1 and in reference [174].

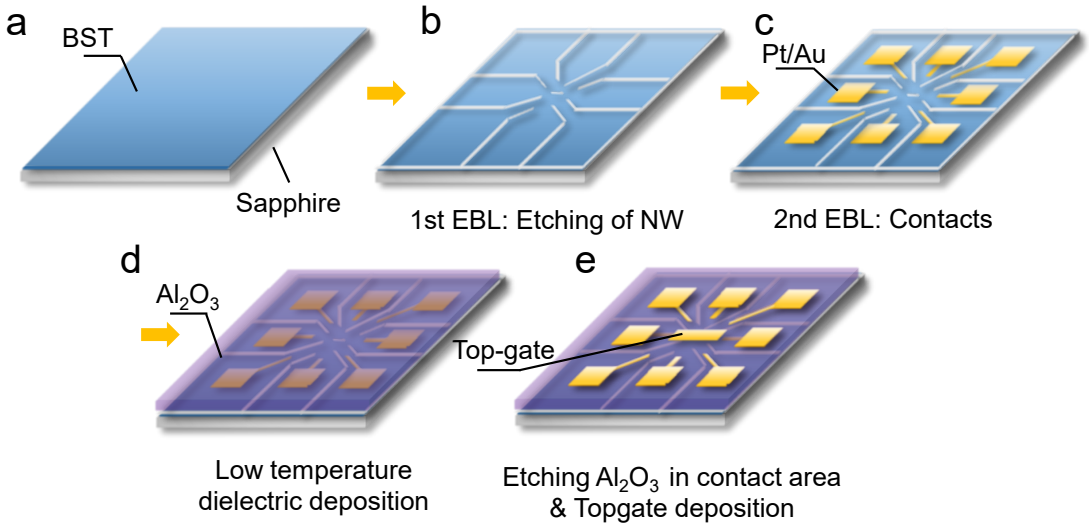

Figure 3.3: Schematic of typical process flow to fabricate TINW devices. a, Fabrication starts with BST on a sapphire substrate. **b,** Electron-beam lithography (EBL), dry- and wet-etching are used to pattern the NWs and trenches that separate individual bond pads. **c,** Contact leads are prepared via EBL and deposited via thermal or sputter deposition after contact cleaning. **d,** Optionally, the sample can be covered with a protecting dielectric (Al_2O_3). **e,** Optical laser lithography or EBL can be used to open up the contact pads for bonding via wet-etching and to pattern and deposit a topgate.

3.2.2 Conserving the properties of Topological Insulators

It has been noticed that for TIs several ambient and fabrication-related conditions can be linked to changes, i.e deterioration, of the transport properties of the material.

- **Oxidization**
  Though very important for devices with large surface to bulk ratios, i.e. nanowires, and contact interfaces, especially to superconducting electrodes, the degree and speed of oxidization of TI-surfaces is barely understood [175]. In early reports, Bi_2Se_3 and Bi_2Te_3 appeared to have a likely self-limiting oxidization that happens comparably slow on experimental relevant timescales, but consecutive studies reported conflicting findings and interpretations [145, 176–183]. Initially it was anticipated that BST would behave similar to these two, but first studies on BST indicated a much different behaviour. Volykhov et al. found for cleaved crystals of Sb_2Te_3 investigated with ARPES and DFT a fast surface oxidation under ambient conditions, rapid reaction with molecular oxygen and slow reaction with water [175]. Reaction with water was also observed in our samples which

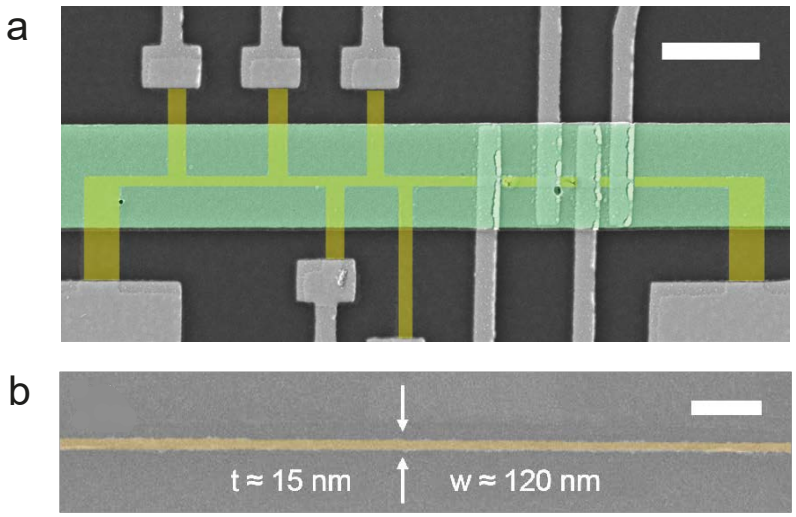

Figure 3.4: Typical etched TINW device for normal-state transport experiments. a, False-color scanning electron microscope (SEM) image of a TINW device (yellow) on sapphire (black) with finger- and film-contacts (light-grey) covered with a dielectric and a topgate (green). **b,** Zoomed SEM image of an etched TINW with thickness t=15 nm, width $w \sim 100$ nm and a side-wall roughness of <10 nm before contact deposition.

when exposed to H_2O over the course of days became quasi-transparent. In humid air, Sb_2Te_3 is claimed to oxidize by more than 2 nm on the time scale of a few hours, strikingly much faster than other tetradymite TIs [175]. In a consecutive study on $(Bi_{1-x}Sb_x)_2Te_3$ that was able to access shorter timescales, Volykhov et al. find that for typical Sb-rich compositions of BST-crystals, 30 min in only p(O_2) = 0.5 mbar are enough to form a 1-2 nm thick oxide layer on the surface [184]. MBE-grown thin films in comparison are known to oxidize even faster in general [176]. For BST in particular the characteristic step-edges of BST are expected to further promote oxidization from the sides due to dangling-bonds, thus additionally facilitating proliferation of the oxide layer into the material from the sides [185], something that could be investigated by conductive atomic force microscopy [186]. These findings serve as a motivation to reduce oxidization related aging as much as possible, for example by capping films as soon as possible after growth ex-situ, e.g. with ALD-grown Al_2O_3, or by storage in vacuum and PMMA-capping. Even more protective should be in-situ capping without breaking the growth chamber's vacuum, which potentially could be done with Al_2O_3, Se (>120 C° bake-off temperature, which is expected to cause unstudied changes in the material), Te (doping of film to be compensated, very rough on RIE-removal and easily oxidized residues) or Ti/Al

(individually found to diffuse into TIs). Further studies are required to understand the details, but thorough interface cleaning or in-situ deposition of the superconductor [37, 40] can serve as a remedy to form transparent contacts.

- **Heating**
  Elevated temperatures can also facilitate undesired deterioration by accelerating above-mentioned oxidization reactions. Additionally, incorporated Tellurium starts to evaporate, which in consequence increases the Te defect density, adds n-type carriers and slightly changes the whole band structure, i.e. shifting E_F and the position of the Dirac Point due to compositional changes [187]. Fabrication recipes therefore are tuned to lower temperatures, e.g. baking only at < 120 C$^\circ$ or depositing alumina only at 80 C$^\circ$, and metal deposition related heating should be considered.

- **Plasma and electron irradiation**
  Ion-bombardment is reported to be linked to physical damage on unprotected sample surfaces and side walls, which can degrade transport properties like phase coherence length [188–191]. Plasma-exposure also causes exposure to high temperatures, with unknown consequences for uncovered surfaces. O_2-plasma is suggested to form an insulating oxide layer on Bi_2Se_3 [192]. Due to these circumstances, low ion energies as well as short etching times are favoured and potentially damaged side walls are removed with an additional wet-etch. Also electron irradiation during EBL and SEM-imaging is commonly associated with harmful changes to the sample such as ionization damage or hydrocarbon contamination [193]. For this reason, acceleration voltages are preferably kept low ($\leq$ 10 kV) if possible and SEM-imaging is reduced to a minimum.

Altogether, the mentioned fabrication processes commonly result in a slight fabrication-related shift of the Fermi-Energy E_F in the final devices compared to the pristine material. For example, the procedures described in subsection 7.1.2 are empirically found to cause a shift of E_F towards p-type transport in BST. To be more specific, more conductive n-type samples tend to shift to more insulating n-type behaviour, while insulating n-type tends to shift across the Dirac point to low carrier density p-type transport characteristics. Note that this is not well understood and is material dependent, as $BSTS_2$ and Bi_2Se_3 were reported to shift towards n-type [171, 194]. As a consequence, mostly n-type BST films are selected for device fabrication which, if chosen correctly, shift to be closer to CNP

after fabrication. Starting with p-type insulating films is found to frequently result in more bulk conducting p-type samples after fabrication. This is consistent with the changes caused by aging in ambient conditions and points to similar origins [195].

Process parameters used in this work are based on recipes that were empirically optimized such that a degradation is minimized and the transport characteristics of the final devices remain very similar to the properties of the pristine as-grown material. This is showcased in chapter 4 which reports nearly as-pristine transport properties for a Hall-bar fabricated by exposure to these fabrication conditions.

3.2.3 Key fabrication processes in detail

To ensure reproducibility, most critical fabrication steps developed during this work are discussed and commented on in some detail in the following. Additional notes can be found in 7.1.1.

Protective Al_2O_3 capping

To reduce oxidization of the top-surface as discussed in section 3.2.2, the samples should be capped as soon as possible after growth. This can be done with Al_2O_3 deposited by Atomic Layer Depositon (ALD) that seals off the material from ambient conditions. The capping can be carried out in a way that ensures less than 60 s exposure to ambient conditions, but is more typically done in a time-scale of 2-10 minutes. The reason is that the fastest capping procedure leads to inhomogeneous island-like growth of the Al_2O_3 only on BST's terrace-edges, which does not properly protect the sample. This hints to modifications of the top-surface in atmosphere happening on a minute-time-scale which seems to enhance the used Trimethylaluminium's (TMA) ability to chemisorb to the surface via unbonded hydroxy groups. To comply with practical considerations regarding the fabrication process flow, i.e. heating, cap-removal etch-times and controllability, the Al_2O_3 is deposited with a thickness t = 4 nm at 80 C°. For such a capping procedure it was shown that the transport properties of a sample show no significant changes on a timescale of at least one week when stored at ambient conditions [195]. Therefore, if such capped samples are stored in vacuum or a desiccator, negligible changes on experimentally relevant timescales are expected. For the removal of the Al_2O_3 cap in areas that directly contact the nanowire, Transene-D Aluminium etchant is used just before metallization. Interestingly, Transene-D is found to be quite selective towards BST as no change

in height or appearance was measured for BST exposed to the commonly used conditions for up to 15 minutes. These findings are in agreement with other reports that highlight Transene-D's good selectivity towards elements with similar properties compared to Bi, Sb and Te [196] and allow to use Transene-D for e.g. $\sim$10 s to remove a protective Al_2O_3 cap of $\sim$4 nm without harming the material itself notably (see 7.1 for further details).

Transfer in Nitrogen atmosphere

To form good superconducting contacts, the interface between electrode and material should be as clean as possible. Thereby exposure of the contact areas to air after development and Al_2O_3 cap removal and potential reoxidization should be minimized. This can be achieved by a process that involves transferring the sample to the metal deposition chamber in a N_2-atmosphere by using a $Sigma - AldrichAtmos$ bag (Z564451). For further details, see 7.1.

Ar-InSitu-Cleaning

Cleaning surfaces in situ with Ar-ions right before contact deposition is a commonly used technique to promote high quality interfaces between superconducting- or normal electrodes and the material [197–200]. Ar-atoms are ionized in a plasma in the UHV-environment of the deposition machine and accelerated towards the sample surface, similar to an Ar-plasma dry etch, just with much lower energies. In this way adsorbates are removed and a gentle milling of the first few oxidized layers of the material can be achieved. Literature suggests that for Bi_2Se_3 and Bi_2Te_3 a self-limiting oxide of thickness of 1-2 nm could be expected, while for BST, which is much less well studied, it could be slightly thicker (2-3 nm) on experimentally common time-scales [175, 179, 184].
To test the effectiveness of Ar-InSitu-cleaning for BST, the consequences of removing 1-2 nm of material from the surface in-situ have been investigated for the available Mantis UHV sputter deposition machine. Devices consisting of two gate-tuneable Hall-bars in series were fabricated, while one channel was treated with the to be tested cleaning procedure and the other channel was kept pristine. Transport experiments remained inconclusive due to considerable variations in the results, but already from simple imaging it became obvious that even low power insitu Ar cleaing at 30 s or longer led to visible surface modifications that were deemed detrimental. This motivated to reduce the cleaning times and to only focus on the removal of adsorbates. Further details can be found in section 7.1.

Superconducting Contacts

The best way to form reliable and highly transparent superconducting junctions on BST is still subject of research. A promising route was realized by Bai et al., who found that Pd-electrodes deposited on BST react with it, thereby forming a $PdTe/PdTe_2$-like phase that is a superconductor (denoted S') on its own. This layer forms a quasi-epitaxial interface with the remaining BST, resulting in a highly transparent S-S'-TI-S'-S interface with a T_C of $\sim$1 K [30]. Considering challenges to control the diffusion in this approach, the here reported work focused on conventional contacting with typical superconducting contact metals. A list of the combinations tried is listed in Table 3.5 and further details are described in section 7.1. Best results were obtained with Nb (see chapter 4).

It is noted that surprisingly a contact cleaning recipe that resulted in highly transparent contact interfaces for $BSTS_2$ flakes [108] gave unpromising results for BST which suggested not yet understood differences between the two materials. It was suspected that BST and its surface terraces structure are more prone to oxidization compared to the atomically flat and terminated surfaces of exfoliated flakes, a suspicion that was later supported by first emerging reports on the oxidization mechanisms in BST, see subsection 3.2.2 [175, 184]. Only in-situ cleaning together with capping as well as cap-removal just before metallization enabled successful proximitization. Additionally it is put to debate whether sputter-deposition of contacts may be advantageous over thermal deposition since plasma and bombardment could act as a gentle in-situ clean and may overcome mild surface oxidization by soft implantation of Nb into the first few BST-layers, a hypothesis that would be interesting to be confirmed via TEM-studies.

In sum, achieving high quality Josephson junctions on 3D TIs is likely not so much determined by the contact metal as it is determined by details of the contact interface conditions, as also apparent from for example work on fine-tuned in-situ cleaning and sulfur-passivation contact preparation in InAs-NWs [198–200], and by scattering in the channel itself, i.e. materials properties. Also, as reported also for $BSTS_2$ flakes [108] and Graphene [201, 202], the robustness of the induced superconductivity is linked to the system's carrier density which could contribute to well induced superconductivity in more conducting Bi_2Se_3 [38, 137], Bi_2Te_3 [203, 204] as well as in more bulk-conducting BST-samples [37, 40, 174]. This highlights the necessity to report carrier concentrations and gating-curves for thorough evaluation of the situation and points to the need for further answers potentially found in materials science.

SC	Combination	Observations
Nb	Nb	Best results, inconsistent yield, low transparencies & no MAR
	Nb/Au	Same as above, capped for reduced time-dependent degradation
	(Pt/Pd)/Nb	Tried on uncapped films – not working
V	V or V/(Al/Au)	Problems with strain as also seen in flake devices
	Pt/V/(+ different caps)	Difficult to achieve/control narrow JJ-gap from two-step deposition in different chambers of e.g. (sputtered) Pt and (thermal evaporated) V
	Ti/V/(Al)	Add Ti as adhesion buffer layer - Strain problem remains and devices always show several kΩ contact resistance R_c & degradation over time (noticeable not in Ar-box, but during bonding / at ambient conditions – later added Al cap to prevent V-oxidization). Also difficult liftoff, unreliable to get <80nm JJ-gaps
	Ti/Al/V/Al	Ti/V strain issue solved by P. Umesh by adding Al to the stack. BST JJs still show high R_c & aging
	Ti/Al/V/Al/ALD	ALD-capped stack to stop degradation: Probestation R_c still not promising and no SC transition
Al	Ti/Al	Degradation of 2 (MR) + 3 (DF) batches, all with degrading Probestation R_c on timescale of ~1 day - suspecting Ti issue
	Pt/Al	Alloying of Pt/Al: Forms grains (appearing as “holes” in contacts)
	Pt/Pd/Al	Pd added to prevent alloying - Unsuccessfully due to difficult to achieve narrow JJ-gap from multi-chamber sputter + thermal deposition (that also may be dirty despite in-situ surface cleaning).
Pd	PdTe2	Difficult to control diffusion, see Bai et al.
Ta	Ta	Strain problems known from BSTS2 flakes

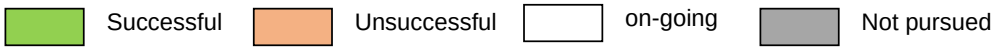

Figure 3.5: List of considered combinations of superconducting electrodes and buffer-layers. This work focused on Nb and Ti/Al, with contributions to tests with V and related stacks, see [174]. Available buffer layer materials were Ti, Pt and Pd as well as superconducting electrode materials Nb, V, Al and Ta. Combinations involving Ti regularly showed insufficient performance, while Pd and Ta were ruled out for etched TINWs based on reasoning derived from other works [30, 205].

3.3 Low-temperature measurement techniques

Modern condensed matter physics experiments are frequently conducted at temperatures much lower than the baseline temperature of outer space ($\sim$2.7 kelvins or -270°C [206]). In the following, the different low temperature measurement setups that were used depending on the required temperature and magnetic field ranges are briefly discussed by outlining their key features.

The typical wiring scheme used for almost all measurements is shown in Figure 3.6. As depicted, using a Josephson-Junction as an example, four contacts of the device are wired to the outside measurement electronics. Two outer contacts carry current in and out which is generated by converting the AC voltage output of a Lock-in via a resistor box. The two inner leads are used to measure the voltage drop across the device area of interest. In this quasi-four-terminal configuration, contributions from the contacts can be neglected. Depending on the setup that the sample was measured in, the signal passes through several stages of filtering and shielding on its way to and back from the sample.
For all experiments involving superconductors as well as experiments which make use of different field directions, dry dilution refrigerators (Oxford Instruments TRITON 400) with a base temperature $\sim$8-30 mK and equipped with 6/1/1-T superconducting vector magnets were used. Detailed descriptions on the operation principles of such systems are widely available in literature [207, 208]. For a more general discussion on the operation principles of dilution refrigerators, Pobell et al. give an instructive review [209]. To reduce electromagnetic noise, the electrical lines of the fridges are equipped with self-made RC-low-pass filters at room temperature, at the 4 K-plate and with additional RC- and copperpowder-filters at the mixing chamber plate. The fridges are referenced to ground either via a dedicated clean ground or via a series of diodes to enable a filtered non-fluctuating ground connection. The samples were wirebonded to a chip-carrier fitting into a QDevil sample holder with further on-chip RC-filtering [210] and line-filtering in the fridge [30]. Current and voltage are measured with a low-frequency lock-in technique, widely discussed elsewhere [211], at low frequencies around 13.37 Hz using NF Corporation LI5640, LI5640 or Stanford Research SR830 and SR860 lock-in amplifiers. For Josephson-Junction experiments, a DC current is superimposed by using a DC voltage source (Keithley 2450) and converting its DC output to a current via a 10 MΩ resistor. In experiments with gating, the gate voltage was applied by using a Keithley 2450 connected via 1 GΩ resistor to limit leak currents.

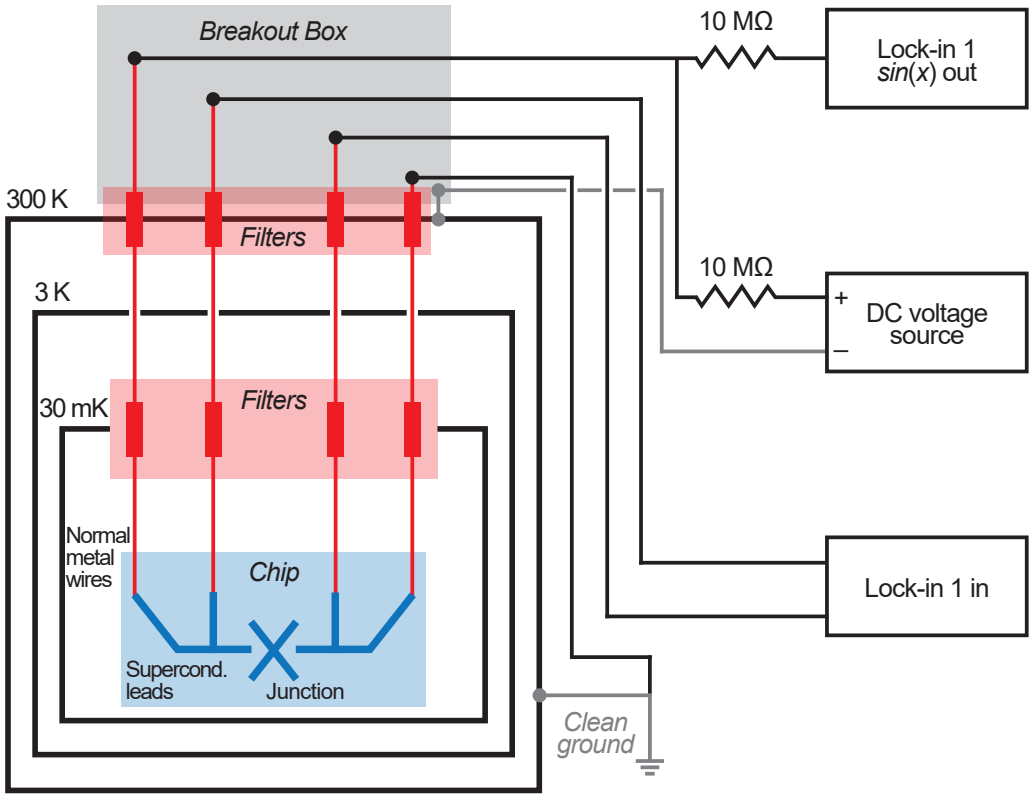

Figure 3.6: Typical measurement setup for low-temperature transport. Schematic of the minimum electronic wiring and filtering in a quasi-4-terminal measurement in a dry dilution refrigerator. Four contacts of the sample are connected via various stages of shielding as well as electronic and thermal filtering to the outside measurement electronics, consisting of Lock-in amplifiers and DC-voltage sourcemeters. The sample resides close to the coldest point of the dilution refrigerator, the mixing chamber ($T \leqslant 30$ mK), which is surrounded by the inner vacuum chamber (IVC, $T \approx 3$ K) and the outer vacuum chamber (OVC, $T \approx 300$ K).

Experiments which benefit from stronger magnetic fields and relaxed temperature needs have been carried out in an Oxford $HelioxVL$ ^{3}He cryostat, a system that can be operated in a temperature range from 0.25 K to about 30 K and with fields up to 13 T. Here, a top-mounted RC-filter box is used to reduce electromagnetic noise. Further operation principles of this low temperature system are described in more detail elsewhere [212]. The most simple transport measurements like Hall-characterization of films were performed in a Quantum Design Physical Properties Measurement System (PPMS), a fully automated measurement setup reaching temperatures of 2-400 K which is equipped with a 9 T magnet

[213]. It is noted that the systems grounding conditions make the measurement of nanowires difficult as electric discharge can be a problem.
For experiments with high-frequency radiation fed to the sample to investigate the Shapiro-response, a R&S SGS100A microwave source was used to provide a RF signal of typically 1-10 GHz which is routed via an unfiltered stainless steel coax radio-frequency-line (RF-line) to a bond-pad of the chip carrier or an antenna a few centimetre away from the sample. From there the signal is radiated into the sample chamber, thereby affecting the devices. To reduce noise from outside the fridge, a DC-block or band-pass filter can be added on the rf-connector at which the microwave source is attached to the fridge. Further details of the wiring, filtering and thermalization of the used equipment have been discussed earlier elsewhere [30].

Chapter 4

TOP-DOWN FABRICATION OF BULK-INSULATING TINWS FOR QUANTUM DEVICES

4.1 Introduction

Topological Insulators are of fundamental interest as they host peculiar topological physics, can be useful in spintronic applications and can allow studies on Majorana states that could enable technology for fault-tolerant topological quantum computing [1, 7, 14]. One route to observe Majorana bound states (MBS) is to reduce the dimensions of a 3D TI into a NW. As a consequence of quantum confinement of the 2D Dirac surface states, quasi-one-dimensional (1D) topological surface state (TSS) subbands arise and by means of a parallel magnetic field the system can undergo a transition to a topological phase which is expected to be much more robust compared to competing material platforms [6]. The resulting spin non-degenerate gapless TSS mode can, when coupled to a s-wave superconductor, give rise to the formation of MBS which should be reflected in e.g. a 4π-periodic contribution to the supercurrent of a S-TI-S Josephson junction [8]. The crucial ingredients, existence and control of the 1D TSS mode as well as robust induced superconductivity, are thereby milestones on the way to further advanced probing of MBS in 3D TIs. These concepts are realized best in materials of highest quality to benefit from clean transport and contact interfaces. Experiments should happen close to the Dirac point of a bulk-insulating system to reduce unwanted trivial contributions and it is desired that the developed platform is compatible with next-generation MBS detection proposals [4].

Earlier work established the preparation of TINWs by various techniques such as Vapour-Liquid-Solid (VLS) growth [23–27], exfoliation of a bulk single crystal [28, 29], sandwiching between different materials [30], selective-area-growth (SAG) [31, 32] or top-down etching of a 2D film [33, 34] and reported a multitude of evidence for the existence of discrete TSS subbands. However, bulk contribution especially in the early binary TI compounds tends to be significant and tuning the chemical potential to the charge neutrality point (CNP) of the Dirac dispersion is rarely achieved. Furthermore for a long term perspective, few existing reports meet the requirement of providing reliable and high material quality in structures that can be patterned, connected and scaled easily [4, 5, 7, 14], a strategy that is also pursued by competing large-scale endeavours based on III-V semiconductor materials [214, 215]. SAG and top-down etching techniques meet these requirements and hence are appealing. However, successful tuning of the chemical potential to the CNP in NWs fabricated with these methods was yet to be reported as in the case of SAG it is difficult to selectively grow for example

$(Bi_{1-x}Sb_x)_2Te_3$ (BST) [144] in a bulk-insulating composition [31, 32] while top-down etching has been applied only to HgTe [33, 34] in which the CNP is buried in the bulk valence band.

In the following work, the first successful fabrication of bulk-insulating TINWs from top-down etching of MBE-grown high quality BST thin films is described [3]. In normal-state transport experiments it is shown that the pristine quality of the material is preserved, that the chemical potential in such NWs can be tuned to the CNP by electrostatic gating and that the peculiar TI-subband physics can be controlled as anticipated, which manifests in gate- and field-dependent resistance oscillations that are consistent with theoretical expectations. Furthermore, superconducting pairing is successfully induced across S-TI-S Josephson junctions on TINWs of varying width and signatures of a 4π-periodic supercurrent contribution previously associated with MBS-physics are observed in Shapiro measurements. This versatile TINW preparation approach only relies on widely accessible technology and is solely limited by independent material improvements. Thereby this work contributes to establish etched TINWs as a promising new platform to advance the search for novel transport phenomena and MBS in TIs.

Reference: Rößler, M.; Fan, D.; Münning, F.; Legg, H. F.; Bliesener, A.; Lippertz, G.; Uday, A.; Yazdanpanah, R.; Feng, J.; Taskin, A. A.; Ando, Y. Top-Down Fabrication of Bulk-Insulating Topological Insulator Nanowires for Quantum Devices. Nano Letters 23 (7), 2846-2853 (2023).

Author contributions: Y.A. conceived and supervised the project. M.R. fabricated the devices, performed the experiments and analysed the data with help from D.F., F.M., H.F.L, J.F. and Y.A. The material was provided by A.B., G.L, A.U., R.Y.R. and A.T. M.R. and Y.A. wrote the manuscript with inputs from all authors.

4.2 Results

4.2.1 Abstract

In a nanowire (NW) of a three-dimensional topological insulator (TI), the quantum-confinement of topological surface states leads to a peculiar subband structure that is useful for generating Majorana bound states. Top-down fabrication of TINWs from a high-quality thin film would be a scalable technology with great design flexibility, but there has been no report on top-down-fabricated TINWs where the chemical potential can be tuned to the charge neutrality point (CNP). Here we present a top-down fabrication process for bulk-insulating TINWs etched from high-quality $(Bi_{1-x}Sb_x)_2Te_3$ thin films without degradation. We show that the chemical potential can be gate-tuned to the CNP and the resistance of the NW presents characteristic oscillations as functions of the gate voltage and the parallel magnetic field, manifesting the TI-subband physics. We further demonstrate the superconducting proximity effect in these TINWs, preparing the groundwork for future devices to investigate Majorana bound states.

4.2.2 TINWs for quantum devices

In the two-dimensional (2D) Dirac surface states of a three-dimensional (3D) topological insulator (TI), the electron spin axis is dictated by the momentum of the electron, a property called spin-momentum locking [45]. This feature is useful not only for spintronics [7] but also for generating non-Abelian Majorana bound states by using the superconducting (SC) proximity effect [17], which may open the door for fault-tolerant topological quantum computing [14]. For the creation of Majorana bound states, reducing the dimensions of a 3D TI into a nanowire (NW) is useful [6]. The quantum confinement of the 2D surface states into a NW leads to the appearance of a series of one-dimensional (1D) subbands, offering an interesting platform for various quantum devices [7]. Although the subband structure with well-defined angular momentum ℓ derived for a circular nanowire cross-section is usually considered for its mathematical ease, the subband structure itself is independent of the shape of the cross-section [83]. To utilize the unique characteristics of these subbands for quantum devices, it is often important to tune the chemical potential to the charge neutrality point (CNP) of the Dirac dispersion [2, 9, 84]. This means that a TINW should be bulk-insulating to become useful.

In the past, TINWs have been fabricated by various techniques: Vapour-Liquid-Solid (VLS) growth [23–27], exfoliation of a bulk single crystal [28, 29], sandwiching between different materials [30], selective-area-growth (SAG) [31, 32], and top-down etching of a 2D film [33, 34]. Among them, the SAG and top-down etching techniques offer a large design flexibility, including the possibility to fabricate curved or branched NWs and NW-circuits, and hence they are particularly appealing as the NW-fabrication techniques for quantum devices. However, there has been no report of a successful tuning of the chemical potential to the CNP in NWs fabricated with these methods. In the case of SAG, it is difficult to selectively grow a TI material, for example $(Bi_{1-x}Sb_x)_2Te_3$ (BST) [144], in the bulk-insulating composition [31, 32], while the top-down etching has been applied only to the TI material HgTe [33, 34], in which the CNP is buried in the bulk valence band. In this paper, we report successful fabrication of bulk-insulating TINWs with a top-down etching of BST thin films, and we show that the chemical potential in such NWs can successfully be tuned to the CNP by electrostatic gating. We further demonstrate that these NWs exhibit the peculiar TI-subband physics and can be used for superconducting devices to search for Majorana bound states.

4.2.3 Preparation and transport characteristics

The etched TINW devices have been prepared from bulk-insulating $(Bi_{1-x}Sb_x)_2Te_3$ (BST) thin films grown by molecular-beam epitaxy (MBE), because BST films are suitable for surface-transport studies [144, 149, 167, 216–219]. Since air-exposure and heating tend to alter the properties of TI films [184, 220, 221], our films are ex-situ capped with Al_2O_3 in an atomic-layer-deposition (ALD) machine immediately after the growth (the film is briefly exposed to air during the transfer) and the process temperatures during the device fabrication are limited to $\leqslant 120$ °C.

Figure 4.1a shows a schematic of our top-down fabrication process. After the patterning with electron-beam (EB) lithography, dry-etching with Ar plasma is performed first to remove unnecessary parts of the BST/Al_2O_3 film. Subsequently, a chemical wet-etching with diluted H_2O_2/H_2SO_4 is carried out to remove damaged edges of the remaining BST to obtain NWs with a smoother edge. Next, the contact areas are exposed by employing EB lithography and removing the Al_2O_3 capping layer in heated Transene Type-D etchant; the exposed BST surface is then cleaned in diluted HCl and further by low-power Ar plasma in the metallization machine. The electrodes (either Pt/Au or Nb) are sputter-deposited in UHV. For our top-gate devices, we deposited a 50-nm-thick Al_2O_3-dielectric in

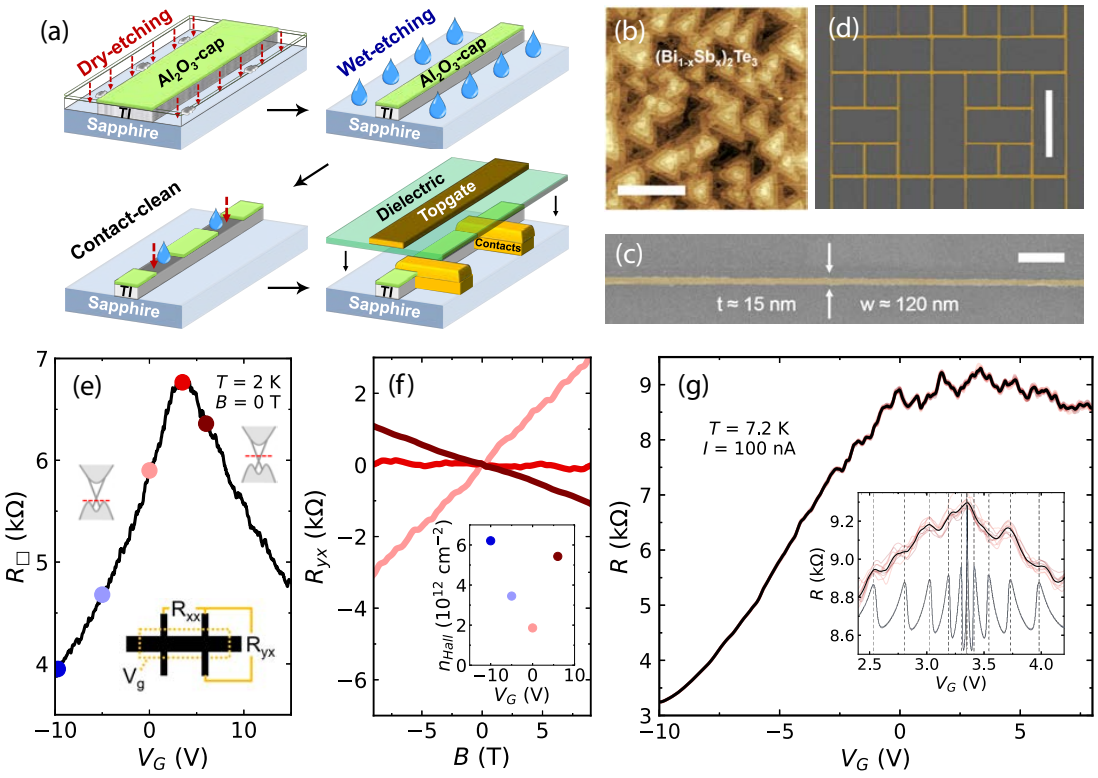

Figure 4.1: **a,** Schematics of the fabrication process: an MBE-grown BST thin film capped with Al_2O_3 is patterned with EB lithography and physically etched with Ar plasma into nanoribbons; consecutive chemical wet-etching is carried out to obtain NWs with a smooth edge; after ex- and in-situ contact cleaning, Pt/Au or Nb electrodes are sputter-deposited. Some devices are encapsulated by an Al_2O_3 dielectric and a Pt/Au top gate is fabricated. **b,** AFM image of the surface of a BST grown on sapphire with characteristic quintuple-layer terrace steps. Scale bar 1 μm. **c,** SEM image of a long NW with a width of 120 $\pm$ 20 nm and a thickness of 15 $\pm$ 2 nm. Scale bar 1 μm. **d,** SEM image of a NW-network. Scale bar 10 μm. **e,** V_G-dependence of the sheet resistance $R_\square$ at 2 K of a 500-nm-wide Hall bar prepared with the aforementioned fabrication process. **f,** B-dependencies of R_{yx} of the same Hall bar at different V_G values that are color-highlighted in panel **e**; inset shows the carrier density n_{Hall} calculated from the Hall coefficient, with which a mobility of $\sim$600 cm^2/Vs can be estimated, confirming the absence of degradation in the fabrication process. **g,** V_G-dependence of the four-terminal resistance R in Device 1 measured between contacts 4–5 (see Supplementary Figure 4.8) at 7.2 K. Thin red lines show the results of 10 uni-directional V_G-sweeps and the thick black line shows their average. Inset shows the $R(V_G)$ behavior near the CNP; dashed vertical lines mark the peak positions expected from theory (blue line) for a gate capacitance C_G = 55 pF obtained from a simple electrostatic model. Reproduced with permission from ACS.

the ALD machine and then fabricated the top-gate electrode with Pt/Au. Further details are described in the Methods section.

An atomic-force-microscopy (AFM) image of the surface of a typical pristine BST thin film used in our work is shown in Figure 4.1b. The well-developed terraces with the step height of ∼1 nm are a signature of high-quality epitaxial growth. As shown in Figure 4.1c, etched NWs can have arbitrary channel lengths with only small fluctuations in the width; the NW pictured here had the width $w \simeq 120 \pm 20$ nm and the thickness $t \simeq 15 \pm 2$ nm (see Supplementary Figure 4.9 for higher-magnification images). With such dimensions, the quasi-1D subbands in the NW have an energy spacing of several meV [7, 26, 85]. Figure 4.1d showcases that this approach allows to fabricate advanced geometries and arbitrary complex networks of bulk-insulting TINWs.

To characterize the properties of the BST film after the NW-fabrication process, we fabricated a relatively wide "ribbon" with a width w = 500 nm, for which the Hall measurement is possible (note, in contrast, the Hall voltage would not appear in a strictly 1D system, and hence the interpretation of the Hall measurement is difficult in a quasi-1D system). The sheet-resistance $R_{\square}$ of such a ribbon sample at 2 K is shown in Figure 4.1e as a function of the gate voltage V_G, and Figure 4.1f shows the magnetic-field dependence of the Hall resistance R_{yx} of this ribbon sample for three V_G values. The peak in $R_{\square}(V_G)$ corroborated with a sign change in R_{yx} gives clear evidence for the CNP-crossing and the bulk-insulating nature of the ribbon after the NW-fabrication process. The $R_{\square}$ and R_{yx} data for V_G = 0 V give the hole density $p = 1.8 \times 10^{12}$ cm^{-2} and the mobility μ = 600 cm^2/Vs, which are close to the values of the pristine material (Supplementary Figure 4.6). These results demonstrate that our NW-fabrication process causes little degradation in bulk-insulating BST.

Once the width of the ribbon is reduced to the "nanowire" regime, which is typically realized for $w \lesssim 250$ nm, the subband physics starts to show up [7, 26]. One characteristic feature is the V_G-dependent oscillation of the NW resistance R. Such a behavior observed in a $w \simeq 150$ nm NW (the device picture is shown in Supplementary Figure 4.8) is presented in Figure 4.1g, where thin red lines show the results of 10 uni-directional V_G-sweeps and the thick black line shows their average. One can see that the pattern of the oscillations is disordered but is essentially reproducible. As shown in the inset of Figure 4.1g for a smaller V_G range near the CNP, reproducible maxima and minima with a characteristic quadratic spacing can be identified. This feature has been elucidated in VLS-grown NWs [26] to be not due to universal conductance fluctuations but to originate from the regular change in the density of states that occurs when the chemical potential

crosses the edge of the quantum-confined subbands. The expected positions of the maxima in $R(V_G)$ can be calculated by using the gate capacitance C_G = 55 pF/m estimated from a simple electrostatic model (see Supporting Information), and the theoretically expected positions are in reasonable agreement with the experimentally observed peaks near the CNP. Although resistance oscillations that are likely due to subbands are also visible away from the CNP, the fitting of these peaks is complicated by the V_G dependence of capacitance and the fact that away from the Dirac point the spacing of subbands is no longer constant in energy. For this NW, we have also estimated the mobility μ from the $R(V_G)$ data and found no evidence for degradation (see Supporting Information).

4.2.4 Phase shift of Aharonov-Bohm oscillations

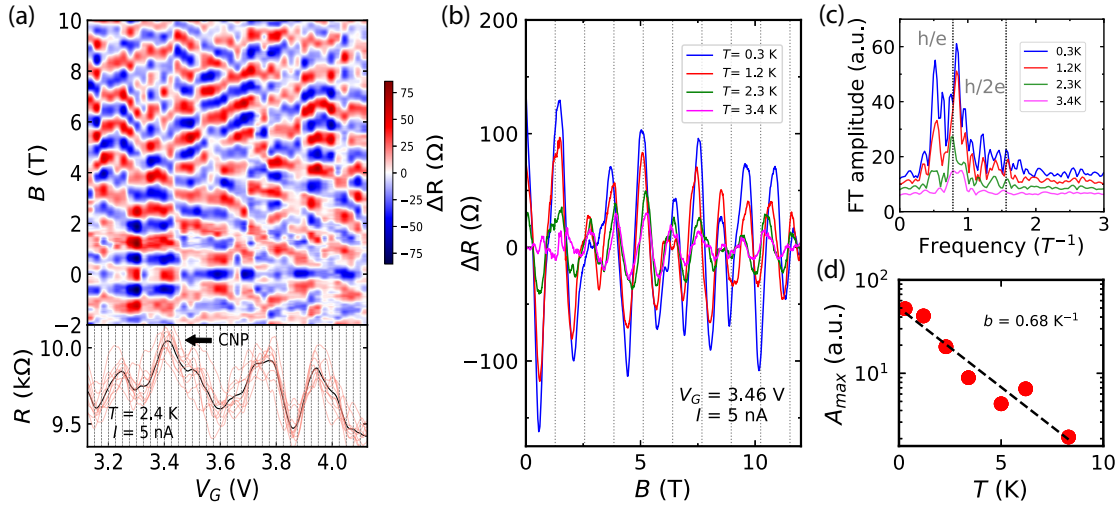

Figure 4.2: **a,** Color mapping of the resistance change ΔR in Device 1 at 2.4 K as a function of V_G and the parallel magnetic field B, presenting occasional π-phase shifts in the AB oscillations. Lower panel shows the $R(V_G)$ behavior at B = 0 in the same V_G range, with dashed lines indicating the positions of individual magnetic-field sweeps. **b,** AB oscillations at various temperatures from 0.3 to 3.4 K measured near the CNP at V_G = 3.46 V. **c,** Fourier transform (FT) of the $\Delta R(B)$ data shown in **b**. Dotted vertical lines indicate the frequencies corresponding to $\Phi_0 = h/e$ and $\Phi_0/2$. **d,** Exponential decay of the FT amplitude A_{max} with T obtained from the data in **c** and supplementary Figure 4.12. Reproduced with permission from ACS.

It is well known [23–25, 28, 32, 33, 183, 222] that the quantum-confined subbands in TINWs also give rise to oscillations of R in parallel magnetic fields with the period of the flux quantum $\Phi_0 = h/e$. This phenomenon is called Aharonov-Bohm (AB) oscillations, because it stems from the flux through the nanowire

cross-section affecting the quantum-confined surface states that are localized at the perimeter of the nanowire [2, 80, 81]. Since the application of V_G leads to oscillations in R as well, the AB oscillations in TINWs are known to present V_G-dependent π-phase shifts [25, 28, 183, 223]. To observe this interplay between V_G and B, we applied a magnetic field B parallel to the NW at various V_G values changed with small steps, and traced the dependence of R on B and V_G. Figure 4.2a (upper panel) shows a color mapping of ΔR in the plane of B vs V_G, where $\Delta R \equiv R(B) - f(B)$ with $f(B)$ a smooth background; the lower panel presents the $R(V_G)$ behavior at B = 0 T for the same gating range, showing that several subband crossings are occurring in this V_G range. Although the periodicity in B is often distorted in Figure 4.2a, the approximate period of the B-dependent oscillations, ∼1.3 T, is consistent with Φ_0 for the cross-section of this NW (150 × 30 nm^2). One can see that sudden π-phase shifts occur at several V_G values, and the occurrence of the sudden phase shifts seen in the upper panel is roughly correlated with the peak-dip features in the lower panel (see Supplementary Figure 4.11 for additional plots). Ideally, a regular checker-board pattern (Supplementary Figure 4.10) is expected in the plane of B vs V_G; however, experimentally the pattern is always distorted [25, 28, 33, 183] which may stem from orbital effects, subband splitting due to gating [2], or disorder [223].

In our NW, the decay of the AB oscillations with increasing temperature is exponential [25, 183, 224] rather than a power law [23], suggesting an approximate phase coherence around the perimeter of the NW [25, 183, 224]. Figure 4.2b shows $\Delta R(B)$ measured in the temperature range of 0.3 – 3.4 K near the CNP at V_G = 3.46 V, and the Fourier transform (FT) of these data are shown in Figure 4.2c. One can see that the dominant oscillation frequency corresponds to the AB oscillations with the period $\Phi_0 = h/e$, and the Altshuler-Aronov-Spivak (AAS) oscillations [225] with period $h/2e$ is essentially absent [23], which is typical for a short TINW [183]. Figure 4.2d demonstrates that the decay of the maximum FT amplitude $A_{\max}$ with temperature is well described by an exponential behavior, $A_{\max} \sim \exp(-bT)$, which has been interpreted to originate from the disorder-induced thermal length L_T that changes as $\sim T^{-1}$ [224]. By putting $\exp(-bT) = \exp(L_{\rm p}/L_T)$ with $L_{\rm p}$ the perimeter length (= 360 nm in the present NW), b = 0.68 K^{-1} obtained in our analysis corresponds to $L_T \approx 0.53$ μm at 1 K, which is shorter than that in VLS-grown TINWs [25, 183, 224]. It should be noted that, despite a subband spacing of a few meV, AB oscillations in our NWs are very much suppressed already at $T \approx 5$ K (see Supplementary Figure 4.12), which suggests that disorder also causes a considerable broadening of subband features.

4.2.5 Proximity-induced superconductivity

To see if our top-down fabricated TINWs can be a viable platform to search for Majorana bound states [6, 84], we have fabricated Josephson junctions (JJs) consisting of Nb electrodes contacting the NW with a small separation (< 100 nm). To ensure bulk-insulation in the NW, BST films with a particularly low carrier concentration were chosen for the NW-fabrication (Supplementary Figures 4.13 and 4.14). The JJ devices, schematically depicted in Figure 4.3a, are measured in a quasi-four-terminal configuration and can be exposed to rf radiation to study their Shapiro response.

Figure 4.3b shows that in our Junction 1, which had a w = 400 nm TI ribbon (see the SEM-image in Figure 4.3c inset), a well-developed critical current I_c is observed at 20 mK but I_c diminishes at $\sim$1 K, and at 1.8 K there is almost no sign of superconductivity. The temperature dependence of I_c allows for an estimate of the interface transparency of the JJ, as was done in similar JJs [30, 37], which gives a relatively low transparency $\mathcal{T}$ of $\sim$0.5 (see Supporting Information). A different method of estimating the interface transparency based on the excess current observed in the I-V curve [226] also gives $\mathcal{T} \approx 0.5$ (see Supporting Information). Hence, there is room for improving the JJ properties by preparing a more transparent interface, which we leave for future works.

When a perpendicular magnetic field B is applied to a usual JJ, the creation of Josephson vortices in the junction leads to the appearance of a Fraunhofer pattern in the B-dependence of I_c [51]. Hence, the Fraunhofer pattern is an indication of the phase winding along the width of the junction, which is not expected when the JJ is formed on a NW having no degree of freedom along the width of the junction. Indeed, whereas the Junction 1 made on a 400-nm-wide ribbon shows a Fraunhofer pattern (Figure 4.3c), the Junction 2 made on a 80-nm-wide NW just presents a monotonic decay of I_c with B (Figure 4.3d). To the best of our knowledge, our Junction 2 is the first successful JJ made on a TINW having such a narrow width of 80 nm. For Junction 1, the effective area $A_{\text{eff}} = 2.3 \times 10^{-13}$ m^2 indicated by the periodicity of the Fraunhofer pattern (9 mT) is consistent with the geometrical area considering the flux focusing effect [40, 108].

4.2.6 Shapiro-measurements

We have also studied the behavior of the Shapiro steps in our JJs under rf irradiation. Figure 4.4 shows color mappings of the differential conductance dI/dV measured in three JJs as a function of the rf power P and the applied dc bias V_{dc} normalized by $\frac{hf}{2e}$ with f the rf frequency; in this type of plots, the horizontal

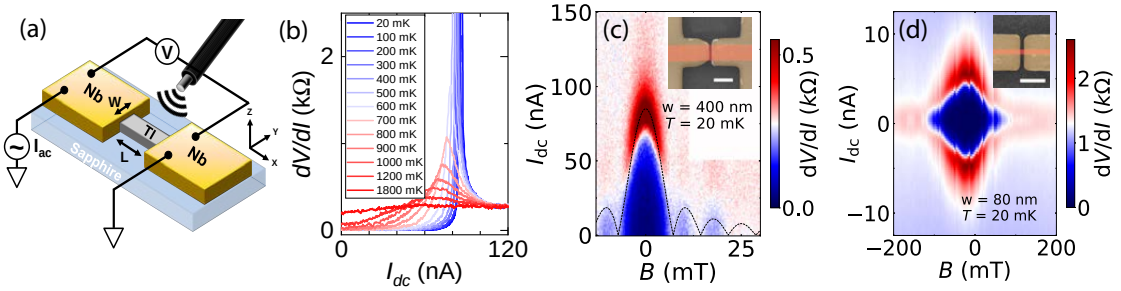

Figure 4.3: **a,** Schematics of the measurements of our TI-based JJ. **b,** Differential resistance $\mathrm{d}V/\mathrm{d}I$ as a function of dc current I_{dc} at various temperatures for Junction 1 made on a 400-nm-wide TI ribbon. **c,** Color mapping of $\mathrm{d}V/\mathrm{d}I$ in the I_{dc}-vs-B plane for Junction 1 at 20 mK, presenting a Fraunhofer pattern; dashed black line shows the theoretically expected pattern for a conventional junction. Inset shows a false-color SEM-image of Junction 1 with TI (red) and Nb (yellow) on sapphire. **d,** Similar mapping of $\mathrm{d}V/\mathrm{d}I$ in the I_{dc}-vs-B plane for Junction 2 made on a 80-nm-wide TINW, showing the absence of a Fraunhofer pattern. Inset shows a false-color SEM-image of Junction 2. Scale bars indicate 500 nm. Reproduced with permission from ACS.

lines appearing at $V_{\mathrm{dc}} = n\frac{hf}{2e}$ correspond to Shapiro steps with index n. Figures 4.4a and 4.4b show the Shapiro response of Junction 1 (made on a 400-nm-wide TI ribbon) at 20 mK for 2.25 and 4 GHz, respectively. The 2.25-GHz data lack the n = 1 step, while the 4-GHz data present all integer steps. At an intermediate frequency of 3 GHz, the 1st Shapiro step was partially observed (Supplementary Figure 4.17). The missing 1st Shapiro step has been reported before for TI-based JJs [34–40] and was interpreted to be possible evidence for Majorana bound states which endow 4π-periodicity to the JJ [12]. However, the Shapiro response alone can never give conclusive evidence for Majorana bound states because other mechanisms of nontopological origin can also cause the 1st Shapiro step to become missing [34, 43, 131, 133]. Our observation demonstrates that our top-down fabrication process does not adversely affect the SC proximity effect in TIs and can be useful for future studies of Majorana bound states.

If one interprets the missing 1st Shapiro step to be due to a 4π-periodic component in the Josephson response [119], the characteristic crossover frequency $f_{4\pi}$ for the appearance of the 1st Shapiro step can be linked to the amplitude of the 4π-periodic current $I_{4\pi}$ via $f_{4\pi} = 2eR_N I_{4\pi}/h$ with R_N the normal-state resistance of the junction [35]. For our Junction 1, we infer $f_{4\pi} \approx 3$ GHz, which gives $I_{4\pi} \approx 26$ nA and $I_{4\pi}/I_{\mathrm{c}} \approx 0.36$.

Of particular interest is how such a Shapiro response changes when the TI-part is narrowed into the NW regime [34, 40, 227, 228], but our Shapiro-measurement

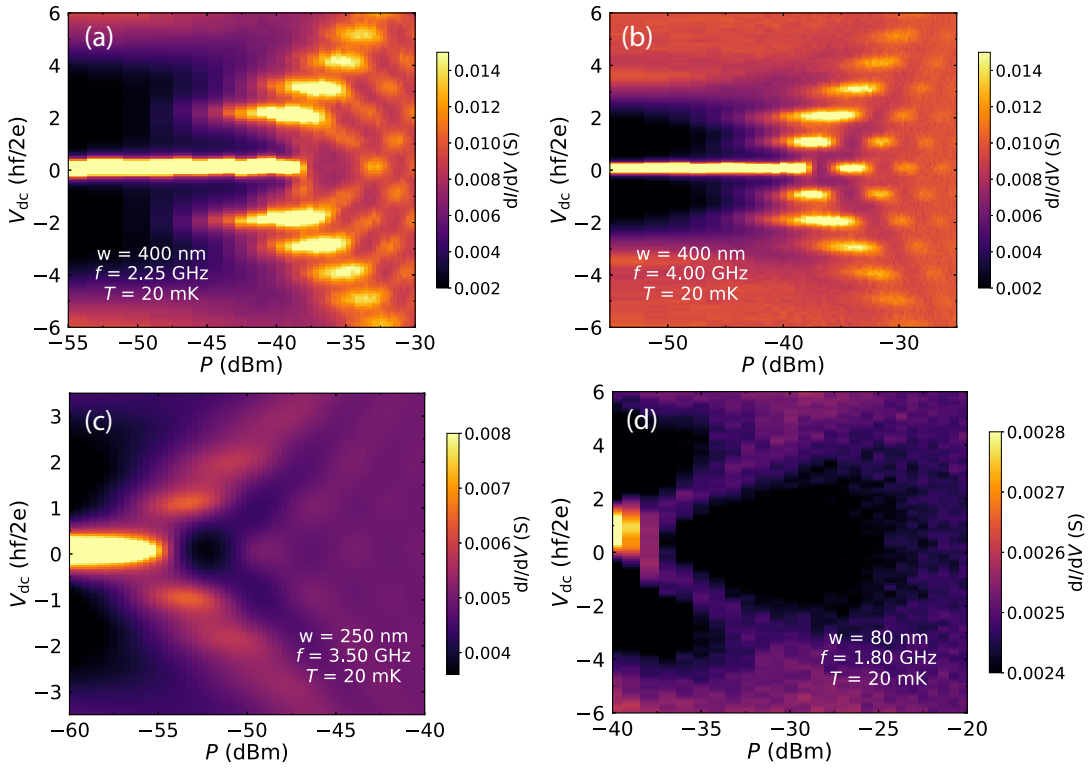

Figure 4.4: Color mappings of the differential conductance $\mathrm{d}I/\mathrm{d}V$ at 20 mK in 0 T as a function of rf power P and dc bias V_{dc} to visualize the Shapiro steps. **a,b,** Data on Junction 1 (w = 400 nm) for f = 2.25 GHz and 4 GHz shown in **a** and **b**, respectively; the n = 1 Shapiro step is missing in **a**, while it is present in **b**. **c,** Data on Junction 3 (w = 250 nm) at f = 3.5 GHz, where the n = 1 Shapiro step is visible. **d,** Data on Junction 2 (w = 80 nm) at f = 1.8 GHz, where no Shapiro step is visible. Reproduced with permission from ACS.

setup was not good enough for this purpose. For our Junction 3 (w = 250 nm), 3.5 GHz was the lowest f at which we could observe Shapiro steps, and the n = 1 step was present (Figure 4.4c). In Junction 2 which had the narrowest NW (w = 80 nm), we detected no Shapiro response at any frequency (Figure 4.4d). This result tells us that the electromagnetic coupling between the TINW and the microwave antenna should be improved, which is beyond the scope of this study. Once a stronger coupling is achieved, it would be interesting to clarify the effect of parallel magnetic fields on the TINW-based JJ to detect the possible generation of Majorana bound states [6, 34]. Trying to detect the microwave emission from a voltage-biased JJ [19, 120] would also be a promising future direction for proximitized TINWs.

4.2.7 Conclusion

In conclusion, we established a top-down fabrication process for bulk-insulating TINWs that are etched from MBE-grown $(Bi_{1-x}Sb_x)_2Te_3$ thin films while maintaining the pristine material's properties. In normal-state transport experiments, characteristic resistance oscillations as a function of both gate voltage and parallel magnetic field are observed, giving evidence that the characteristic TI-subband physics manifests itself in our NWs. We further demonstrate that it is possible to study the superconducting proximity effect in these TINWs by fabricating Josephson junctions with ex-situ prepared Nb contacts, providing the foundation for future devices to investigate Majorana bound states. The process established here is based on widely available clean-room technologies, benefits from the well-controlled properties of high-quality MBE-grown thin films, and enables flexible design of NW geometries. Hence, the results presented here will widen the opportunities for research using mesoscopic topological devices.

4.3 Supplementary Information

Properties of BST before and after the NW-fabrication process

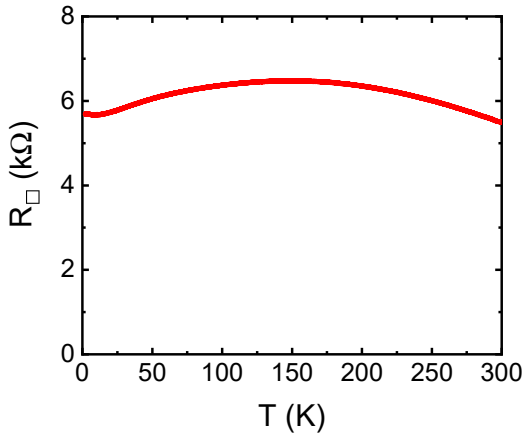

Figure 4.5: a, Temperature dependence of the sheet resistance $R_\square$ of the 500-nm-wide Hall-bar device discussed in the main text.

Figure 4.5 shows the four-terminal sheet resistance $R_\square$ as a function of temperature T in the 500-nm-wide Hall-bar device discussed in the main text (Figs. 4.1 and 4.1f), showing the behavior typical for bulk-insulating $(Bi_{1-x}Sb_x)_2Te_3$ (BST) thin films [144, 217].

Figure 4.6a shows the $R_\square(T)$ behavior of the pristine BST thin film used for this Hall-bar device, and Fig. 4.6b shows the Hall resistance R_{yx} of this film as a

function of the magnetic field B, which gives an electron density n_{2D} = 4.7×10^{12} cm^{-2}. From these data, we extract the mobility μ = 515 cm^2/Vs for the pristine film. This mobility is close to that obtained for the Hall-bar device (600 cm^2/Vs) after carrying out the fabrication process, indicating that there is essentially no degradation in material's quality.

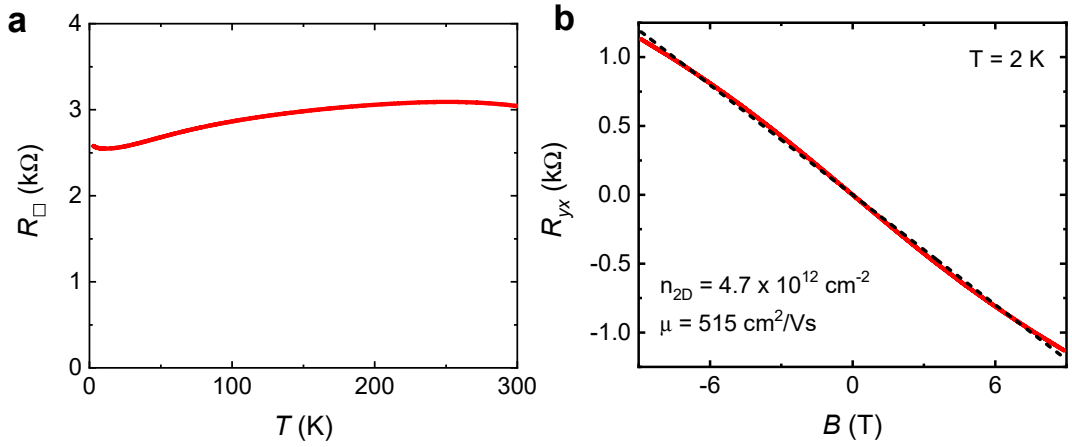

Figure 4.6: **a,** Temperature dependence of the sheet resistance $R_\square$ of the pristine BST film used for the 500-nm-wide Hall-bar device discussed in the main text. **b,** Hall resistance R_{yx} as a function of magnetic field B of the same thin film.

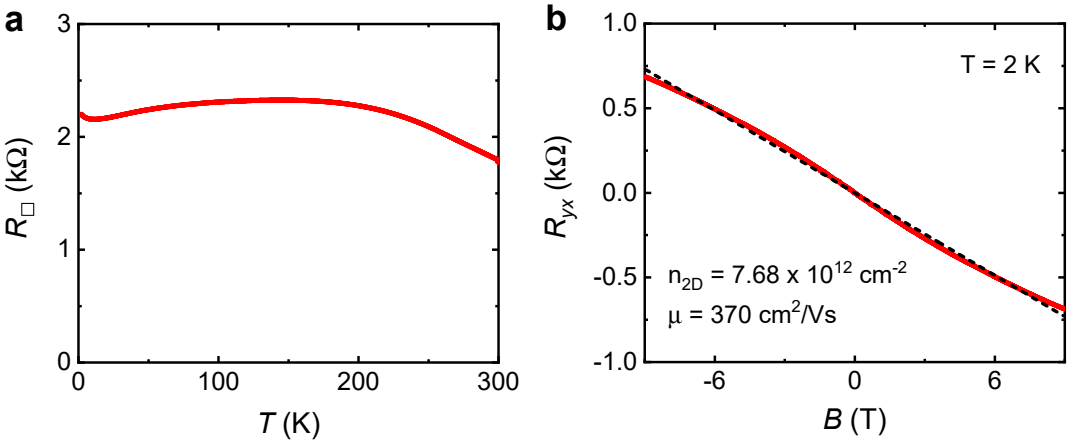

Figure 4.7: Temperature dependence of the sheet resistance $R_\square$ of the pristine BST film used for the gate-tunable Device 1 used for Fig. 4.1g and Fig. 4.2 of the main text. **b,** Hall resistance R_{yx} as a function of magnetic field B of the same thin film.

Figures 4.7a and 4.7b show the $R_\square(T)$ behavior and the $R_{yx}(B)$ behavior, respectively, of the pristine BST thin film used for the gate-tunable nanowire (NW)

Device 1 before fabrication. These data indicate that the pristine film was a typical bulk-insulating BST film with $n_{2D} = 7.7 \times 10^{12}$ cm^{-2} and $\mu = 370$ cm^2/Vs. Note that the chemical potential tends to shift slightly towards the hole-doped side after the fabrication process, resulting in the 500-nm-wide Hall-bar device and the NW Device 1 to become p-type after the fabrication compared to the initially n-type pristine films.

Gate-tunable nanowire device image and wiring

Figure 4.8 shows a false-colour scanning electron microscope (SEM) image of gate-tunable Device 1 together with an electric circuit diagram indicating the four-terminal measurement configuration. In this device, a NW with width $w \approx$ 150 nm (red) fabricated from a 30-nm-thick BST thin film and capped with Al_2O_3 is connected via Pt/Au leads (dark yellow) to the measurement circuit. A Pt/Au top-gate electrode (green) on top of the transport channel is used to vary the chemical potential. The resistance of the nanowire was measured between the voltage contact pair 4–5, while the current was set to flow from contact 1 to 7.

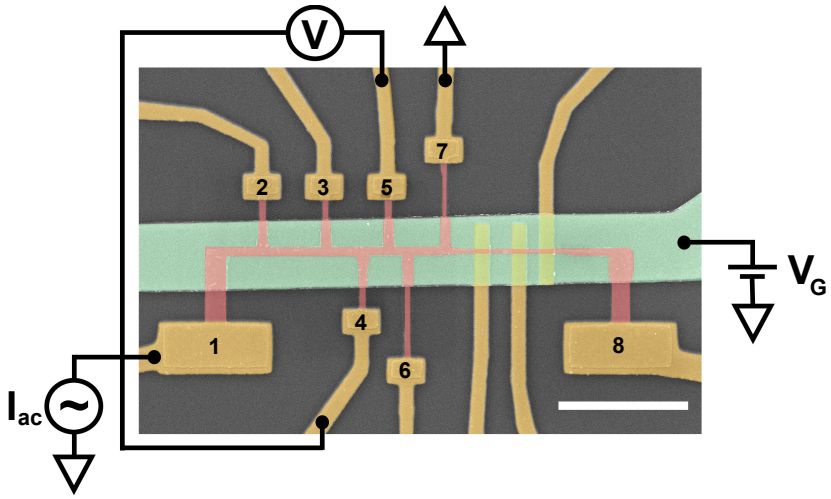

Figure 4.8: False-colour SEM image of Device 1 with schematics of the electrical wiring. The Pt/Au leads are colored in dark yellow, the TINW in red, and the top-gate electrode in green. The four-terminal resistance of the NW was measured between the voltage contact pair 4–5. Scale-bar is 5 μm.

Figure 4.9 shows SEM images with varying magnification of a 130 nm wide and 35 μm long NW after dry- and wet-etching as described in the main text, but prior to the removal of the Al_2O_3 capping layer, contact formation, and deposition of a top-gate. The roughness of the edge is typically around 10 nm per side,

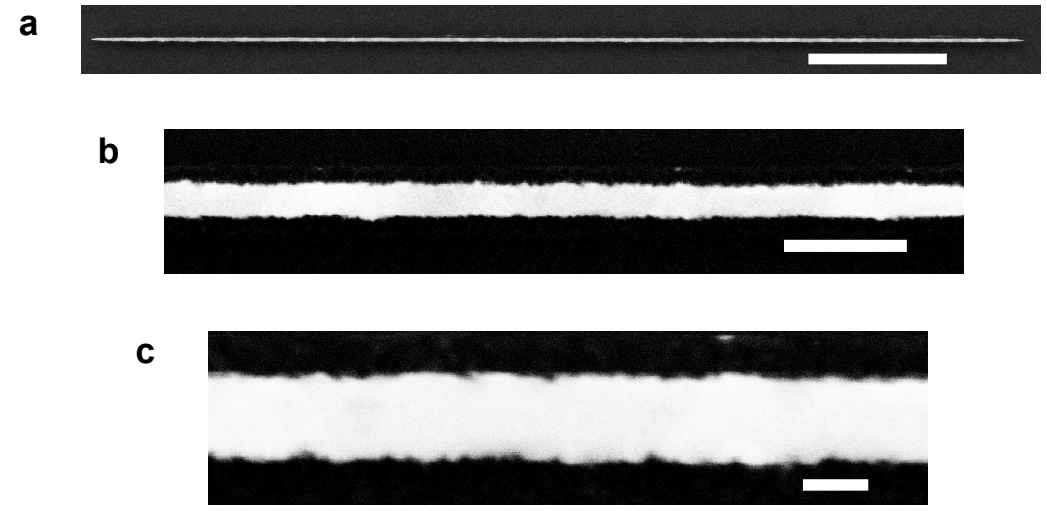

Figure 4.9: SEM images with varying magnification of a 130 nm wide and 35 μm long NW after dry- and wet-etching, but prior to the removal of the Al_2O_3 cap and subsequent fabrication steps. Scale bars indicate 5 μm in **a**, 500 nm in **b**, and 100 nm in **c**.

depending on the duration of the wet-etch as well as on local defects which can affect the lateral etch-speed.

Gate-voltage dependent resistance oscillations in TINW

In TINWs, the resistance oscillates as a function of the gate voltage (V_G) due to the subband structure (see Fig. 4.10b) [26]; the positions of the minima and maxima relative to the charge-neutrality point (CNP) are set by the perimeter length L_{P} and the capacitance of the device, C, as discussed in detail in a previous work [26]. The spacing of the V_G-dependent oscillations is most sensitive to C. This C can be reasonably estimated, thanks to the simple slab-like geometry of the thin-film based devices. By using an electrostatic model for our geometry - including the dielectric environment - and solving the Laplace equation using the finite element method (in which we make a simple assumption that the NW can be modeled as a perfect metal and that the effects of the quantum capacitance can be neglected [26]), we obtain a capacitance $C \approx 55$ pF/m for the parameters of Device 1. This estimated capacitance and the dimensions of the device are used for calculating the expected positions of the resistance peaks (vertical dashed lines) and the theoretically expected oscillations in $R(V_G)$ (solid blue lines) shown in the inset of the main-text Fig. 4.1g. Note that the peak positions depend on the charge density $n \propto (E_F)^2$, such that the spacing of the V_G-dependent oscillations is approximately quadratic in the voltage difference from the location of the CNP.

In the main-text Fig. 4.1g, despite the variations in L_{P} and additional uncertainty in the capacitance, the locations of observed resistance peaks correspond well with the theoretically expected positions, especially for small subband indices ℓ. We note that in the actual NWs studied here, complications arise due to the fact that the scattering-potential landscape in the NW changes with V_G, and this is likely to be responsible for the random but reproducible V_G-dependent resistance oscillations whose amplitude (up to 0.5 kΩ in the main-text Figure 4.2g) is larger than the amplitude of the oscillations due to subband crossings (up to 0.1 kΩ in the main-text Figure 4.2g inset). Nevertheless, the differences in the amplitudes as well as in the typical V_G intervals of these oscillations make it possible to discern the latter despite the presence of the former.

Estimation of the mobility μ in nanowires

Since the Hall resistivity cannot be measured on a NW, we tried to estimate the mobility in a NW based on the $R(V_G)$ behavior. Note that the total two-dimensional carrier density in a TI thin film due to the surface states is approximately given by $n_{2\mathrm{D}}(k_F) \approx 2 \cdot \frac{1}{(2\pi)^2} \cdot \pi k_F^2 = \frac{k_F^2}{2\pi}$, where k_F is the Fermi wave vector on the Dirac cone. From the known band structure of BST [144], we know that $k_F \approx 0.06$ Å^{-1} when the chemical potential is just touching the top of the bulk valence band (BVB). The corresponding hole density in this situation (which we call the threshold hole density $p_{2\mathrm{D,th}}$) is about 6×10^{-12} cm^{-2}.

Experimentally, when the chemical potential touches the BVB, the rate of change in R with respect to V_G becomes weaker; this situation corresponds to the region where the slope of $R(V_G)$ starts to flatten after rapidly decreasing with the sweep of V_G to the negative direction. In high-quality BST thin films, a sheet resistance $R_\square$ of 2–4 kΩ is typically observed in this region [144, 217, 219], which is also the case in our Hall-bar device (see Fig. 4.1e of the main text); namely, the Hall measurement in our Hall-bar device gives $p_{2\mathrm{D}} \approx 6 \times 10^{-12}$ cm^{-2} at V_G = -10 V where $R_\square$= 3.85 kΩ was observed. From $R_\square$= 2–4 kΩ and $p_{2\mathrm{D,th}} \approx 6 \times 10^{-12}$cm^{-2}, one obtains the mobility $\mu \simeq$ 250–500 cm^2/Vs, which is actually the typical surface-state mobility of a high-quality BST film [144, 217, 219].

Based on this knowledge, we tried to make a rough estimate of μ from the $R(V_G)$ data of the NW shown in Fig. 4.1g of the main text, where a flattening of the $R(V_G)$ behavior occurs below $V_G \simeq -5$ V. With $w \approx 150$ nm, $L \approx 650$ nm, and $R \approx$ 5.5 kΩ at $V_G = -5$ V, we obtain $R_\square \approx$ 1.3 kΩ, which gives $\mu \approx$ 780 cm^2/Vs if $p_{2\mathrm{D,th}} \approx 6 \times 10^{-12}$cm^{-2} is assumed as the carrier density. This result suggests that at least no obvious degradation is caused in the process of NW fabrication.

π-phase shift in the Aharonov-Bohm oscillations

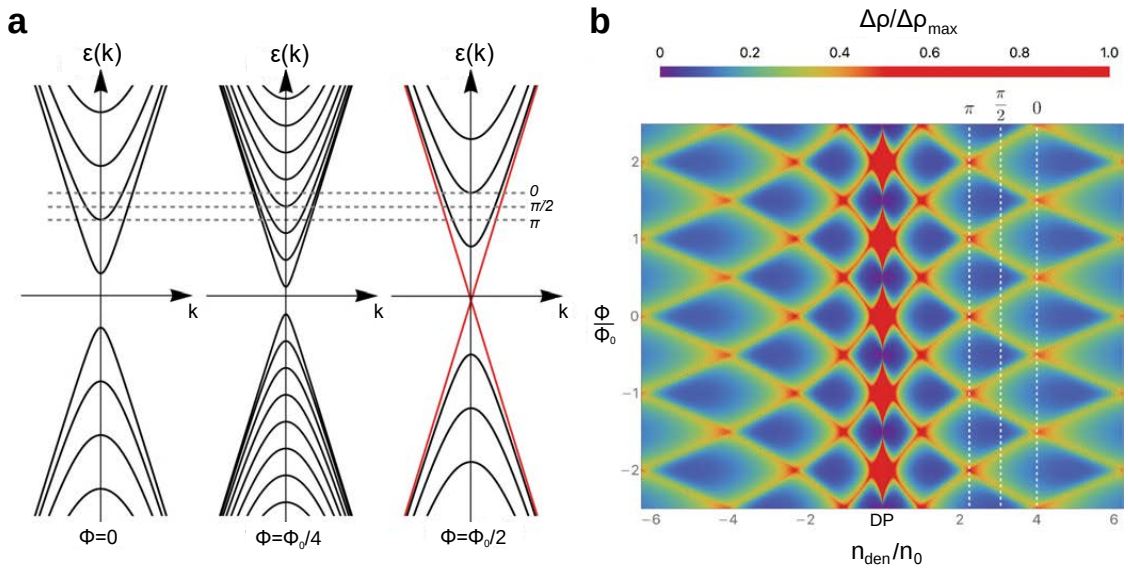

Figure 4.10: **a,** Schematic of the quantized subbands formed in a TINW for the axial magnetic flux Φ of 0, $\Phi_0/4$, and $\Phi_0/2$. Red lines indicate the gapless spin-non-degenerate 1D mode. Dashed horizontal lines mark characteristic positions of E_F relevant for a peak in the resistance oscillations. **b,** Color mapping of the normalized change in the resistivity, $\Delta\rho/\Delta\rho_{\max}$, expected from theoretical calculations as a function of both axial magnetic flux Φ (normalized by Φ_0) and the carrier density $n_{\rm den}$ near the CNP (normalized by the value n_0 at the edge of the first subband). The latter is controlled by gating. White vertical dotted lines denote the three positions of E_F marked in panel **a**. At a fixed E_F, $\Delta\rho$ oscillates with Φ and the oscillation phase shifts depending on $n_{\rm den}$, causing a checker-board-like pattern.

The subband structure formed in TINWs due to the quantum confinement causes the density of states to oscillate strongly with energy or with the axial magnetic flux, which manifests itself in terms of resistance oscillations when E_F or B is swept [80, 81]. In our experiment, both resistance oscillations as a function of V_G (see main-text Fig. 4.1g) and the Aharonov-Bohm (AB) oscillations as a function of B (see main-text Fig. 4.2) were observed. In both cases, the oscillations are mainly the result of the increased scattering rate that arises at the edge of each subband (see Fig. 4.10a). A characteristic feature of the AB oscillations in TINWs is a π-phase shift in the oscillations that occurs as E_F is changed [81] (see Fig. 4.10b).

Owing to the bulk-insulating nature and the gate-tunability of our devices, we were able to investigate the occurrence of such a π-phase shift in the AB oscillations close to the CNP and with respect to features in $R(V_G)$. Figure 4.11 shows the change in resistance ΔR plotted vs the threading magnetic flux Φ (in units of the flux quantum $\Phi_0 = h/e$) close to CNP at selected V_G positions (see inset showing the $R(V_G)$ data in the relevant V_G range). One can recognize π-phase shifts in the oscillations plotted here, although the phase shift is sometimes smeared due to irregularities. Interestingly, the phase shift is not observed when the CNP (which is located at V_G = 3.41 V) is crossed, which is a theoretically expected behavior [6, 223], as one can see in Fig. 4.10b.

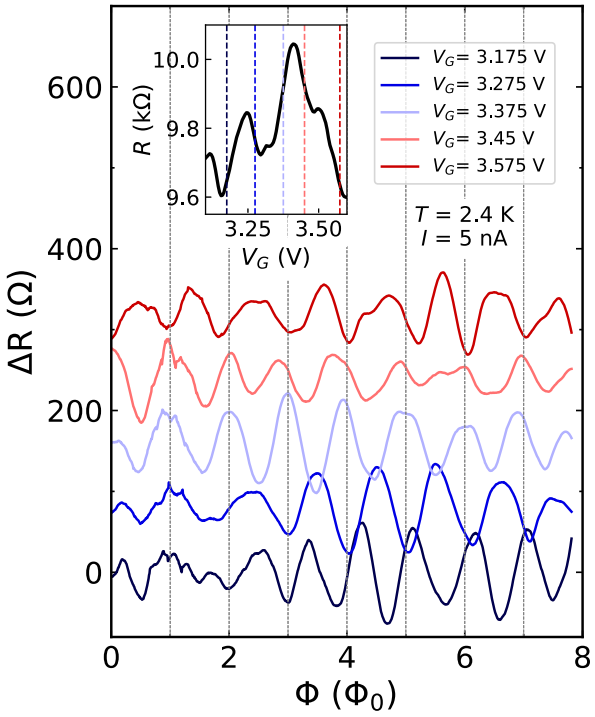

Figure 4.11: a, Resistance change ΔR as a function of magnetic flux Φ (in units of the flux quantum Φ_0) at selected V_G positions showing π-phase shifts in the oscillations. Inset shows the positions of the selected V_G values in relation to the $R(V_G)$ behavior near the CNP.

Temperature dependence of the Aharonov-Bohm oscillations

Complementing the main-text Figure 4.2, Figure 4.12a shows the data of AB oscillations in $\Delta R(B)$ for the full temperature range measured, i.e. 0.3 – 8.3 K, near the CNP at V_G = 3.46 V. Figure 4.12b shows the corresponding Fourier transform (FT) of these data, which are used for extracting the temperature dependence of the maximum FT amplitude $A_{\max}$ plotted in the main-text Figure 4.2d.

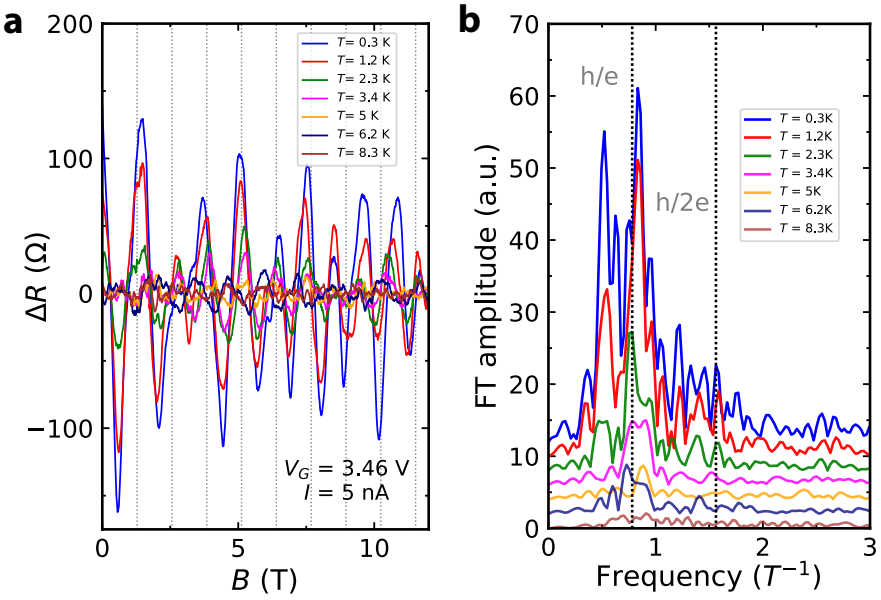

Figure 4.12: **a,** AB oscillations in $\Delta R(B)$ at various temperatures from 0.3 to 8.3 K measured near the CNP at V_G = 3.46 V. **b,** Fourier transform (FT) of the $\Delta R(B)$ data shown in **a**. Dotted vertical lines indicate the frequencies corresponding to $\Phi_0 = h/e$ and $\Phi_0/2$.

Properties of the pristine BST films used for the Josephson junction devices

Figures 4.13a and 4.13b show the $R_\square(T)$ behavior and the $R_{yx}(B)$ behavior, respectively, of the pristine BST thin film used for the Josephson junction 1 before fabrication. A linear fit to $R_{yx}(B)$ gives an apparent carrier density of 1.2×10^{13} cm^{-2}, but this large value is an artifact of the cancellation of the electron and hole carriers on the two surfaces to give a small R_{yx}, which is often observed when the chemical potential is very close the CNP.
Figures 4.14a and 4.14b shows the $R_\square(T)$ behavior and the $R_{yx}(B)$ behavior, respectively, of the pristine BST thin film used for the Josephson junction 2 and 3 before fabrication. These data indicate that the pristine film was a typical bulk-insulating BST film with n_{2D} = 1.8×10^{12} cm^{-2} and $\mu \approx 600$ cm^2/Vs.

Temperature dependence of the critical current in Junction 1

Figure 4.15 shows the temperature dependence of the critical current I_c in Junction 1 (w = 400 nm). Here, I_c was defined as the $I_{\rm dc}$ value at which the junction resistance reaches 10% of its normal-state resistance R_N. Following the analysis of similar TI-based junctions [30], we fit the $I_c(T)$ data to the theoretical formula

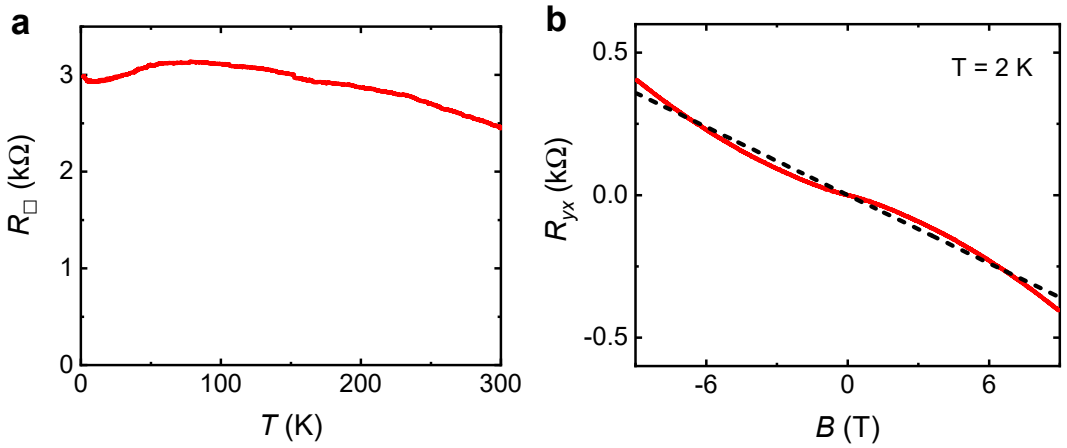

Figure 4.13: **a,** Temperature dependence of the sheet resistance $R_\square$ of the pristine BST film used for the Josephson junction 1, whose results are shown in Figs. 4.3b, 4.3c, 4.4a, and 4.4b of the main text. **b,** Hall resistance R_{yx} as a function of magnetic field B of the same thin film.

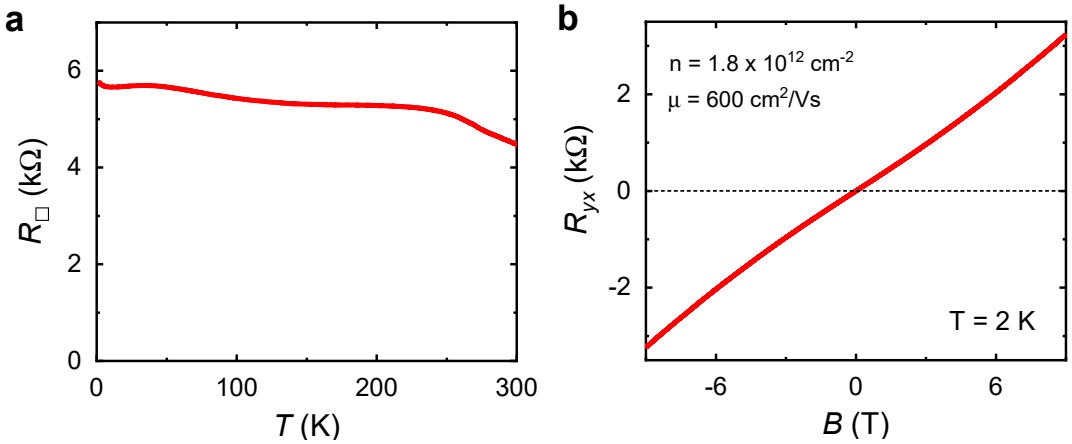

Figure 4.14: **a,** Temperature dependence of the sheet resistance $R_\square$ of the pristine BST film used for the Josephson Junctions 2 and 3 used for Figs. 4.3d, 4.4c, and 4.4d of the main text. **b,** Hall resistance R_{yx} as a function of magnetic field B of the same thin film.

given by Galaktionov and Zaikin [229], and the fit yields the interface transparency $\mathcal{T} \approx 0.5$.

Characteristic parameters of the Josephson-junction devices

The characteristic parameters of the three JJs reported in the main text are listed in Table 4.1. L is the channel length of the JJ obtained from the SEM image, w is

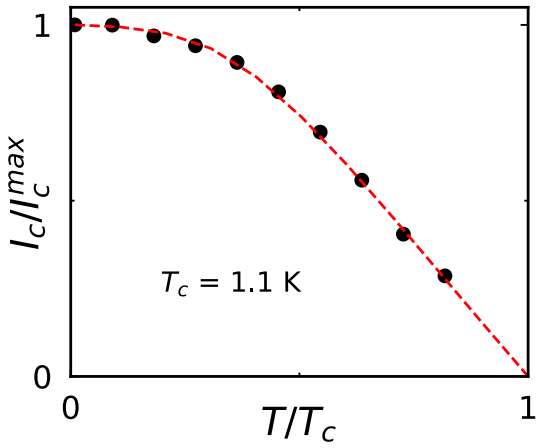

Figure 4.15: Temperature dependence of I_c in Junction 1 obtained from $\mathrm{d}V/\mathrm{d}I$ vs I_{dc} at various temperatures up to 0.9 K. The red dashed line is the behavior of the theoretical formula given by Galaktionov and Zaikin [229] with $T_c \approx 1.1$ K and transparency $\mathcal{T} \approx 0.5$.

the width of the TI part, t is its thickness, I_{c} is the critical current, and R_{N} is the normal-state resistance measured by applying a large dc current $I_{\mathrm{dc}} \gg I_{\mathrm{c}}$.

No.	L (nm)	w (μm)	t (nm)	I_{c} (nA)	I_{e} (nA)	R_{N} (Ω)	$R_{\mathrm{N}}^{I\text{-}V}$ (Ω)	$I_{\mathrm{c}}R_{\mathrm{N}}$ (μV)	$I_{\mathrm{c}}R_{\mathrm{N}}^{I\text{-}V}$ (μV)	Δ_{ind} (meV)	$eI_{\mathrm{c}}R_{\mathrm{N}}/\Delta_{\mathrm{ind}}$	$eI_{\mathrm{c}}R_{\mathrm{N}}^{I\text{-}V}/\Delta_{\mathrm{ind}}$	$\mathcal{T}$
1	70	400	14	86	852	238	242	20.5	20.8	1.25	0.02	0.02	0.5
2	65	80	16	4	22	1770	1763	7.1	7.1	1.1	0.01	0.01	0.5
3	70	250	16	20	213	518	524	10.5	10.5	0.75	0.01	0.01	0.5

Table 4.1: Relevant parameters of the reported Josephson-junction devices.

Figure 4.16 shows the I-V curves measured on these three JJs. The excess current I_{e} is identified from the I-V curve by measuring up to a high bias beyond $V_{\mathrm{dc}} = 2\Delta_{\mathrm{Nb}}/e$, where $\Delta_{\mathrm{Nb}} \approx 1.3$ meV is the superconducting gap of Nb. The linear part of the high-bias I-V curve was extrapolated to $V_{\mathrm{dc}} = 0$ and the intercept on the I_{dc} axis gives I_{e}. R_{N}^{I-V} is the inverse slope at high bias (i.e. $V_{\mathrm{dc}} > 2\Delta_{\mathrm{ind}}/e$) region. In low transparency TI-based JJs containing a series of interfaces S-S'-TI-S'-S, the induced gap Δ_{ind} in S' is the relevant gap for the Andreev reflections at the S'/TI interface that affects the observed I-V curve, and the upper limit of $2\Delta_{\mathrm{ind}}$ can be inferred from the plot of dI/dV vs V_{dc} as the energy scale above which the dI/dV ceases to change with V_{dc}. In the upper inset of each panel in Fig. 4.16, this energy scale is indicated by an arrow. The transparency $\mathcal{T}$ of the interface governing the I-V curve can be estimated from the values of I_{e}, R_{N}^{I-V}, and Δ_{ind} by using the Octavio-Tinkham-Blonder-Klapwijk (OBTK) theory [107, 226], and this estimate gives a relatively low transparency of $\mathcal{T} \approx 0.5$.

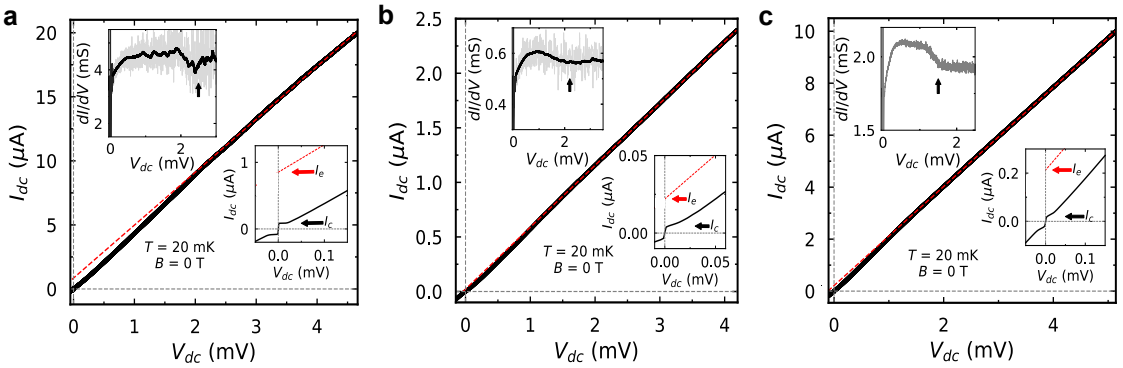

Figure 4.16: **a,b,c,** I-V characteristics of Junctions 1, 2, and 3, respectively, measured at 20 mK in 0 T. The red dashed line is a linear extrapolation of the high-bias region to $V_{\rm dc}$ = 0 V, used for the extraction of the excess current I_e and the normal-state resistance R_N^{I-V}. The lower inset in each panel shows a close-up of the main panel at very low $V_{\rm dc}$, with the red arrow indicating I_e and the black arrow indicating I_c. The upper inset in each panel shows the differential conductance $\mathrm{d}I/\mathrm{d}V$ as a function of $V_{\rm dc}$; thin grey line shows the raw data and the thick black line is a smoothed curve, with the black arrow indicating the upper limit of $2\Delta_{\rm ind}/\mathrm{e}$.

Shapiro-step data for Junction 1 at f = 3 GHz

In the main-text Figure 4.4, we showed the Shapiro-step data only for f = 2.25 and 4 Gz for Junction 1 (w = 400 nm). Figure 4.17 shows the Shapiro-response of Junction 1 at f = 3 GHz as a function of the rf power P and the bias voltage $V_{\rm dc}$. The 1st Shapiro step is partially observed at relatively high P.

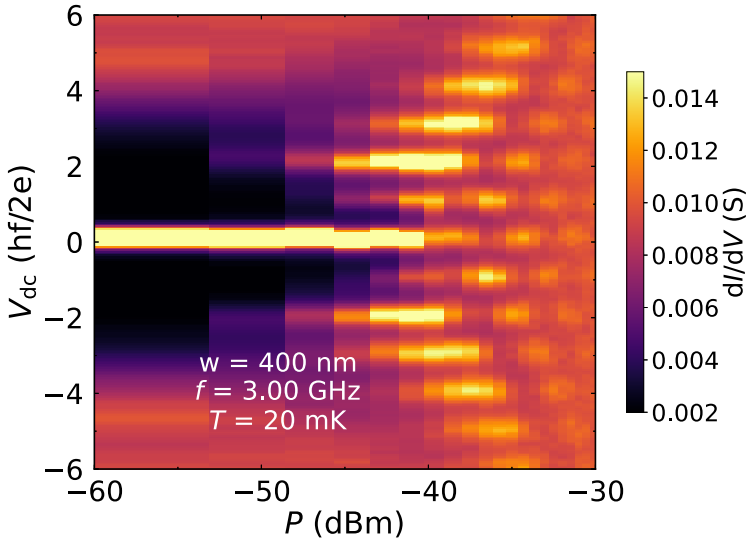

Figure 4.17: a, Color mapping of $\mathrm{d}I/\mathrm{d}V$ measured in Junction 1 on a TI ribbon with w = 400 nm under rf irradiation at frequency f = 3 GHz as a function of rf power P and applied dc voltage V_{dc} at B = 0 T and T = 20 mK.

Chapter 5

GIANT MAGNETOCHIRAL ANISOTROPY FROM QUANTUM-CONFINED SURFACE STATES OF TINW

5.1 Introduction

The widely-known Ohm's law $V = IR_0$ governs that for electric transport in most materials for small currents I the voltage drop across a material is proportional to a constant resistance R_0. Directional transport however is of great technological relevance as exemplified by semiconducting diodes that are omnipresent in wireless and computing technology. Diodes, or more general nonreciprocal transport channels that explicitly break the relevant symmetries, can produce a difference in resistance R as a current flows in one or the opposite direction so that $R(+I) \neq R(-I)$, an effect also termed rectification. Such nonreciprocal transport effects have been observed in an increasing number of quantum materials, typically with broken inversion symmetry and strong rashba spin-orbit coupling, where rectification is particularly well controllable [87–92, 230–234]. Magnetochiral anisotropy (MCA) is one of such effects and is described as a nonreciprocal charge transport in which the measured resistance R depends on an additional contribution that is linear in current I and externally applied magnetic field B, i.e. $R = R_0(1 + \gamma BI)$ [87–90]. Here the rectification coefficient γ determines the size of the possible rectification effect and is typically small (usually $|\gamma| \lesssim 1\ \mathrm{A}^{-1}\mathrm{T}^{-1}$[89–93]) as it relies on spin-orbit coupling, a relativistic effect [87–89].

For MCA to occur both inversion and time-reversal symmetry need to be broken [87–89] which can be achieved artificially in quasi-one-dimensional (1D) bulk-insulating 3D TI nanowires (TINW). Application of a gate voltage from the top of the TINW induces a non-uniformity of the charge density in the wire that breaks the subband degeneracy and results in a splitting of the subbands as well as a finite spin polarization that can lead to MCA when a magnetic field is applied [26, 33, 80, 83, 84]. This approach provides an unexplored playground to substantially enhance the size of non-reciprocal transport effects and makes TINWs an interesting platform to search for a resulting possibly very large MCA. Additionally upon tuning the chemical potential through the TINWs topological surface state subbands, γ is expected to change sign depending on the chemical potential μ. This makes the rectification effect due to the MCA highly controllable by both the magnetic field direction and μ which is experimentally easily adjusted by a small change in gate voltage V_g.
In the following work, after theoretical predictions that suggest the existence of this potentially giant rectification effect, expectations are confirmed by low-temperature transport experiments on thin bulk-insulating $(Bi_{1-x}Sb_x)_2Te_3$ (BST)

TINWs in which a MCA response fully consistent with theory and a $|\gamma| \sim 100000$ $A^{-1}T^{-1}$ is observed, an outstandingly large MCA rectification coefficient in a normal conductor [2]. This precise theoretical prediction and consecutive experimental validation does not only showcase good understanding and control over the underlying quantum effects present in TINWs, but could furthermore help to develop new perspectives for technological applications for devices made from TINWs, especially in the context of the recently rapidly growing field of superconducting diode effects [9, 139, 235–240]. Nonreciprocal responses in quantum materials touch on fundamental aspects of modern condensed matter physics such as broken symmetries, topology, quantum confinement and correlations, for which reason the discovered large and well-controlled MCA based on an intriguing combination of these aspects points to promising new grounds for research beyond the context of TINWs.

Reference: Rößler, M.*; Legg, H. F.*; Münning, F.; Fan, D.; Breunig, O.; Bliesener, A.; Lippertz, G.; Uday, A.; Taskin, A. A.; Loss, D.; Klinovaja, J.; Ando, Y. Giant magnetochiral anisotropy from quantum confined surface states of topological insulator nanowires. Nature Nanotechnology 2022, 17, 696-700.
* These authors contributed equally: Matthias Rößler, Henry F. Legg.

Author contributions: M.R. fabricated the devices, performed the experiments and analysed the data with help from H.F.L., F.M., D.F., O.B. and Y.A. H.F.L., with help from J.K., D.L. and Y.A., conceived the project. H.F.L., with help from J.K. and D.L., performed the theoretical calculations. A.B., G.L., A.U. and A.A.T. provided the material. H.F.L., M.R., D.L., J.K. and Y.A. wrote the manuscript with inputs from all the authors.

5.2 Results

5.2.1 Abstract

Wireless technology relies on the conversion of alternating electromagnetic fields to direct currents, a process known as rectification. While rectifiers are normally based on semiconductor diodes, quantum mechanical non-reciprocal transport effects that enable highly controllable rectification have recently been discovered [87–90, 230–234]. One such effect is magnetochiral anisotropy (MCA) [87–90], where the resistance of a material or a device depends on both the direction of current flow and an applied magnetic field. However, the size of rectification possible due to MCA is usually extremely small, because MCA relies on inversion symmetry breaking leading to the manifestation of spin-orbit coupling, which is a relativistic effect [87–89]. In typical materials the rectification coefficient γ due to MCA is usually [89–93] $|\gamma| \lesssim 1\ \mathrm{A}^{-1}\mathrm{T}^{-1}$ and the maximum values reported so far are $|\gamma| \sim 100\ \mathrm{A}^{-1}\mathrm{T}^{-1}$ in carbon nanotubes [241] and $ZrTe_5$ [94]. Here, to overcome this limitation, we artificially break inversion symmetry via an applied gate voltage in thin topological insulator (TI) nanowire heterostructures and theoretically predict that such a symmetry breaking can lead to a giant MCA effect. Our prediction is confirmed via experiments on thin bulk-insulating $(Bi_{1-x}Sb_x)_2Te_3$ TI nanowires, in which we observe an MCA consistent with theory and $|\gamma| \sim 100000\ \mathrm{A}^{-1}\mathrm{T}^{-1}$, a very large MCA rectification coefficient in a normal conductor.

5.2.2 Non-reciprocal transport due to broken symmetry

In most materials transport is well described by Ohm's law, $V = IR_0$, dictating that for small currents I the voltage drop across a material is proportional to a constant resistance R_0. Junctions that explicitly break inversion symmetry, for instance semiconductor pn-junctions, can produce a difference in resistance R as a current flows in one or the opposite direction through the junction, $R(+I) \neq R(-I)$; this difference in resistance is the key ingredient required to build a rectifier. A much greater degree of control over the rectification effect can be achieved when a similar non-reciprocity of resistance exists as a property of a material rather than a junction. However, to achieve such a non-reciprocity necessitates that the inversion symmetry of the material is itself broken. Previously, large non-reciprocal effects were observed in materials where inversion symmetry breaking resulted in strong spin-orbit coupling (SOC) [87–94]. However, since SOC is always a very small energy scale, this limits the possible size of any rectification effect.

The non-reciprocal transport effect considered here is magnetochiral anisotropy (MCA), which occurs when both inversion and time-reversal symmetry are broken [87–94]. When allowed, the leading order correction of Ohm's law due to MCA is a term second order in current and manifests itself as a resistance of the form $R = R_0(1 + \gamma BI)$, with B the magnitude of an external magnetic field and where γ determines the size of the possible rectification effect. MCA may also be called bilinear magnetoelectric resistance [90, 242]. We note non-reciprocal transport in ferromagnets [232, 233] does not allow the coefficient γ to be calculated and rectification of light into dc current due to bulk photovoltaic effects [243–245] concerns much higher energy scales than MCA.

5.2.3 Giant magnetochiral anisotropy (MCA) in TINW

In heterostructures of topological materials it is possible to artificially break the inversion symmetry of a material [84]; such an approach provides an unexplored playground to significantly enhance the size of non-reciprocal transport effects. In this context, quasi one-dimensional (1D) bulk-insulating three-dimensional TI nanowires [26, 33, 80, 83, 84] are the perfect platform to investigate large possible MCA due to artificial inversion symmetry breaking. In the absence of symmetry breaking, for an idealised cylindrical TI nanowire – although generalisable to an arbitrary cross-section [83, 84] – the surface states form energy subbands of momentum k along the nanowire and half-integer angular momentum $\ell = \pm\frac{1}{2}, \frac{3}{2}, \ldots$ around the nanowire, where the half-integer values are due to spin-momentum locking. The presence of inversion symmetry along a TI nanowire requires that the subbands with angular momenta $\pm\ell$ are degenerate. It is possible to artificially break the inversion symmetry along the wire, for instance, by application of a gate-voltage from the top of the TI nanowire [26, 33, 84]. Such a gate voltage induces a non-uniformity of charge density across the nanowire cross-section which breaks the subband degeneracy and results in a splitting of the subband at finite momenta [84] (see Fig. 5.1c). An additional consequence is that the subband states develop finite spin polarisation in the plane perpendicular to the nanowire axis (i.e. yz-plane) with the states with opposite momenta being polarized in the opposite directions such that the time-reversal symmetry is respected. When a magnetic field is applied, the subbands can be shifted in energy via the Zeeman effect, which suggests that an MCA can be present in this setup. Indeed, using the Boltzmann equation [91, 92, 94] (see Supplementary Note 4), we find an MCA of the vector product type $\gamma \propto \boldsymbol{P} \cdot (\hat{\boldsymbol{B}} \times \hat{\boldsymbol{I}})$ with the characteristic vector $\boldsymbol{P}$ in the yz plane. For the rectification effect $\gamma_\ell(\mu)$ of a given subband pair $\eta = \pm$

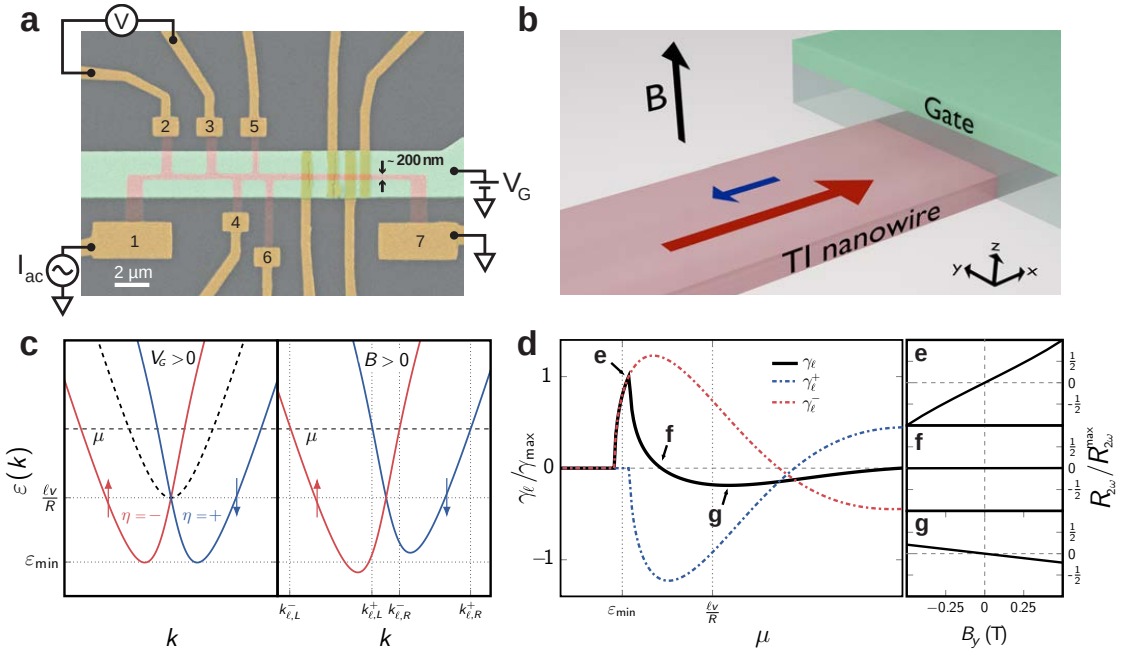

Figure 5.1: Gate-tunable topological insulator nanowire device and the theory of magnetochiral anisotropy: **a,** False-colour scanning-electron-microscope image of Device 1 with schematics of the electrical wiring; the Pt/Au leads are coloured in dark yellow, the TI nanowire etched from an MBE-grown BST thin film in red, and the top-gate electrode in green. The resistance of the nanowire was measured on different sections: Section 1, 2, 3, 4, 5 correspond to the voltage-contact pairs 2-3, 3-4, 4-5, 5-6, and 2-6, respectively. **b,** Schematic of MCA in TI nanowires. A gate, applied here to the top of the nanowire, breaks inversion symmetry along the wire. Applying a magnetic field along the gate normal (z-direction) results in a giant MCA rectification such that current flows more easily in one direction along the wire than the opposite (indicated by red/blue arrows). **c,** TI nanowire surface states form degenerate subbands (dashed line). When a finite gate voltage is applied, inversion symmetry is broken and the subbands split (solid lines). A new minimum occurs at $\varepsilon_{\min}$ and the states possess a finite spin polarisation in the yz-plane (red/blue colour). A magnetic field $\boldsymbol{B}$ shifts the subband pair relative to each other in energy due to the Zeeman effect, which is maximal for $\boldsymbol{B}$ along the z-axis, leading to an MCA (the size of the shift shown here is not to scale and used for clarity). **d,** Size of the MCA rectification γ_ℓ (see Eq. (5.1)) as a function of chemical potential μ within a given subband pair. Due to the peculiar dispersion of a TI nanowire, the curvature, $\hbar^2\mathcal{V}_\ell^\eta(k) \equiv \partial_k^2\varepsilon_\ell^\eta(k)$, is large and highly anisotropic at opposite Fermi momenta resulting in a giant MCA. As the chemical potential μ is tuned from the bottom of the subband, γ_ℓ changes sign. Here, for clarity, we used $B = 1$ T, see Supplementary Note 5 for further parameters. The panels **e-g** show the theoretically expected magnetic-field dependence of the 2nd harmonic resistance $R_{2\omega}$ at the chemical potentials indicated in the main panel. Reproduced with permission from Springer Nature [2].

labelled by $\ell > 0$, we found

$$\gamma_\ell = \gamma_\ell^+ + \gamma_\ell^- \approx \frac{e^3}{(\sigma^{(1)})^2 hB} \sum_{\eta=\pm} \tau^2 \left[\mathcal{V}_\ell^\eta(k_{\ell,R}^\eta) - \mathcal{V}_\ell^\eta(k_{\ell,L}^\eta) \right], \tag{5.1}$$

where e is the elementary charge, h is the Planck constant, $\sigma^{(1)}$ is the conductivity in linear response, τ is the scattering time, $\mathcal{V}_\ell^\eta(k) = \frac{1}{\hbar^2}\partial_k^2 \varepsilon_\ell^\eta(k)$ with $\varepsilon_\ell^\eta(k)$ describing the energy spectrum in the presence of symmetry breaking terms and of the finite magnetic field B (see Fig. 5.1c and Supplementary Note 4), and $k_{\ell,R(L)}^\eta$ is the right (left) Fermi momentum of a given subband (see Fig. 5.1c). Due to the non-parabolic spectrum of subbands, $\mathcal{V}_\eta^\pm(k)$ is large for a TI nanowire resulting in the giant MCA. The quantities γ_ℓ^+ and γ_ℓ^- are the contributions of the individual subbands. The behaviour of γ_ℓ as a function of chemical potential μ is shown in Fig. 5.1d. We find that, as the chemical potential is tuned through the subband pair, γ_ℓ will change sign depending on the chemical potential. This makes the rectification effect due to the MCA highly controllable by both magnetic field direction and by the chemical potential μ within a given subband pair, which can be experimentally adjusted by a small change in gate voltage. For reasonable experimental parameters we predict that the theoretical size of the rectification can easily reach giant values $\gamma \sim 5 \times 10^5\ \mathrm{T^{-1}A^{-1}}$ (see Supplementary Note 5).
To experimentally investigate the predicted non-reciprocal transport behaviour, we fabricated nanowire devices [7] of the bulk-insulating TI material $(Bi_{1-x}Sb_x)_2Te_3$ as shown in Fig. 5.1a by etching high-quality thin films grown by molecular beam epitaxy (MBE). The nanowires have a rectangular cross-section of height $h \approx 16$ nm and width $w \approx 200$ nm, with channel lengths up to several μm. The long channel lengths suppress coherent transport effects such as universal conductance fluctuations and the cross-sectional perimeter allows for the formation of well-defined subbands (see Supplementary Note 8). An electrostatic gate electrode is placed on top of the transport channel for the dual purpose of breaking inversion symmetry and tuning the chemical potential. The resistance R of the nanowire shows a broad maximum as a function of the gate voltage V_G (see Fig. 5.2a inset), which indicates that the chemical potential can be tuned across the charge neutrality point (CNP) of the surface-state Dirac cone; the dominant surface transport in these nanowires is further documented in the Supplementary Note 7. Near the broad maximum (i.e. around the CNP), the V_G dependence of R shows reproducible peaks and dips (see Fig. 5.2a), which is a manifestation of the quantum-confined quasi-1D subbands realized in TI nanowires [26] - each peak corresponds to the crossing of a subband minima, although the

feature can be smeared by disorder [26]. To measure the non-reciprocal transport, we used a low-frequency ac excitation current $I = I_0 \sin \omega t$ and probed the second-harmonic resistance $R_{2\omega}$. The MCA causes a second-harmonic signal that is antisymmetric with magnetic field $\boldsymbol{B}$, and therefore we calculated the antisymmetric component $R^A_{2\omega} \equiv \frac{R_{2\omega}(\boldsymbol{B}) - R_{2\omega}(-\boldsymbol{B})}{2}$, which is proportional to γ via $R^A_{2\omega} = \frac{1}{2}\gamma R_0 B I_0 \approx \frac{1}{2}\gamma R B I_0$, where R_0 is the reciprocal resistance (see Methods for details).

In our experiment, we observed a large $R^A_{2\omega}$ for $V_G \gtrsim 2$ V with a magnetic field along the z axis. The $R^A_{2\omega}(B_z)$ behaviour is linear for small B_z (see Fig. 5.2b) and $R^A_{2\omega}$ increases linearly with I_0 up to ∼250 nA (see Fig. 5.2c), both of which are the defining characteristics of the MCA. The deviation from B-linear behaviour at higher fields is likely due to orbital effects (see Supplementary Note 3). The magnetic-field-orientation dependence of γ, shown in Fig. 5.2d for the zx-plane rotation, agrees well with $\gamma \approx \gamma_0 \cos\alpha$, with α the angle from the z-direction and γ_0 the value at $\alpha = 0$; the yz-plane rotation gave similar results, while MCA remained essentially zero for the xy-plane rotation (see Supplementary Note 10). This points to the vector-product type MCA, $R^A_{2\omega} \propto \boldsymbol{P} \cdot (\boldsymbol{B} \times \boldsymbol{I})$, with the characteristic vector $\boldsymbol{P}$ essentially parallel to y, which is likely dictated by the large g-factor anisotropy [143] (see Supplementary Note 2). The maximum size of the $|\gamma|$ in Fig. 5.2d reaches a giant value of $|\gamma| \sim 6 \times 10^4$ $\mathrm{A^{-1}T^{-1}}$. In addition, one may notice in Figs. 2b and 2d that the relative sign of γ changes for different V_G values, which is very unusual. We observe a giant MCA with similarly large rectification γ in all measured devices, some of them reaching $\sim 1 \times 10^5$ $\mathrm{A^{-1}T^{-1}}$ (see Supplementary Note 13). Note that in the MCA literature, γ is often multiplied by the cross-sectional area A of the sample to give γ' (= γA), which is useful for comparing MCA in different materials as a bulk property. However, in nanodevices like our TI nanowires, the large MCA owes partly to mesoscopic effects and γ' is not very meaningful. In fact, the large MCA rectification of $|\gamma| \sim 100$ $\mathrm{A^{-1}T^{-1}}$ observed in chiral carbon nanotubes [241] was largely due to the fact that a nanotube can be considered a quasi 1D system. In the Supplementary Note 13, we present extensive comparisons of the nonreciprocal transport reported for various systems.

5.2.4 Controllability of MCA

A unique feature of the predicted MCA is the controllability of its sign with a small change of V_G. To confirm this prediction, we measured detailed V_G-dependence of $R^A_{2\omega}$ in the V_G range of 5.1–5.5 V, where the chemical potential appears to pass through two subband minima, because $R(V_G)$ presents two peaks

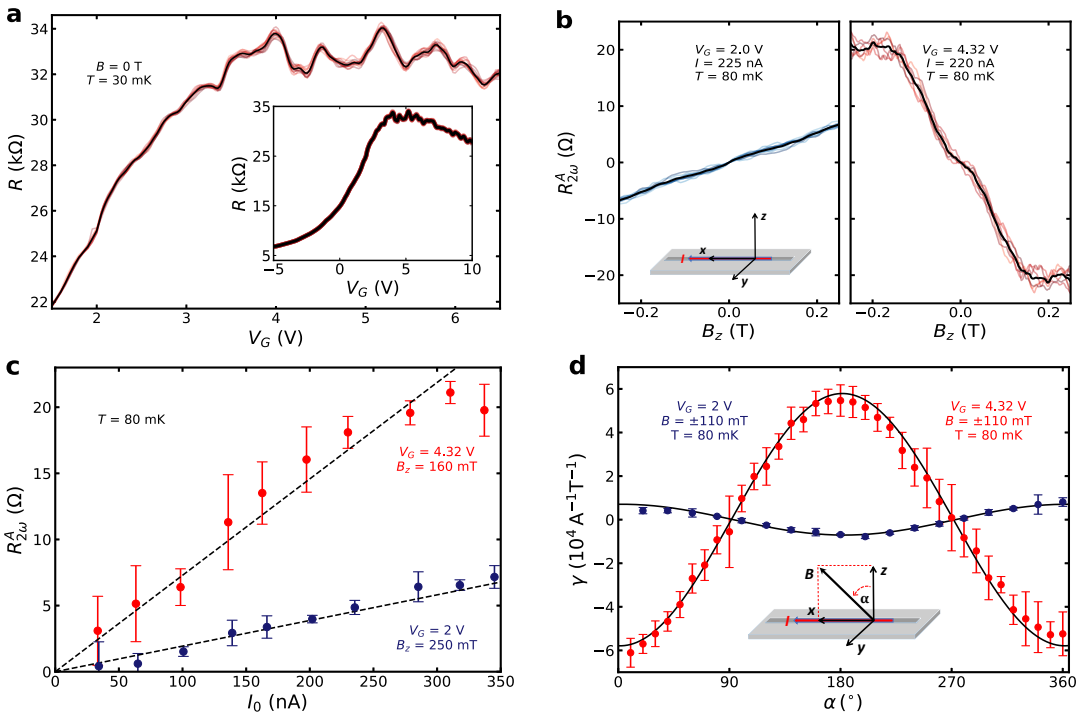

Figure 5.2: Non-reciprocal transport in $(Bi_{1-x}Sb_x)_2Te_3$ topological insulator nanowire: a, Four-terminal resistance R measured on Device 1, Section 1, at 30 mK in 0 T as a function of gate voltage V_G showing reproducible peaks and dips around the resistance maximum, which are consistent with the response expected from quantum-confined surface states [26]. Since the R value is very sensitive to the details of the charge distributions in/near the nanowires, the $R(V_G)$ behaviour is slightly different for different sweeps; thin red lines show the results of 15 uni-directional V_G sweeps and the thick black line shows their mean average. Inset shows the data for a wider range of V_G, demonstrating the typical behaviour of a bulk-insulating TI. **b,** Antisymmetric component of the second-harmonic resistance, $R^A_{2\omega}$, for V_G = 2 and 4.32 V plotted vs magnetic field $\boldsymbol{B}$ applied along the z-direction (coordinate system is depicted in the inset); coloured thin lines show 10 (6) individual B-field sweeps for 2 V (4.32 V) and the thick black line shows their mean. **c,** $R^A_{2\omega}$ measured for V_G = 2 and 4.32 V in the B-field (applied in the z-direction) of 0.25 and 0.16 T, respectively, as a function of the ac excitation current I_0. The dashed lines are a guide to the eye marking the linear behaviour. Error bars are defined using the standard deviation of 10 (6) individual B-field sweeps for 2 V (4.32 V). **d,** Magnetic-field-orientation dependencies of γ at V_G = 2 V (blue) and 4.32 V (red) when the B-field is rotated in the zx-plane. Error bars are defined using the Min-Max method with 6 (8) individual B-field sweeps for 2 V (4.32 V).. Solid black lines are fits to $\gamma \approx \gamma_0 \cos\alpha$ expected for MCA. The inset shows the definition of α and the coordinate system. Reproduced with permission from Springer Nature [2].

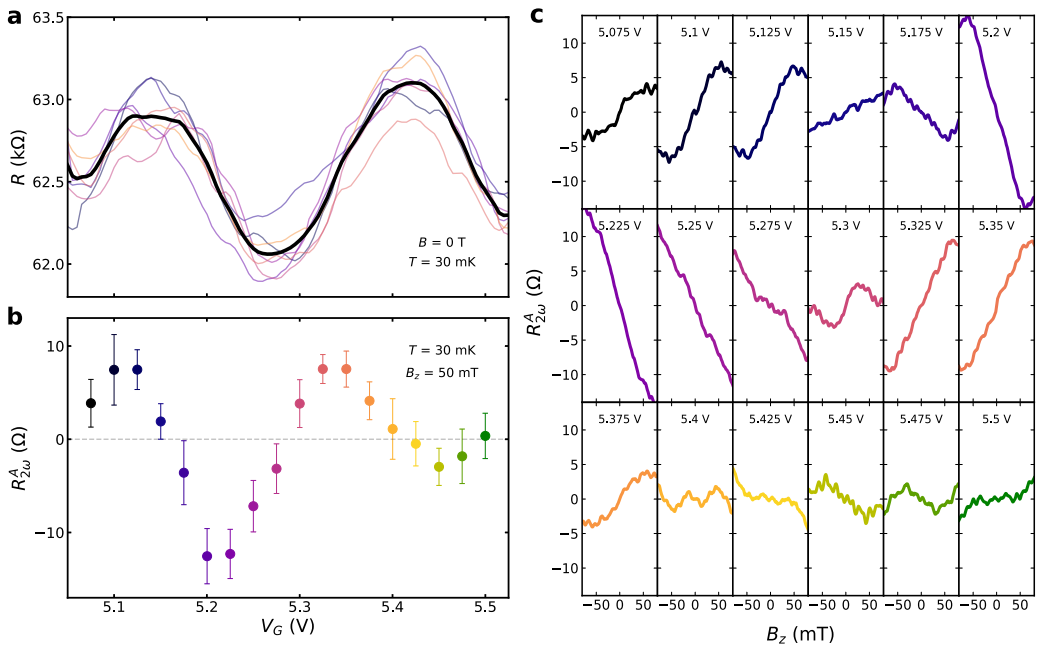

Figure 5.3: Evolution of the non-reciprocal response with changing chemical potential: a, R vs V_G data of Device 3, Section 5, in a narrow range of V_G, in which the chemical potential is changed near the CNP (for a wider range of V_G, see Supplementary Fig. 5.15a). The peaks in R occur when the bottom of one of the quantum-confined subbands is crossed by the chemical potential; coloured thin lines show 7 individual V_G sweeps and the thick black line shows their mean. **b,** Mean $R^A_{2\omega}$ values at B_z = 50 mT for various gate voltages in the range corresponding to panel **a**. The zero-crossings of $R^A_{2\omega}$ roughly correspond to the peaks and dips in $R(V_G)$, and thereby are linked to the quantum-confined subbands. Error bars are defined using the standard deviation of 10 individual B-field sweeps. **c,** Averaged $R^A_{2\omega}(B_z)$ curves at various V_G settings, from which the data points in panel **b** were calculated (data points and curves are coloured correspondingly). The systematic change in the $R^A_{2\omega}(B_z)$ behaviour as a function of gate voltage is clearly visible. Reproduced with permission from Springer Nature [2].

(see Fig. 5.3a). We indeed observe the slope of $R^A_{2\omega}(B_z)$ to change sign with V_G (see Fig. 5.3b), and its zero-crossing roughly coincides with the peak or dip in the $R(V_G)$ curve (compare Figs. 5.3a and 5.3b). A change in sign of the slope of $R^A_{2\omega}(B_z)$ on either side of $R(V_G)$ peaks is also observed in other devices (see Supplementary Note 11). To obtain confidence in this striking observation, the evolution of the $R^A_{2\omega}(B_z)$ behaviour upon changing V_G is shown in Fig. 5.3c for many V_G values. This sign change upon a small change of gate voltage also endows the giant MCA in TI nanowires with an unprecedented level of control. In addition, this V_G-dependent sign change of MCA gives a unique proof that the origin of the peak-and-dip feature in $R(V_G)$ is indeed subband-crossings.

5.2.5 Conclusion

The giant MCA observed here due to an artificial breaking of inversion symmetry in TI nanowires not only results in a maximum rectification coefficient γ that is orders of magnitude larger than any previously reported, but this giant MCA is also highly controllable by small changes of chemical potential. Although rather different to the MCA of a normal conductor discussed here, we note that large rectification effects of similar magnitude have recently been discovered in non-centrosymmetric superconductor devices [230, 234] and in quantum anomalous Hall edge states [233], where the controllability is comparatively limited. It is prudent to mention that the MCA reported here was measured below 0.1 K and it diminishes around 10 K (see Supplementary Note 12), which is consistent with the subband gap of $\sim$1 meV. Since TI nanowire devices are still in their infancy [7], the magnitude and temperature dependence of the MCA could be improved with future improvements in nanowire quality and geometry; for example, in a 20-nm diameter nanowire, the subband gap would be $\sim$10 meV which enables MCA up to $\sim$100 K. The presence of the giant MCA provides compelling evidence for a large spin-splitting of the subbands in TI nanowires with broken inversion symmetry which can be used for spin-filters [246, 247]. Moreover, it has been suggested that the helical spin polarization and large energy scales possible in such TI nanowires with broken inversion symmetry can be used as a platform for robust Majorana bound states [84], which are an integral building block for future topological quantum computers.

5.3 Supplementary Information

5.3.1 Further theoretical descriptions

Model Hamiltonian and symmetries

Since the nanowires considered in our experiments are etched from thin films of $(Bi_{1-x}Sb_x)_2Te_3$, the exact crystallographic direction of the nanowire is unknown and therefore in general the only remaining symmetries [143] of $(Bi_{1-x}Sb_x)_2Te_3$ are inversion symmetry ($\mathcal{I} : x \to -x, y \to -y, z \to -z$) and time-reversal symmetry (represented as $\Theta = i\sigma_y K$, where K is complex conjugation and σ_i are Pauli-matrices operating in spin space). To linear order a general Hamiltonian satisfying these symmetries – for analytic simplicity we will use a cylindrical nanowire – is given by

$$H(x,\theta) = \frac{v_F}{2r} - iv_F\left[\sigma_x\partial_\theta/R - \{\cos\varphi(\sigma_y\cos\theta - \sigma_z\sin\theta) + \sin\varphi(\sigma_y\sin\theta + \sigma_z\cos\theta)\}\,\partial_x\right], \tag{5.2}$$

where $\partial_\theta/R = \cos(\theta)\partial_y - \sin(\theta)\partial_z$, $2\pi r$ is the nanowire perimeter, v_F is the Fermi-velocity, and θ is the angle measured from the top of the nanowire. The angle φ parameterises the direction of the spin-texture perpendicular to the wire axis. In the [111] surface states of a bulk TI, an out-of-plane component ($\varphi \neq 0$) can occur, for instance, due to hexagonal warping effect [114]; in a nanowire, however, the exact amount of rotation is theoretically undetermined due to the low symmetry involving the side surface, and it will be determined by the experiment.
It can be see the Hamiltonian (5.2) has inversion symmetry since $H(x,\theta) = H(-x,\theta+\pi)$ and also obeys time-reversal symmetry because $H(x,\theta) = \sigma_y H^*(x,\theta)\sigma_y$. Note that both these symmetries map a current, I, along the wire such that $I \to -I$ and as such if either symmetry is present it requires that the resistance $R(I) = R(-I)$ and no MCA can occur. As will be discussed below a non-uniform potential $\delta\mu(\theta) \neq \delta\mu(\theta+\pi)$ through the cross-section breaks inversion symmetry and time reversal symmetry can be broken via the application of an external magnetic field.

Band structure and influence of gating

Applying the spinor rotation $U(\theta) = e^{i\theta\sigma_x/2}$ and using the ansatz wavefunction $\psi_{k\ell\tau}(y,\theta) = \chi_{k\ell\tau}e^{i(\ell\theta+ky)}$ gives

$$U^\dagger H U = v_F\sigma_x\ell/R - v_F k\left(\sigma_y\cos\varphi + \sigma_z\sin\varphi\right), \tag{5.3}$$

here k is the momentum along the nanowire and ℓ the angular momentum around the nanowire. Due to the 2π anti-periodicity of $U(\theta)$ the quantum confined surface states of a TI nanowire are such that the states have half-integer angular momentum $\ell = \pm\frac{1}{2}, \frac{3}{2}, \ldots$ around the nanowire and obey the dispersion relation

$$\epsilon_\ell(k) = \pm v_F \sqrt{k^2 + (\ell/r)^2}. \tag{5.4}$$

Application of a gate voltage, for instance, from the top of the TI nanowire, induces a non-uniform chemical potential $\mu(\phi) = \mu + \delta\mu(\phi)$ in the nanowire cross-section [26, 33, 84], where μ is the chemical potential on the nanowire surface (measured from the Dirac point) and $\phi = 0$ is the angle from the direction normal to the gate. The non-uniformity of chemical potential breaks inversion symmetry and can result in a large spin-splitting of the subbands for finite momentum k along the nanowire (see Fig. 5.1c main text). For an idealised circular nanowire and non-uniformities smaller than the subband gap – although also valid for larger non-uniformities – it has been shown that the dispersion is given by (see Ref. [84] for details)

$$\varepsilon_\ell^\pm(k) \approx \epsilon_\ell(k) \pm \frac{k\mu_{2\ell}}{\sqrt{k^2 + (\ell/r)^2}}, \tag{5.5}$$

and similarly $-\varepsilon_\ell^\pm(k)$ below the Dirac point. Here the bands are labelled by $\ell > 0$ and μ_n is the nth Fourier coefficient of the non-uniform chemical potential $\delta\mu(\phi) = \sum_n \mu_n \cos n\phi$ assuming the potential is symmetric for $\pm\phi$. The magnitude of the splitting does not depend strongly on the exact shape of the potential, $\delta\mu(\phi)$, other than through the components μ_n [84]. The band splitting due to such a non-uniform potential is shown in Fig. 5.1c in the main text.

When inversion symmetry in the Hamiltonian (5.3) is broken by a non-uniform chemical potential the states in the split-bands possess a finite spin polarisation $\boldsymbol{s} = (0, s_y, s_z)$ in the yz-plane that is perpendicular to the wire axis [84]. As a result, as discussed in the main text, when a magnetic field is applied in the yz-plane the bands shift relative to each other by the Zeeman energy $\pm(g_y\mu_B s_y B_y + g_z\mu_B s_z B_z)/2$ with $g_{y(z)}$ the g-factor in the $y(z)$-direction and μ_B is the Bohr magneton. Given that in $(Bi_{1-x}Sb_x)_2Te_3$ the g-factor is highly anisotropic, $g_z/g_y \simeq 20$ [143, 248], we neglect the contribution $g_y\mu_B s_y B_y$ which would be only significant for very large s_y/s_z. As such, the situation can be modelled analytically by considering helical bands – valid in the limit of small non-uniformities – such that the subbands $\varepsilon_\ell^\pm(k)$ above the Dirac point are given by

$$\varepsilon_\ell^\pm(k) \approx \epsilon_\ell(k) \pm \frac{k\mu_{2\ell}}{\sqrt{k^2 + (\ell/r)^2}} \pm g_z\mu_B s_z B_z/2 \tag{5.6}$$

and similarly $-\varepsilon_\ell^{\pm}(k)$ below the Dirac point (see Fig. 5.1c main text).

Influence of orbital effects

We can estimate the field strength at which orbital effects due to the out-of-plane field affect the MCA by considering the probability density of a state in a Landau level without any confinement. Such a state is localised with the form $|\psi|^2 \propto e^{-r^2/2l_B^2}$, where r the displacement on the surface and $l_B = \sqrt{\hbar/eB}$ the magnetic length. As such a Landau level state will only be consistent with the confinement of our $W \approx 200$ nm wide nanowire when $(W/2)/2l_B \sim 1$, this corresponds to a field strength of $B \sim 0.15$ T. Indeed, experimentally we find that at this field strength the MCA begins to saturate (see e.g. Fig. 5.2b main text).
Orbital effects due to a magnetic field B_x along the wire should also open a gap in the dispersion [84]. However, for the small $B = 110$ mT field used in the experimental angular rotation α the size of such a gap will be very small – since this field strength is considerably less than a flux quantum corresponding to a field value $B \sim 1.4$ T for the given nanowire cross-section – as such orbitals effects will only alter the MCA from the perpendicular component for a very small range of chemical potentials and only for $\alpha \sim 90^{\text{o}}$ or $\alpha \sim 270^{\text{o}}$ in Fig. 5.2d of the experiment. Finally we note that for a magnetic field, B_x, parallel to the wire axis, the Zeeman contribution can be entirely absorbed into the orbital contribution [84], such that $\frac{\Phi}{\Phi_0} \to \frac{\Phi}{\Phi_0} - \frac{\frac{1}{2}g_x\mu_B B_x}{\hbar v_F/r}$, where $\Phi = BA$ with A the cross-sectional area of the wire, the fundamental flux quantum $\Phi_0 = h/e$, and $\frac{1}{2}g_x\mu_B B_x$ is the Zeeman energy due to the magnetic field parallel to the wire.

Linear and second order response conductivity from the Boltzmann equation

Since the gate and magnetic field break inversion and time-reversal symmetry, respectively, an MCA is symmetry allowed for the setup shown in Fig. 5.1b. In this section, we use the Boltzmann equation in the relaxation time approximation to derive the conductivity expanded to linear and second order in electric field, i.e. the linear and second order conductivity [92, 94]. This approach is valid in the diffusive limit, relevant for the bulk-insulating TI nanowires in our experiment [26]. We start by considering a scattering time which is independent of the chemical potential $\tau(\mu) = \tau$. Later in this section we will consider the influence of broadening processes such as Coulomb disorder and the inclusion of the dependence of scattering time on chemical potential.

Boltzmann equation for 1st order conductivity: We begin by expanding the distribution function of states in a given subband labelled by $(\ell, \pm)$ as $f^{\pm,\ell} = f_0^{\pm,\ell} + f_1^{\pm,\ell} + f_2^{\pm,\ell} + ...$, where $f_n^{\pm,\ell}$ is the nth order response to an electric field E of the $\pm$ branch of ℓth subband [92]. The distribution function to first order in E within the relaxation time approximation of the Boltzmann equation is therefore given by

$$f_1^{\pm,\ell} \approx \frac{e\tau E}{\hbar}\frac{\partial f_0^{\pm,\ell}}{\partial k} = e\tau E v_\ell^{\pm}(k)\frac{\partial f_0^{\pm,\ell}}{\partial \varepsilon_\ell^{\pm}(k)}, \tag{5.7}$$

where $v_\ell^{\pm}(k) = \frac{1}{\hbar}\partial_k \varepsilon_\ell^{\pm}(k)$ is the velocity and e the elementary charge. We use the Fermi-Dirac distribution function for $f_0^{\pm,\ell} = f_0(\varepsilon_\ell^{\pm}(k) - \mu)$.
Next, we calculate the current density $j = j^{(1)} + j^{(2)} + \dots$ expanded order by order in electric field. We begin by utilising the first order distribution function to calculate the current density $j^{(1)}$ which is first order in electric field E (with coefficient given by the linear response conductivity $\sigma^{(1)}$) such that

$$\begin{aligned} j^{(1)} \equiv E\sigma^{(1)} &= -e\sum_{\eta=\pm}\sum_{\ell=\frac{1}{2},\frac{3}{2},\dots}\int \frac{dk}{2\pi} v_\ell^{\eta}(k) f_1^{\eta,\ell} \\ &= e^2 E \sum_{\eta=\pm}\sum_{\ell=\frac{1}{2},\frac{3}{2},\dots} \tau \int \frac{dk}{2\pi}[v_\ell^{\eta}(k)]^2 \delta(\mu - \varepsilon_\ell^{\eta}(k)) \\ &= \frac{e^2}{h} E \sum_{\eta=\pm}\sum_{\ell=\frac{1}{2},\frac{3}{2},\dots} \tau \left[v_\ell^{\eta}(k_{\ell,R}^{\eta}) - v_\ell^{\eta}(k_{\ell,L}^{\eta})\right], \end{aligned} \tag{5.8}$$

where in the second line we used that the Fermi-Dirac distribution at zero temperature is given by $\frac{\partial f_0^{\pm,\ell}}{\partial \varepsilon_\ell^{\pm}(k)} = -\delta(\mu - \varepsilon_\ell^{\pm}(k))$ and, as in the main text, $k_{\ell,R}^{\eta}$ and $k_{\ell,L}^{\eta}$ are right and left Fermi wave vectors for the $\eta = \pm$ branch of ℓth subband (see Fig. 5.1c main text). In general, these wave vectors $k_{\ell,L/R}^{\eta}$ can be found by numerically solving the equation $\varepsilon_\ell^{\eta}(k_{\ell,L/R}^{\eta}) = \mu$. Note that if the band is not occupied then it will not contribute to the current density j. Finally, we also note that setting magnetic field to zero ($B = 0$) and non-uniform chemical potential to zero ($\delta\mu(\phi) = 0$) we find that $\sigma^{(1)}(\mu)$ coincides with the result with the same limit in Ref. [26] derived from the Kubo formula.

Boltzmann equation for 2nd order conductivity: The E^2 contribution to the current density $j^{(2)}$ can be obtained similarly by using the first order of the distribution function $f_1^{\pm,\ell}$ from above such that in the relaxation time approximation [92] we arrive at

$$f_2^{\pm,\ell} \approx \frac{e\tau E}{\hbar}\frac{\partial f_1^{\pm,\ell}}{\partial k} = \left(\frac{e\tau E}{\hbar}\right)^2 \frac{\partial^2 f_0^{\pm,\ell}}{\partial k^2}. \tag{5.9}$$

Inserting this expression for $f_2^{\pm,\ell}$ into the Boltzmann equation gives the component of current density proportional to the square of the electric field as

$$j^{(2)} \equiv \sigma^{(2)} E^2 = -e \sum_{\eta=\pm} \sum_{\ell=\frac{1}{2},\frac{3}{2},\ldots} \int \frac{dk}{2\pi} v_\ell^\eta(k) f_2^{\eta,\ell} \tag{5.10}$$

$$= -e \left(\frac{e\tau E}{\hbar}\right)^2 \sum_{\eta=\pm} \sum_{\ell=\frac{1}{2},\frac{3}{2},\ldots} \int \frac{dk}{2\pi} v_\ell^\eta(k) \frac{\partial^2 f_0^{\pm,\ell}}{\partial k^2} \tag{5.11}$$

$$= -e \left(\frac{e\tau E}{\hbar}\right)^2 \sum_{\eta=\pm} \sum_{\ell=\frac{1}{2},\frac{3}{2},\ldots} \int \frac{dk}{2\pi} v_\ell^\eta(k) \frac{\partial^2 \varepsilon_k^\eta}{\partial k^2} \delta(\mu - \varepsilon_k^\eta)$$

$$= -\frac{e^3}{h} E^2 \sum_{\eta=\pm} \sum_{\ell=\frac{1}{2},\frac{3}{2},\ldots} \tau^2 \left[\mathcal{V}_\ell^\eta(k_{\ell,R}^\eta) - \mathcal{V}_\ell^\eta(k_{\ell,L}^\eta)\right],$$

where $\mathcal{V}_\ell^\pm(k) = \frac{1}{\hbar^2}\partial_k^2 \varepsilon_\ell^\pm(k)$ denotes the band curvature and the second line requires integration by parts. We use this to aquire the MCA rectification coefficient

$$\gamma = \frac{-\sigma^{(2)}}{B(\sigma^{(1)})^2} = \sum_{\ell=\frac{1}{2},\frac{3}{2},\ldots} \gamma_\ell, \tag{5.12}$$

with γ_ℓ given by Eq. (1) of the main text. We note that for a purely parabolic band, for example, in a Rashba nanowire where to good approximation $\varepsilon_\pm(k) = (k \pm k_{\mathrm{so}})^2/2m$, the quantity $\mathcal{V}_\ell^\pm(k) = 1/m$ is independent of the Fermi wavevectors $k_{L/R}^\pm$ if the magnetic field points along the spin-orbit interaction vector and, thus, the two contributions $\gamma_\ell^\pm$ of Eq. (1) in the main text would cancel each other. Hence, the giant size of the MCA is a unique feature of the peculiar dispersion of TI subbands and the fact the spin degree of freedom enters Dirac Hamiltonian of the TI surface states. In what follows we focus on the contribution of an individual subband pair via γ_ℓ. We note that the precise magnitude of the harmonics μ_n depends on several experimental factors which are difficult to model theoretically, these include the electrostatics of the nanowire setup, screening effects (e.g. from contacts), and the exact geometry of the nanowires. Using (5.11) and the eigenenergies from (5.6) gives the result shown in Fig. 5.1d of the main text. Finally, we note that $\sigma^{(2)}$ is zero when the chemical potential is uniform in the cross-section (i.e. $\mu_n = 0$ for all n) or when the magnetic filed is absent (i.e. $g\mu_B B_y/2 = 0$). In other words there is only a finite MCA when *both* inversion symmetry and time reversal symmetry are broken simultaneously, as expected.

Estimate of rectification effect:

To obtain a theoretical estimate of the size of the maximum possible MCA rectification γ in a typical nanowire, we first use the experimental fact that the Ohmic resistance of a $L \sim 5$ μm nanowire (e.g. the resistance of Device 3, Section 5, see Fig. 5.15) saturates at $R \sim 60$ kΩ as function of gate voltage with only small fluctuations around this value, these oscillation can be attributed to the quantum confinement of surface states (see below). For the $W \approx 200$ nm and $H \approx 16$ nm nanowires used in our experiment the presence of these fluctuations suggests that the broadening due to disorder is smaller than the subband spacing, i.e. $\tau \gtrsim \hbar/(1\ \mathrm{meV}) \sim 1$ ps, in fact this value also fits well with the $\sigma^{(1)} \sim 0.1\ \mu\mathrm{m/k}\Omega$ found experimentally. Numerically calculating $\sigma^{(2)}(\mu)$ using (5.11) we find that the maximum $|\sigma^{(2)}| \sim e^3(\tau/\hbar)^2(2500\ \mathrm{meV\ nm^2})/h$ close to the bottom of the subband pair, here we use the small angular momenta $\ell = 3/2$, Fourier coefficient $\mu_{2\ell} \sim \ell v/r$, $v \sim 5 \times 10^5$ m/s, and $B \sim 0.05$ T with the g-factor $g_z \approx 50$ [143] and take a conservative estimate for spin component in the z-direction $s_z = 0.08$. Therefore, we estimate the order of magnitude for the maximal rectification γ_ℓ from a given subband pair as

$$|\gamma_\ell^{\max}| = \frac{|\sigma^{(2)}|}{B(\sigma^{(1)})^2} \sim \frac{e^3(1\ \mathrm{ps}/\hbar)^2(2500\ \mathrm{meV\ nm^2})}{h(0.05\ \mathrm{T})(0.1\ \mu\mathrm{m/k}\Omega)^2} \sim 5 \times 10^5\ \mathrm{A^{-1}T^{-1}}. \tag{5.13}$$

This estimate represents only an approximation of the order of magnitude that one can expect due to MCA in TI nanowires, showing that it is extremely large. In real experimental systems the value of $|\gamma_\ell^{\max}|$ could even be larger if the non-uniformity of chemical potential across the nanowire cross-section, characterised by the Fourier harmonics μ_n, is larger than assumed here. It is, however, as found in experiment, more likely that $|\gamma_\ell^{\max}|$ is reduced in size by several factors such as the chemical potential dependence of scattering time, smearing of chemical potential due to Coulomb disorder, and further effects not considered in this simple approximation, for instance the separate contributions of bulk and surface conductivity channels. Note that throughout the calculations above, there is an assumption that $|E\sigma^{(2)}| \ll |\sigma^{(1)}|$ is always satisfied; when this assumption is not satisfied, our second-order theory breaks down. Although the rectification is giant in comparison to the largest γ values observed so far, the estimate given in Eq. (5.13) is still orders of magnitude below this bound for all values of B and I in our experiment.

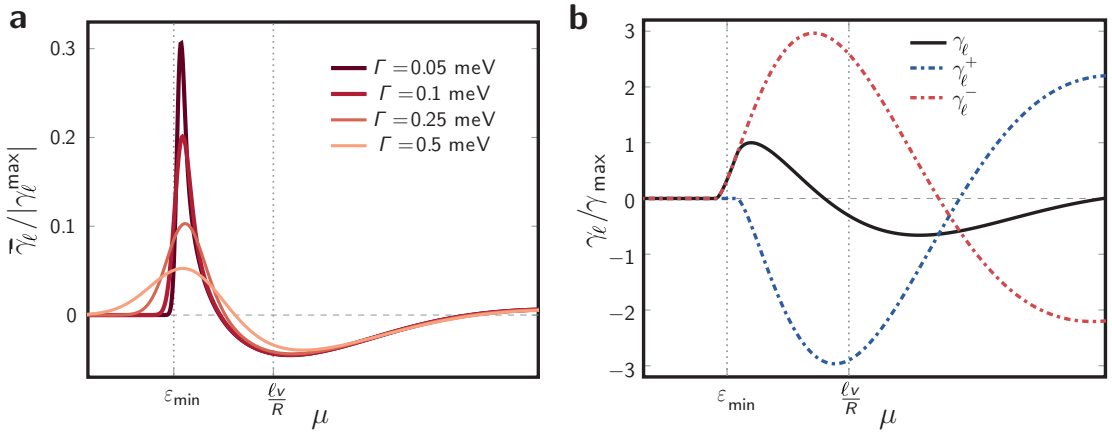

Figure 5.4: Influence of different disorder effects: a, Influence of Coulomb disorder: Charged impurities in the bulk and on the surface of the TI smear out the chemical potential μ which leads to a reduction and smoothing of γ_ℓ, here shown for a constant scattering time τ. We choose realistic experimental parameters $B = 0.05$ T, $g = 4$, $v_F = 5 \times 10^5$ m/s, $\tau \sim 1$ ps. For this plot we also chose $\ell = 3/2$ with the Fourier harmonic $\mu_{2\ell} \approx v_F \ell / r \approx 3.9$ meV. This gives $|\gamma_\ell^{\max}| \sim 5 \times 10^5$ T^{-1}A^{-1} as discussed in the text. These are the same parameters as in Fig. 5.1d of the main text, apart from there $B = 1$ T is used for clarity of the different contributions. **b,** Influence of strong subband minimum scattering: Although only weakly visible in our experimental devices, close to a given subband minimum there is an increase in the scattering rate $1/\tau$ due to the diverging density of states [26]. Here, we show that, even in nanowires in which τ is very strongly dependent on chemical potential μ (such that $\tau = 0$ at the bottom of the band), the overall qualitative features of γ_ℓ will be largely unaffected by such a divergence, with a pronounced maximum and change in sign still clearly visible. We use the same parameters as in **a**, apart from $B = 1$ T for clarity of the different contributions. For simplicity in this plot we assume $\sigma^{(1)} \approx \text{const.}$ since there are more conductivity channels for Ohmic conductivity, i.e. through the bulk. In reality $\sigma^{(1)}$ will also inherit the additional dependence on τ which will lead to an increase in γ_ℓ close to $\varepsilon_{\min}$.

Influence of disorder

Influence of Coulomb disorder: One reasons for the lower experimental value than the estimate of (5.13) is the influence of Coulomb disorder in the bulk and on the surface of the TI nanowire [160, 162, 164, 165]. In general, such Coulomb disorder leads to fluctuations in the local chemical potential of the nanowire surface, resulting in so-called surface puddles. These surface puddles smear out the chemical potential and lead to an averaging of γ_ℓ over the length of the nanowire [160]. To approximate the influence of such surface puddles we use our result from (5.11) and assume that the surface fluctuations of chemical potential belong to a Gaussian distribution of width Γ, such that

$$\bar{\gamma}_\ell(\mu) = \frac{1}{\Gamma\sqrt{2\pi}} \int_{-\infty}^{\infty} d\mu' \gamma_\ell(\mu') e^{-\frac{1}{2}\left(\frac{\mu-\mu'}{\Gamma}\right)^2}. \tag{5.14}$$

We show $\bar{\gamma}_\ell(\mu)$ for several distributions widths Γ in Fig. 5.4. As expected, for not unrealistic broadenings Γ, the smearing results in a smoothening of the function $\gamma_\ell(\mu)$ and a reduction in the maximum possible rectification $|\bar{\gamma}_\ell^{\max}|$. The density of Coulomb disorder and its influence on the surface states of TI nanowires remains an open experimental question, but the presence of quantum confinement oscillations in the resistivity curves suggests that the broadening Γ of our ribbon-shaped experimental nanowires is smaller than or similar to the subband spacing.

Influence of scattering time: In the experiment, quantum confinement features in the Ohmic resistance R due to increased scattering near the bottom of subbands are weak ($\sim 5\%$ of the total R, see Fig. 5.3a), and so, to a good approximation, τ can be taken as constant (as above). In theory, for a nanowire with perfect quantum confinement and only surface contributions to the conductivity, the scattering time τ becomes very strongly dependent on the position of the chemical potential within a given subband due to the divergence in density of states at subband minima in one dimension [26]. For completeness, here we take the opposite limit and assume the scattering time is strongly dependent on chemical potential and consider how this would affect $\sigma^{(2)}(\mu)$ and hence $\gamma_\ell(\mu)$. We will see that the overall qualitative features of $\gamma_\ell(\mu)$ are largely unchanged in this limit.

To estimate the scattering time we will use the Born approximation [26] valid for weak impurity scattering potential u_0 and low impurity density n_{imp} and assume that spin-flip interband scattering is negligible. The scattering time for

the separate $\pm$ bands at zero temperature is given by

$$\frac{\hbar}{\tau^{\pm}(\mu)} \approx n_{\mathrm{imp}} u_0^2 \sum_{\ell=\frac{1}{2},\frac{3}{2},\ldots} \int \frac{dk}{2\pi} \delta(\mu - \varepsilon_\ell^{\pm}(k)) = n_{\mathrm{imp}} u_0^2 \sum_{\ell=\frac{1}{2},\frac{3}{2},\ldots} \rho_\ell^{\pm}(\mu), \tag{5.15}$$

where

$$\rho^{\pm}(\mu) = \sum_{\ell=\frac{1}{2},\frac{3}{2},\ldots} \left(\frac{1}{\hbar |v_\ell^{\pm}(k_{\ell,L}^{\pm})|} + \frac{1}{\hbar |v_\ell^{\pm}(k_{\ell,R}^{\pm})|} \right) \tag{5.16}$$

is the density of states of the respective $\pm$ bands. The linear response and second harmonic conductivities are obtained with the replacement $\tau \to \tau^{\pm}(\mu)$. The density of states in (5.16) diverges at the bottom of a given subband leading to a rapid increase in the scattering rate at this point [26], however, the qualitative features of $\sigma^{(2)}(\mu)$ and hence γ_ℓ within a given subband are not strongly modified by this additional dependence of $\tau(\mu)$ (see Fig. 5.4b). Additionally, the divergence of scattering rate will be cut-off by temperature and disorder, we can therefore expect that the true experimental behaviour of γ_ℓ is somewhere between the two scenarios shown in Fig. 5.4b and Fig. 5.1d of the main text.

5.3.2 Further experimental descriptions

Materials characterization

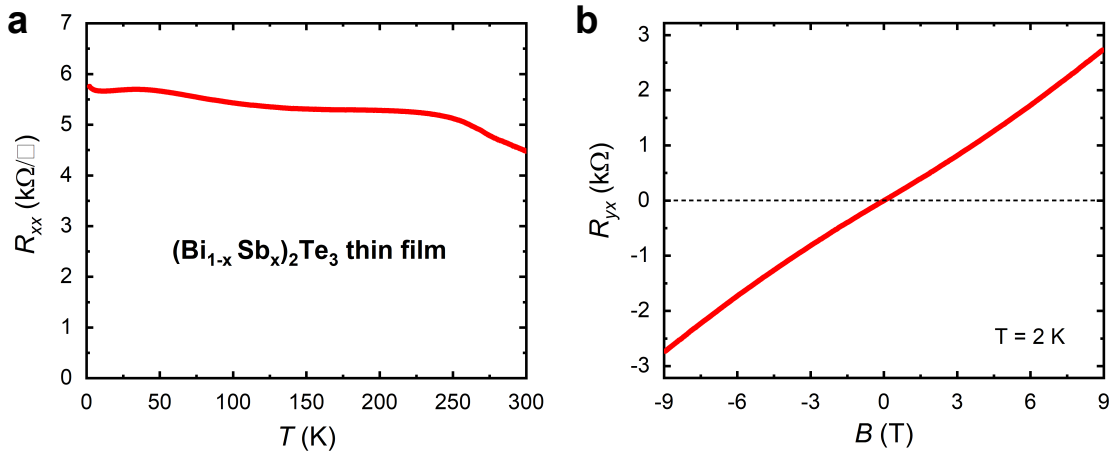

Figure 5.5: Transport properties of the $(Bi_{1-x}Sb_x)_2Te_3$ thin film used for the nanowire device fabrication. a, Temperature dependence of the sheet resistance R_{xx} of the thin film used in this study. A six-terminal measurement was done on a small part of the 2×2 cm^2 film. **b,** Magnetic-field dependence of the Hall resistance R_{yx} at 2 K.

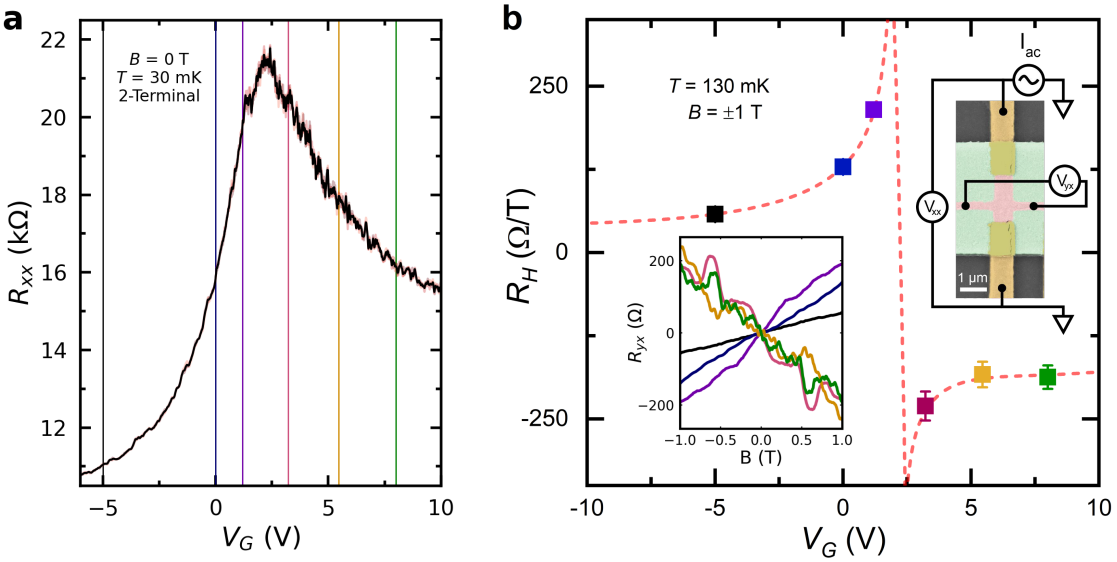

Figure 5.6: V_G-dependence of R_{xx} and R_H in Device 4. a, $R_{xx}(V_G)$ data measured with a two-terminal configuration shown in the inset of panel **b**. Thin red lines show 3 uni-directional V_G sweeps, while the thick black line shows the average. Coloured vertical lines shows the V_G positions where R_H in panel **b** was measured. **b,** R_H at selected V_G values extracted from a linear fit of the $R_{yx}(B)$ data for $B = \pm 1$ T applied along the $\hat{z}$-axis, which are shown in the left inset. The red dashed line is a guide to the eye. The right inset shows the reconfigured electrode arrangement of Device 4 for these measurements, in which the nanowire part is used as Hall-voltage electrodes.

Figure 5.5 shows the the temperature dependence of the sheet resistance R_{xx} and the magnetic-field dependence of the Hall resistance R_{yx} measured on a small piece taken from the $(Bi_{1-x}Sb_x)_2Te_3$ (BST) thin film that was used for fabricating all the nanowire devices. The $R_{xx}(T)$ behavior, presenting only a weak T-dependence, is typical for a bulk-insulating BST thin film [217, 249], which is corroborated by the low 2D hole carrier density of only $n \sim 1.8\times10^{12}$ cm^{-2} calculated from dR_{yx}/dB at B = 0 T. We also obtain the mobility $\mu \simeq 600$ cm^2/Vs from the data in Fig. 5.5.

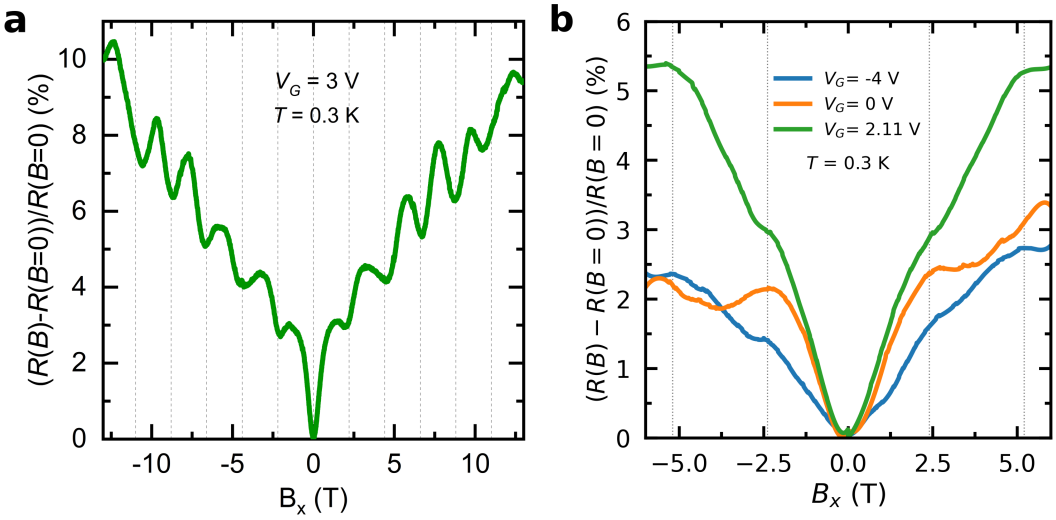

Figure 5.7: Aharonov-Bohm-like oscillations in top-down-fabricated TI nanaowires. a, Magnetic-field dependence of the resistance, $R(B)$, measured in Device 5, Section 2, with magnetic fields applied along the nanowire axis, normalized by the resistance value at B = 0 T. Vertical dashed lines mark the periodicity. **b,** Similar oscillations were observed at various V_G values in Device 4, Section 2, although the maximum magnetic field was limited to 6 T in the measurement of this device. Vertical dashed lines mark the peak positions.

To further document the dominant role of the surface states in the transport properties, Fig. 5.6 shows the gate-voltage (V_G) dependence of the resistance R_{xx} and the Hall coefficient R_H of Device 4. For these measurements, we reconfigured Device 4, which is on the same wafer as Devices 1–3, to use the nanowire section as the Hall-voltage electrodes (see inset of Fig. 5.6b), because the Hall voltage cannot be measured on a nanowire; the $R(V_G)$ data were simultaneously measured with a two-terminal configuration on the section where R_H was measured. The V_G-dependence of R_H in Fig. 5.6b presents the typical semi-divergence and sudden sign change as the Fermi level is tuned across the Dirac point with gating; this behavior gives evidence that the Dirac cone of the surface states dominates the transport. In addition, the corresponding V_G-dependence of the resistance R

in Fig. 5.6a presents a sharp peak at the Dirac point, which is another signature of the dominant surface transport.
The magnetoresistance (MR) data with magnetic fields applied along the nanowire axis provide additional support to the dominant role of the surface states when they present Aharonov-Bohm (AB)-like oscillations (see Ref. [81] for details) which reflect the periodic change in the quantum-confined surface states as a function of the threading magnetic flux [80]. The MR data shown in Fig. 5.7a were measured on Device 5, which was fabricated in the same way and from a thin film of very similar quality as that of Devices 1–4. The nanowire part of Device 5 was ∼17-nm thick and ∼200-nm wide. The observed oscillation period of ∼2.2 T corresponds to the flux quantum Φ_0 (= h/e) if the relevant area is 1.9 $\times$ 10^{-15} m^2, which is essentially consistent with the cross-sectional area of the nanowire when considering the finite extension of the surface-state wavefunction. This consistency gives confidence in the interpretation that the MR data in Fig. 5.7a signifies the AB-like oscillations from the quantum-confined surface states. The TI nanowire of Divice 4 used for the MCA experiment presents similar AB-like oscillations at various V_G values as shown in Fig. 5.7b, although the magnetic-field range was limited to ±6 T in the measurement of this device. Here again, the oscillation period of ∼2.6 T (indicating the relevant area of 1.6 $\times$ 10^{-15} m^2) is essentially consistent with the cross-sectional area of the nanowire (∼ 16 $\times$ 200 nm^2) considering the depth of the surface states.

Signatures of well-defined surface state subbands

The regular gate dependent resistance oscillations and AB-like resistance oscillations in magnetic field that we observe are both signatures of well-defined subbands [25, 26, 28, 33, 80]. Both types of oscillation are of similar magnitude, this is expected since they arise as the result of the increased density of states that occurs close to the bottom of subbands [26]. In this section we will show that both gate dependent resistance oscillations and AB-like oscillation depend on the nanowire cross-sectional geometry and that the estimate of this geometry is consistent with the geometry of our nanowires for both types of oscillation. We also note that the TI nanowire devices used in our study have long channel lengths up to several μm, we can therefore confidentially rule out the presence of universal conductance fluctuations (UCFs) in our TI nanowire devices since the channel lengths are longer than the phase coherence length and, in addition, we do not observe the magnetic field dependent resistance jumps expected to arise due to UCFs (see Fig. 5.7). Finally, the observation of the smooth change of sign

of the MCA signal within single gate voltage peaks actually provides yet another check for well defined subbands in our nanowires.

The nanowires in our study have widths of $W \approx 200 \pm 20$ nm and heights $H \approx 16 \pm 1$ nm, this leads to variations between different devices of $\pm 15\%$ in cross-sectional area $A = W \times H$ and variations $\pm 10\%$ in the perimeter $P = 2(W + H)$. As discussed above, the observed AB period, P_{AB}, was ~2.6 T for Device 4 (16 nm thickness measured via AFM) and ~2.2 T in Device 5 (17 nm measured via AFM). The periods of AB-like resistance oscillations are dependent on the flux enclosed by the quantum confined surface state and as such vary with the cross-sectional area, A, of the device. Therefore, taking into account the ~ 4 nm average extension of the TI surface states [166], the periods of AB-like oscillations allow us to estimate a width $W \approx 190$ nm for Device 4 and $W \approx 220$ nm for Device 5. These values fall within the expected range of the nanowire widths.

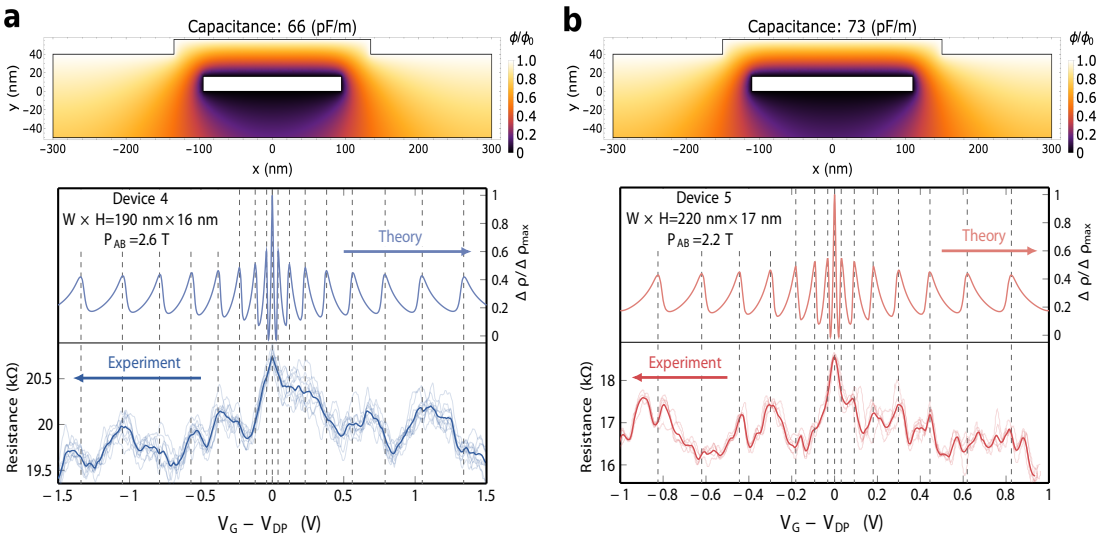

Figure 5.8: Gate voltage dependent resistance oscillations close to the resistance maximum: a) Device 4 and b) Device 5. Top: Electrostatic potential resulting from numerical solution of the Laplace equation using an electrostatic model of our full device setup and the device cross-section estimated from AB-like oscillations. Bottom: Gate voltage dependent resistance averaged over several gate voltage sweeps (lighter thin lines show individual gate sweeps). The theoretically predicted locations of peaks (dashed lines), which are calculated using the electrostatic model and dimensions of the nanowire cross-section, coincide relatively well with the observed resistance curves, especially for small subband indices ℓ. This confirms that the spacing of gate dependent resistance peaks is related to the cross-sectional geometry. The resistance maximum occurs at $V_{\mathrm{DP}} = 4.01$ V for Device 4 and $V_{\mathrm{DP}} = 3.05$ V for Device 5. Model parameters: Al_2O_3 dielectric permitivity $\epsilon = 9.34$, top Al_2O_3 thickness 40 nm, and top Al_2O_3/gate width is nanowire width W plus 40 nm.

Gate voltage dependent resistance oscillations are set by the perimeter, P, and the capacitance of the device, C. Since there are smaller variations in the perimeter than cross-sectional area and it is likely the capacitance also varies between devices, it should be expected that the spacing of gate voltage resistance oscillations contains greater uncertainty compared with the periods of AB-like oscillations. Despite this, following the same analysis as Ref. [26], in Fig. 5.8 we plot the resistance $R(V_{\mathrm{G}})$ – averaged over several gate sweeps to eliminate artefacts such as e.g. jumps from trapped charges – in the vicinity of the resistance maximum $R(V_{\mathrm{DP}})$. We estimate the capacitance of Device 4 and Device 5 by utilising an electrostatic model for our full setup – including dielectric environment – and solving the Laplace equation using the finite element method. We make the simple assumption that the nanowire can be modelled as a perfect metal and that effects of quantum capacitance can be neglected for our setup. This calculation gives a capacitance $C = 66$ pF/m for the parameters of Device 4 and $C = 73$ pF/m for the parameters of Device 5. We use the estimated capacitance and the dimensions of each device to plot the theoretically expected resistance, $R(V_{\mathrm{G}})$, and positions of individual gate peaks (dashed lines). Note that the peak position varies with charge density $n \propto \mu^2$, such that the spacing of subband oscillations is approximately quadratic in the voltage difference from the location of the resistance maximum. From Fig. 5.8, despite the smaller variations in perimeter and additional uncertainty in capacitance, we see that the locations of observed resistance peaks correspond relatively well with the theoretically expected resistance curve, especially for small subband indices ℓ. In Fig. 5.8 all parameters of the theoretical curves are set by the electrostatic simulations and estimates of the nanowire cross-sectional geometry that are obtained from AB-like oscillations, meaning that there is no free fitting parameter.

Raw data of $R_{2\omega}$ and symmetric component

Upon sweeping the magnetic field B_z applied parallel to the gate-induced electric field E, the second-harmonic voltage $R_{2\omega}$ comprises an antisymmetric component $R^A_{2\omega}$ and a symmetric component $R^S_{2\omega}$; these two components can be easily separated by antisymmetrization/symmetrization of the B-dependence data. Figures 5.9a and 5.9c show the raw $R_{2\omega}$ data for V_G = 2 V and 4.32 V, respectively, from which the $R^A_{2\omega}$ data shown in Fig. 5.2b of the main text were extracted. The $R^S_{2\omega}$ component shown in Figs. 5.9b and 5.9d can have various trivial origins such as a diode-like effect at an imperfect contact.

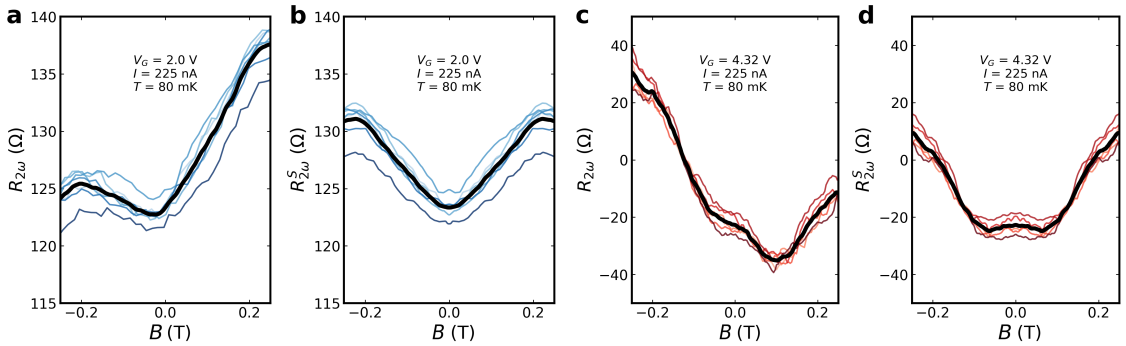

Figure 5.9: Raw $R_{2\omega}$ data and symmetric component $R^S_{2\omega}$ of Device 1, Section 1. a, Raw $R_{2\omega}$ vs B_z data at V_G = 2 V. **b,** The symmetric component $R^S_{2\omega}$ extracted from the raw data for V_G = 2 V. **c,** Analogously, raw $R_{2\omega}$ vs B_z data at V_G = 4.32 V. **d,** The symmetric component $R^S_{2\omega}$ extracted from the raw data for 4.32 V. The corresponding extracted asymmetric components $R^A_{2\omega}$ are shown in Fig. 5.2b of the main text. Coloured thin lines show the results of 6 sweeps, and the thick black line shows their average.

Magnetic-field-orientation dependence of γ for the in-plane and out-of-plane rotations

In addition to the magnetic-field-orientation dependence of $R^A_{2\omega}$ for the zx-plane rotation shown in the main text (Fig. 5.2d), we have taken similar data on Device 1 for the yz-plane rotation (Fig. 5.10) and found that the behaviour is also consistent with $\gamma \approx \gamma_0 \cos\alpha_2$, where α_2 is the angle of the B-field away from the z-direction in the yz-plane. Each data point was generated by averaging 6 (8) individual B-field sweeps at V_G = 2 V (4.32 V), while the error was calculated by a Min-Max method (though a standard deviation approach gives very similar results). We note that the γ_0 values for the zx- and yz-plane rotations at nominally the same V_G are slightly different; this is probably due to a difference in the details of the charge distributions and a slightly different chemical potentials for the two measurements, since the gating history was different.

We measured the magnetic-field-orientation dependencies for all three major rotation planes (xy, yz, and zx) in Device 4 at V_G = 3.26 V and the results are shown in Fig. 5.11. Each data point was generated by averaging 10 individual B-field sweeps, while the error was calculated by a Min-Max method. One can see that the $\gamma \approx \gamma_0 \cos\alpha$ dependence is reproduced for the zx- and yz-plane rotations, while γ remains essentially zero during the xy-plane rotation, which fully supports the vector-product type MCA with the $\boldsymbol{P}$ vector along the y-axis. Note that the maximum γ value observed in Device 4 reaches 1×10^5 $\mathrm{A^{-1}T^{-1}}$ (see Figs. 5.11a and 5.11b).

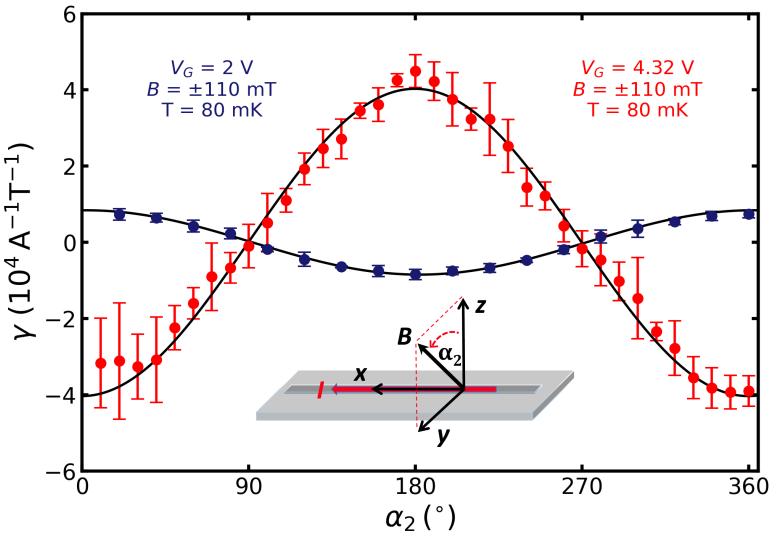

Figure 5.10: Magnetic-field-orientation dependence of γ for the yz-plane rotation in Device 1, Section 1. a, The MCA coefficient γ obeys $\gamma \approx \gamma_0 \cos\alpha_2$, where α_2 is the angle from the z-direction. The data shown here is for Device 1, Section 1, at V_G of 2 V (blue) and 4.32 V (red). Solid black lines are fits to the cosine function. The inset shows the definition of α_2 and the coordinate system.

Reproducibility of the magnetochiral anisotropy

To confirm the reproducibility of the experimental data supporting a giant MCA in BST nanowires, additional measurements have been performed on four devices (Device 1, 2, 3, 4) at various nanowire sections. All four devices had the same design (with slightly different width) and were fabricated from the same thin film in the same fabrication batch. The nanowire width was ∼200, ∼205, ∼210, and ∼200 nm in Devices 1 to 4, respectively, with the film thickness of ∼16 nm. In the following, we show representative data reconfirming the behaviours reported in the main text.

Figure 5.12 shows a data set to confirm the sign change in γ upon a slight change in the chemical potential. The data were taken on Section 1 of Device 1.
Figures 5.13 and 5.14 show further data, taken on Section 2 of Device 1 and Section 1 of Device 2, respectively, to demonstrate that our BST nanowires consistently show the large MCA. The three basic characteristics of the vector-product-type MCA are: (i) $R^A_{2\omega}$ depends linearly on B at low field, (ii) $R^A_{2\omega}$ is maximum for $\boldsymbol{B} \parallel \hat{\boldsymbol{z}}$ and vanishes when $\boldsymbol{B}$ is along $\hat{\boldsymbol{x}}$ or $\hat{\boldsymbol{y}}$, and (iii) $R^A_{2\omega}$ increases linearly with I. All three characteristics are reproduced.

Figure 5.15 shows supplemental data for Device 3 which was used for demonstrating the repeated sign change in γ as a function of V_G in the main text. The

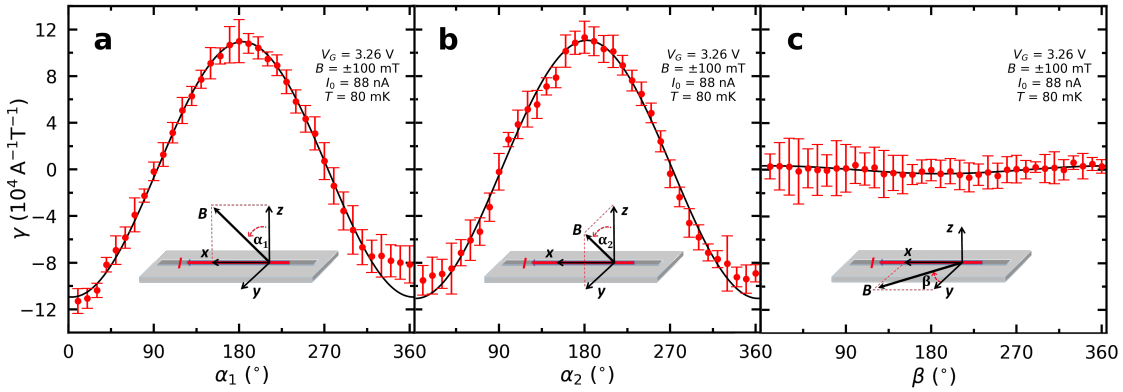

Figure 5.11: Magnetic-field-orientation dependence of γ for Device 4, Section 1. a,b,c At V_G = 3.26 V, the MCA coefficient γ was determined at low fields (-100 mT $\leq B \leq +100$ mT) while the magnetic-field orientation was gradually rotated in the zx, yz, and xy planes, respectively. Solid black lines are fits to the cosine function. Insets show the definitions of α_1, α_2 and β in each rotation plane.

V_G dependence of R is shown in Fig. 5.15a for a wide range of V_G. The I-linear increase of $R^A_{2\omega}$ is shown in Fig. 5.15b. The B-linear dependence of $R^A_{2\omega}$ for $\boldsymbol{B} \parallel \hat{\boldsymbol{z}}$ and vanishing $R^A_{2\omega}$ for $\boldsymbol{B} \parallel \boldsymbol{I}$ are shown for both positive and negative γ in Figs. 5.15c and 5.15d, respectively.

Figure 5.16 shows that Device 4, which was used for the full angular-dependence measurement (5.3.2, Fig. 5.11) and the temperature-dependence measurement (5.3.2, Fig. 5.17), also presents giant MCA. The three basic characteristics, B-linear dependence of $R^A_{2\omega}$ for $\boldsymbol{B} \parallel \hat{\boldsymbol{z}}$ at low field, vanishing $R^A_{2\omega}$ when $\boldsymbol{B}$ is along $\boldsymbol{I}$ or $\boldsymbol{P}$, and I-linear dependence of $R^A_{2\omega}$, are all confirmed.

Temperature dependence of MCA

To elucidate the temperature dependence of MCA, we measured γ of Device 4, Section 1, at V_G = 3.22 V at various temperatures up to 7 K (Fig. 5.17). We found that MCA weakens with temperature and diminishes towards ∼10 K. The temperature range in which MCA is observed, up to ∼10 K, is in good correspondence with the expected subband gap of ∼1 meV. It is useful to notice that this energy/temperature scale also dictates the AB-like oscillations in the MR for $\boldsymbol{B} \parallel \hat{\boldsymbol{x}}$, which was reported to diminish above a few Kelvin [25].

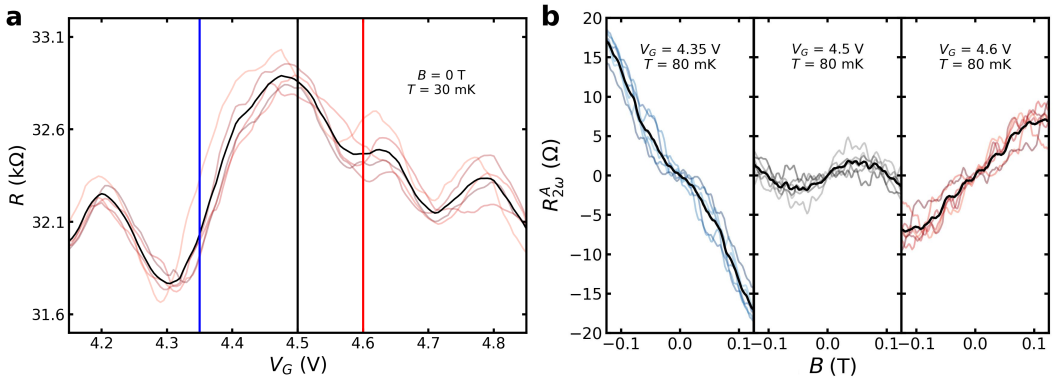

Figure 5.12: Sign change of γ upon changing the chemical potential in Device 1, Section 1. a, The V_G-dependence of R in the V_G range of 4.15–4.9 V obtained in a different sweep from that in Fig. 5.2a of the main text. Thin coloured lines are the data from 5 individual V_G sweeps and the thick black line is their average. The blue, black, and red vertical lines mark the V_G values at which the B-dependence of $R^A_{2\omega}$ was measured. **b,** Plots of $R^A_{2\omega}$ vs B_z at the V_G values of 4.35 V, 4.5 V, and 4.6 V, which span a peak in the $R(V_G)$ curve shown in panel **a**. The sign of $dR^A_{2\omega}/dB_z$ near B_z = 0 T (i.e. the sign of γ) changes in this V_G interval. Coloured thin lines show 6 individual B-field sweeps and the thick black line shows their average.

Comparison with MCA in other materials and with other non-reciprocal response

To put the giant MCA we observed in gated TI nanowires into context, we compare it with the MCA observed in other materials. Table 5.1 lists the materials for which relatively large MCA has been reported. In this table, the values of both γ and γ' (= γA, with A the cross-sectional area) are given for each material/structure, even though γ' is not an appropriate parameter to measure the MCA rectification in a mesoscopic system like TI nanowires or carbon nanotubes. Also, we list MCA observed in superconductors in this table, although the physical origin of the non-reciprocal response in superconductors is completely different and it exists only in a very limited range of current and temperature. One can see in this table that the γ value found in this study is the largest ever reported. In addition to listing the MCA in other materials, we also list the cases of relatively large non-reciprocal responses observed in magnetic materials/structures in Table 5.2. Since time reversal symmetry is spontaneously broken in these cases, these non-reciprocal effects do not belong to MCA (in which time reversal symmetry is broken by an applied magnetic field) and hence the MCA rectification coefficient γ is not well-defined. Nevertheless, one can see in this table that the

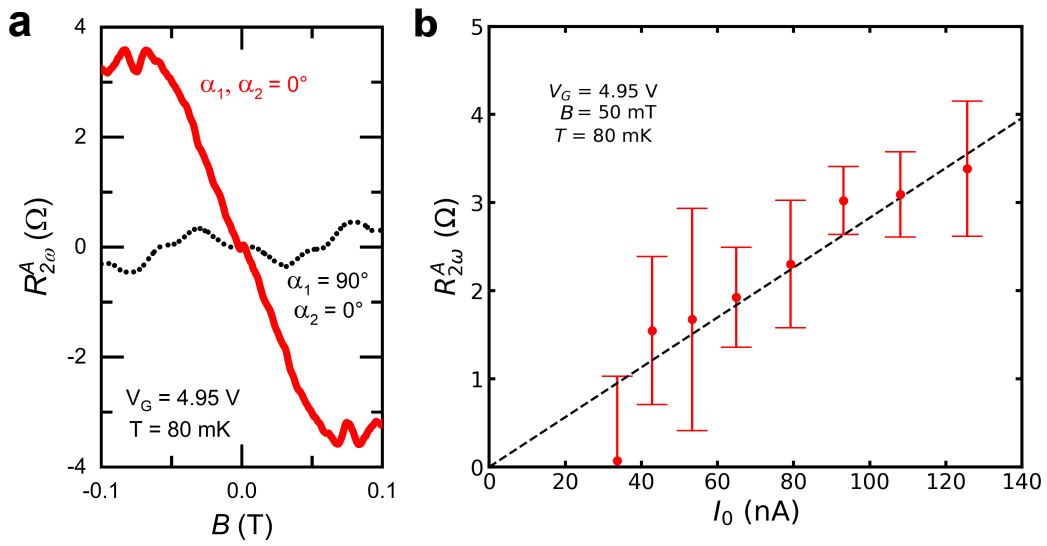

Figure 5.13: MCA in Device 1, Section 2. a, Averaged $R^A_{2\omega}(B)$ behaviours for $\boldsymbol{B} \parallel \hat{\boldsymbol{z}}$ (red solid line) and $\boldsymbol{B} \parallel \boldsymbol{I}$ (black dotted line) at V_G = 4.95 V measured on Section 2 of Device 1. Averages are obtained from 10 individual B-field sweeps. **b,** $R^A_{2\omega}$ at V_G = 4.95 V as a function of the ac excitation current I_0 for B_z = 50 mT. The black dashed line is a guide to the eye to mark the linear behaviour.

size of the rectification effects, measured with either $\Delta R/R$ or $\Delta R/R/i$ (where i is the current density), can be comparable or even larger than MCA.

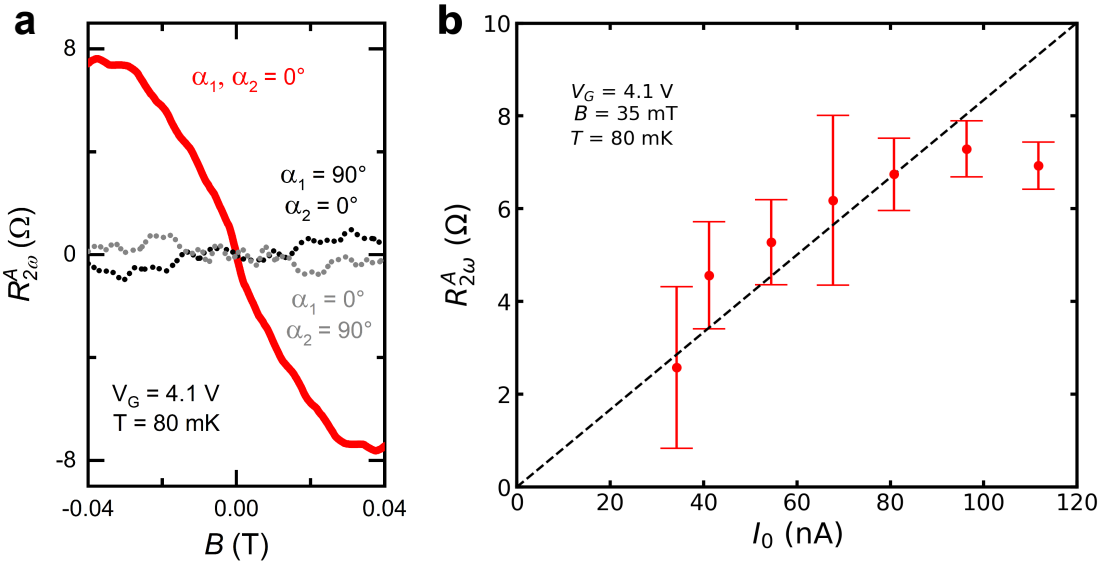

Figure 5.14: MCA in Device 2, Section 3. a, Averaged $R^A_{2\omega}(B)$ behaviours for $\boldsymbol{B} \parallel \hat{\boldsymbol{z}}$ (red solid line), $\boldsymbol{B} \parallel \boldsymbol{I}$ (black dotted line) and $\boldsymbol{B} \parallel \hat{\boldsymbol{y}}$ (grey dotted line) at V_G = 4.1 V measured on Section 3 of Device 2. Averages are obtained from 10 individual B-field sweeps. **b,** $R^A_{2\omega}$ at V_G = 4.1 V as a function of the ac excitation current I_0 for B_z = 35 mT. The black dashed line is a guide to the eye to mark the linear behaviour.

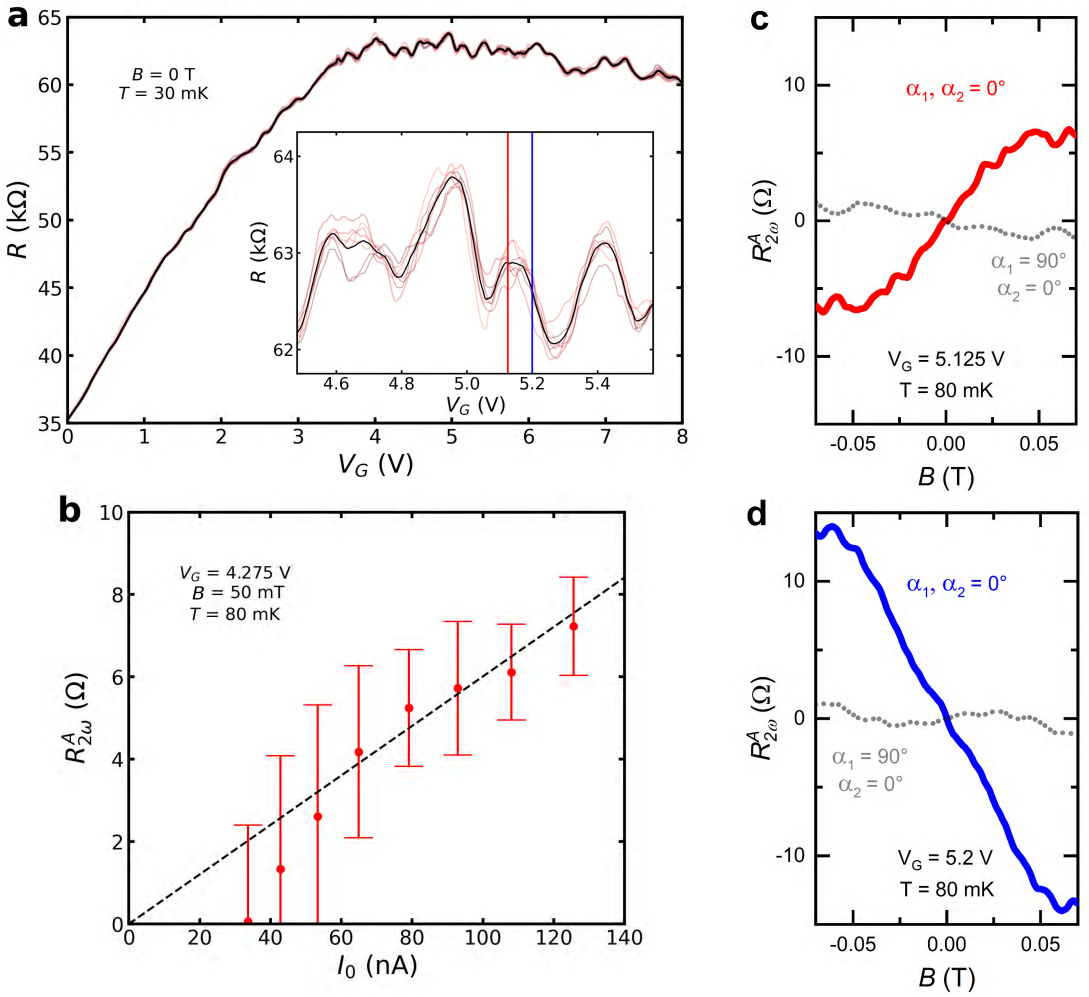

Figure 5.15: MCA in Device 3, Section 5. a, $R(V_G)$ behaviour of the Section 5 of Device 3 in a wide V_G range, presenting a broad maximum around $V_G \simeq 5$ V. Coloured thin lines show 7 uni-directional V_G sweeps and the thick black line shows the average. Inset shows a magnification of the V_G range 4.5–5.6 V; the red and blue vertical lines mark the V_G positions used for the $R^A_{2\omega}(B)$ measurements shown in panels **c** and **d**. **b,** $R^A_{2\omega}$ at V_G = 4.275 V as a function of the ac excitation current amplitude I_0 for B = 50 mT applied along $\hat{z}$. The black dashed line is a guide to the eye. **c,d** Averaged $R^A_{2\omega}(B)$ behaviours for $\boldsymbol{B} \parallel \hat{\boldsymbol{z}}$ (solid lines) and $\boldsymbol{B} \parallel \boldsymbol{I}$ (dotted lines) at V_G = 5.125 V (c) and 5.2 V (d). The sign of $dR^A_{2\omega}/dB_z$ near B = 0 T (i.e. the sign of γ) changes in this narrow V_G interval crossing a peak in the $R(V_G)$ curve. Averages are obtained from 10 individual B-field sweeps.

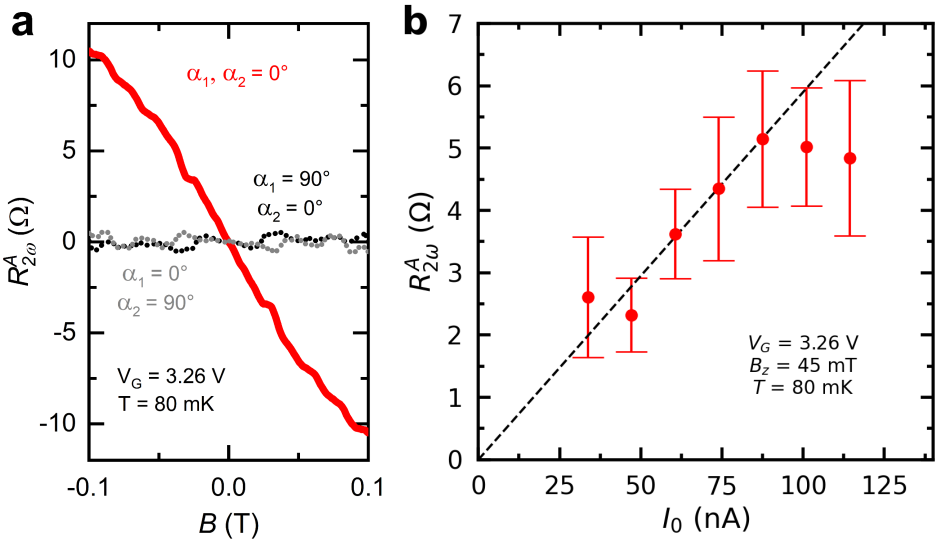

Figure 5.16: MCA in Device 4, Section 1. a, Averaged $R^A_{2\omega}(B)$ response for $\boldsymbol{B} \parallel \hat{\boldsymbol{z}}$ (red solid line), $\boldsymbol{B} \parallel \hat{\boldsymbol{x}}$ (black dotted line) and $\boldsymbol{B} \parallel \hat{\boldsymbol{y}}$ (grey dotted line) at V_G = 3.26 V measured on Section 1 of Device 4. Averages are obtained from 10 individual B-field sweeps. **b,** $R^A_{2\omega}$ at V_G = 3.26 V as a function of the ac excitation current I_0 for B_z = 45 mT. The black dashed line is a guide to the eye to mark the linear behaviour.

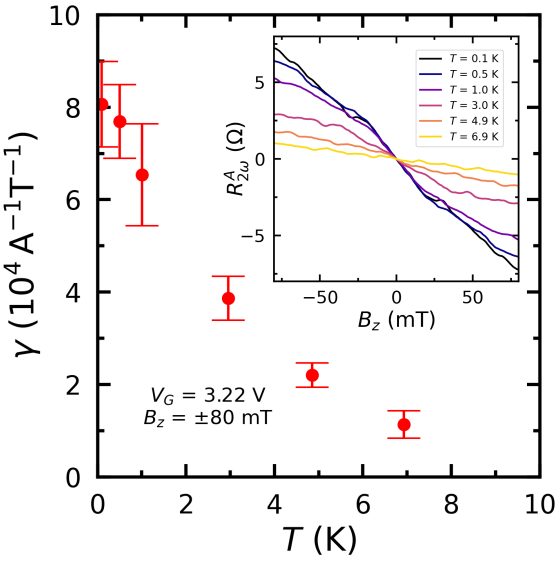

Figure 5.17: Temperature dependence of γ for Device 4, Section 1. a, The γ value at V_G = 3.22 V determined at low fields (-80 mT $\leq B \leq +80$ mT) at various temperatures up to 7 K. Inset shows the raw data of $R^A_{2\omega}$ vs B_z at various temperatures; each curve is an average of 10 individual B-field sweeps.

	Material	T (K)	B (T)	ΔR (Ω)	$R_{0,1\omega}$ (Ω)	$\Delta R/R$ (%)	i (A/m^2)	$\Delta R/R/i$ (10^{-8} m^2/A)	I (A)	Area (m^2)	γ (A^{-1}T^{-1})	γ' (m^{2}A^{-1}T^{-1})	MCA type	Ref.
Normal conductors	$(Bi,Sb)_2Te_3$ Device 1 Sec.1	0.08	0.11	36	32150	0.112	5×10^{7}	0.23	1.64×10^{-7}	3.3×10^{-15}	62100	2.1×10^{-10}	Vector-product	This study
	$(Bi,Sb)_2Te_3$ Device 1 Sec.2	0.08	0.05	6	14200	0.043	3.3×10^{7}	0.13	1.1×10^{-7}	3.3×10^{-15}	76800	2.5×10^{-10}	Vector-product	This study
	$(Bi,Sb)_2Te_3$ Device 2 Sec.3	0.08	0.035	14	12250	0.114	3×10^{7}	0.38	1×10^{-7}	3.3×10^{-15}	327000	1.1×10^{-9}	Vector-product	This study
	$(Bi,Sb)_2Te_3$ Device 3 Sec.5	0.08	0.05	14	62750	0.022	3.9×10^{7}	0.06	1.3×10^{-7}	3.3×10^{-15}	34300	1.1×10^{-10}	Vector-product	This study
	$(Bi,Sb)_2Te_3$ Device 4 Sec.1	0.08	0.1	20	22700	0.088	2.7×10^{7}	0.33	8.8×10^{-8}	3.3×10^{-15}	100000	3.3×10^{-10}	Vector-product	This study
	n-type Si FET	300	2	0.8	620	0.13	1×10^{10}	1.3×10^{-3}	1×10^{-3}	1×10^{-13}	0.1	1×10^{-14}	Vector-product	[88]
	[DM-EDT-TTF]$_2$ClO$_4$	300	3.2	0.59	3000	0.020	2×10^{5}	9.9	1×10^{-3}	5×10^{-9}	0.01	5×10^{-11}	Inner-product	[250]
	Carbon nanotube	2.5	14	23	10000	0.23	3.5×10^{10}	6.6×10^{-4}	3.5×10^{-7}	1×10^{-17}	230	2.3×10^{-15}	Inner-product	[241]
	$SrTiO_3$	7	0.18	0.45	50	0.9	8.3×10^{8}	0.1	5×10^{-4}	6×10^{-13}	20	1.2×10^{-11}	Vector-product	[251]
	BiTeBr	2	9	0.036	1000	0.0037	1.3×10^{9}	2.8×10^{-4}	1.3×10^{-4}	1×10^{-13}	1	3×10^{-12}	Vector-product	[92]
	WTe_2	300	14	0.027	180	0.015	7.1×10^{9}	2.1×10^{-4}	1.2×10^{-3}	1.7×10^{-13}	0.22	3.7×10^{-14}	Vector-product	[252]
	Ge(111)	15	1	120	29000	0.41	1.7×10^{5}	0.41	1×10^{-5}	6×10^{-11}	0.7	4.2×10^{-11}	Vector-product	[253]
	Bi_2Se_3	60	9	0.11	1800	0.0063	1.4×10^{9}	4.6×10^{-4}	5.6×10^{-3}	4×10^{-13}	0.0006	2.4×10^{-16}	Vector-product	[90]
	t-Te	300	1.5	-	-	0.01	1.3×10^{4}	77	6.5×10^{-3}	5×10^{-7}	0.00073	3.6×10^{-9}	Inner-product	[93]
	$ZrTe_5$	3	0.02	0.014	29.6	0.047	8.3×10^{4}	57	2×10^{-4}	2.4×10^{-9}	195	4.7×10^{-7}	Vector-product	[94]
Superconductors	MoS_2	2	0.7	1.8	32	5.7	1.1×10^{9}	0.51	1.7×10^{-5}	1.6×10^{-14}	3800	5.9×10^{-11}	Vector-product	[254]
	WS_2 nanotube	4	2	0.57	40	1.4	4.5×10^{6}	31	3.5×10^{-8}	7.9×10^{-15}	100000	7.9×10^{-10}	Inner-product	[255]
	Bi2Te3/FeTe	6.9	0.5	0.0057	0.36	1.6	6.7×10^{7}	2.4	2×10^{-4}	3×10^{-12}	0.00065	2×10^{-14}	Vector-product	[235]
	InAs 2DEG	1.45	0.09	400	45000	0.89	-	-	2.8×10^{-8}	-	4.15×10^{6}	-	Vector-product	[234]

Table 5.1: Magnetochiral anisotropy in normal conductors and superconductors: Adapted from Ref. [233] and some new entries, including all our samples, are added. When the values of the MCA coefficient γ and/or γ' were not given in the publication, they are calculated.

	Material	T (K)	B (T)	ΔR (Ω)	$R_{0,1\omega}$ (Ω)	$\Delta R/R$ (%)	i (A/m^2)	$\Delta R/R/i$ (10^{-8} m^2/A)	I (A)	Area (m^2)	Ref.
Magnet/ SC	YIG/MoGe	4	7.3	0.073	0.86	8.5	5.7×10^{4}	14900	0.00004	-	[256]
Magnet	Pt/Co	300	2	0.2	290	0.069	4.9×10^{11}	1.4×10^{-4}	0.0213	4.3×10^{-14}	[257]
	Ta/Co	300	0.2	0.014	574	0.0025	1.0×10^{11}	2.5×10^{-5}	0.0085	8.5×10^{-14}	[258]
	Pt/Py	300	0.015	0.04	40	0.1	1.1×10^{12}	9.1×10^{-5}	0.0033	3.0×10^{-15}	[259]
	Pt/Co	300	0.2	0.0031	170	0.0018	1.0×10^{11}	1.8×10^{-5}	0.003	3.0×10^{-14}	[260]
	Co_2MnSi/Pt	300	0.075	0.05	33000	0.00015	1.7×10^{11}	8.9×10^{-7}	0.41	2.4×10^{-11}	[261]
	GaMnAs	130	0.002	2.2	1720	0.13	7.5×10^{9}	0.0017	0.00015	2.0×10^{-14}	[262]
	MnSi	35	0.4	0.00011	1	0.011	1.0×10^{9}	0.0011	0.0025	2.5×10^{-12}	[263]
	$(Bi,Sb)_2Te_3$/ CoFeB	150	0.02	0.0085	730	0.0012	6.7×10^{9}	1.7×10^{-4}	0.0020	3.0×10^{-13}	[264]
	$(Bi,Sb)_2Te_3$/ $Cr_x(Bi,Sb)_{2-x}Te_3$	2	0.7	35	14000	0.25	6.3×10^{6}	3.97	5.0×10^{-7}	8.0×10^{-14}	[232]
	$(Bi,Sb)_2Te_3$/ $Cr_x(Bi,Sb)_{2-x}Te_3$	1.9	1	51	14000	0.23	2.5×10^{6}	15	6×10^{-7}	2.4×10^{-13}	[265]
	$CrNb_3S_6$	<200	2	$\mathcal{O}(10^{-6})$	-	-	1.1×10^{9}	-	0.0045	4.1×10^{-12}	[266]
QAHI	$Cr_x(Bi,Sb)_{2-x}Te_3$	2	0.1	4100	16000	26	1.3×10^{8}	21	0.0001	8.0×10^{-13}	[233]
	$Cr_x(Bi,Sb)_{2-x}Te_3$	0.5	0.1	190	16000	1.1	3.8×10^{6}	31	3×10^{-6}	8.0×10^{-13}	[233]

Table 5.2: Non-reciprocal responses in magnetic materials/structures: Adapted from Ref. [233] and some new entries are added. Here, the non-reciprocal responses are possible due to spontaneously broken time-reversal symmetry. Hence, the magnetic field B is playing only a supportive role and γ is not a well-defined parameter to characterize the non-reciprocal response. SC and QAHI stand for superconductor and quantum anomalous Hall insulator, respectively.

Chapter 6

SUMMARY AND OUTLOOK

This work explores the development and electronic transport phenomena of etched bulk-insulating topological insulator nanowires (TINWs) prepared from the 3D topological insulator (TI) $(Bi_{1-x}Sb_x)_2Te_3$.

Starting with Chapter 2, key theoretical concepts for 3D TIs as well as more specifically TINWs are introduced and a short review of the modern understanding of superconductivity is provided to give a framework for the observed transport effects. From considerations of topological classification derived from the Quantum Hall-effect, in systems with strong spin orbit coupling topological surface states (TSS) can arise due to the bulk-boundary correspondence. When a 3D TI is formed into a nanowire, the resulting discrete surface state subbands with characteristic Dirac-nature and helical spin polarization due to spin momentum locking can give rise to interesting transport phenomena, especially when coupled to a superconductor as studied here. A short review of the modern understanding of superconductivity in terms of Andreev-reflections and BTK-Theory provides an understanding of proximity induced superconductivity in TINWs so that results from measurements of S-TI-S Josephson junctions, especially the fractional Josephson effect under microwave-irradiation, can be understood. In Chapter 3, information on the material used in this study, $(Bi_{1-x}Sb_x)_2Te_3$ (BST), is given and some relevant properties are discussed. BST is a compensated 3D TI that can be grown as a thin film with Molecular-beam epitaxy and well-controlled quality, but that is also adversely effected by intrinsic disorder from charge compensation. When patterning such a surface-transport-dominated material during nanodevice-fabrication, treatment conditions need to be tuned carefully to not harm the quality of the surface state. In this regard relevant technical developments during this work are described. Finishing with a brief recap of the low-temperature measurement systems used allows to proceed to the discussion of the experimental results.

In Chapter 4, the successful preparation and characterization of etched bulk-insulating topological insulator nanowires (TINWs) in both normal-state and superconducting-state transport experiments is presented. From low-temperature measurements it is shown that the developed versatile and easy to adapt preparation procedure to obtain TINWs preserves the pristine quality of the initial BST thin film. In contrast to most previous reports, the NWs put forward here are bulk-insulating and the chemical potential can be tuned easily to the CNP by electrostatic gating. Characteristic periodic oscillations in electrical resistance both as a function of externally applied magnetic-field and gate-voltage give strong evidence for the formation of TSS and are studied to characterize the NWs quality. When superconducting transport is investigated in S-TI-S Josephson junctions on such TINWs of varying width, signatures of a 4π-periodic supercurrent contribution are observed in Shapiro measurements. In previous reports this has been associated with the formation of Majorana Bound States [8, 34, 40, 42]. However, even tough most trivial origins for the observed suppression of the first integer Shapiro step are ruled out here, such experiments cannot be conclusive [41]. Interface transparency in these S-TI-S junctions is likely limited by oxidization of the TI-surface at the contact interfaces, which in future studies could be prevented by e.g. in-situ capping or may be further improved by more work on contact cleaning procedures. Though evidence for the formation of MBS remains inconclusive, for the first time this preparation protocol meets the requirements of providing bulk-insulating TINWs with a well-controlled TSS that can be grown in reliable material quality and that can be patterned into interconnected branched arbitrary large-scale networks which can be successfully proximitized by a superconductor. This makes TINWs fabricated by etching a platform that is well-considerable for advanced detection and control proposals to study MBS [4, 5, 14].

Additionally, a previously unexpected manifestation of the TSS in TINWs was found, the occurrence of a giant magnetochiral anisotropy (MCA). In Chapter 5 the theoretical prediction and consecutive experimental confirmation of non-reciprocal transport in TINWs is reported, which is characterized by a outstandingly large MCA rectification coefficient $|\gamma| \sim 100000\ \mathrm{A^{-1}T^{-1}}$. Similar to previous comparable reports this effect is only observed at low temperatures, but in TINWs it is highly controllable via gate voltage and a magnetic field which cause the necessary splitting and shifting of the responsible spin polarized subbands. As non-reciprocal responses in quantum materials touch on fundamental aspects of modern condensed matter physics such as broken symmetries, topology, quantum confinement and correlations, MCA based on an intriguing combination of

these aspects points to an unexplored playground to substantially enhance the size of non-reciprocal transport effects.

As preparation of TINWs by etching is shown to not adversely effect the properties inherited from the starting material, future work would benefit from a deepened understanding of how to reduce disorder in the involved TI materials and interfaces, as has been achieved in the III-V semiconductor community after immense efforts. Imperfect charge compensation for example is known to cause chemical potential variations that cause ambiguity of macroscopic transport signatures and oxidization of 3D TIs and respective contact interfaces is not well studied, the latter severely limiting the achieved contact interface transparencies so far. In-Situ deposition of a superconductor similar to what has been reported for selective-area grown 3D TIs [40, 42], for example in a flipped materials stack with BST on top so that it can be etched easily, could help to reliably induce superconductivity. Alternatively, removable surface termination like briefly tried in this work or well-controlled self-formation of superconducting contacts like with PdTe [267] are conceivable. These improvements are well-compatible with the presented top-down preparation of etched TINWs, and once highly transparent interfaces that host more robust induced superconductivity have been established, Shapiro-experiments with narrow NWs in a parallel magnetic field strong enough to tune on and off the 1D TSS mode would be interesting [34]. Even for the existing preparation technique, enhanced microwave coupling to the TINW junctions or Josephson radiation experiments could lead to new insights [41]. Such experiments however can not give conclusive evidence for the presence of MBS, for which reason future work needs to cover end-state tunneling spectroscopy and eventually braiding experiments, both which seem feasible with the TINW preparation procedure presented in this work.

The presented results are therefore evidence that etched 3D TINWs are a scalable platform that provides all crucial ingredients, the existence and control of a quasi-1D TSS mode in a bulk-insulating system in conjunction with induced superconductivity, to investigate the presence and control of MBS as well as (potentially superconducting) diode effects in TIs. Thereby this work serves as a steppingstone to enable further fundamental research on TINWs and their technical applications in for example rectifiers and topological quantum computation.

Chapter 7

APPENDIX

7.1 Appendix A: Nanodevice-Fabrication details

7.1.1 Further key fabrication process in detail

To ensure reproducibility, critical fabrication steps are discussed and commented on in more detail in the following:

Al_2O_3 removal
For the removal of the Al_2O_3 cap in areas that directly contact the nanowire, Transene-D Aluminium etchant is used just before metallization. For less sensitive areas, a TMAH-based optical developer (AZ326 MIF or NMD, both 2.38% TMAH) is applied due to the simplicity of the process (consider that TMAH does etch BST though). For Transene-D at 50 C°, an etch rate of $\sim$1 nm/s was found which is sensitive to exact temperature conditions as it roughly halves every 10 C° with decreasing temperature. Halving the etch rate at 40 C° to stabilize process conditions was tested to not be beneficial [174]. Interestingly, Transene-D is found to be quite selective towards BST. No change in height or appearance was measured for BST exposed to these conditions for up to 15 minutes. These findings are in agreement with other reports that highlight Transene-D's good selectivity towards elements with similar properties compared to Bi, Sb and Te [196] and allow to use Transene-D for e.g. $\sim$10 s to remove a protective Al_2O_3 cap of $\sim$4 nm without harming the material itself notably. For further tests with Transene-D at 40 C° and 50 C°, see reference [174]. Note that at lower temperatures resist adhesion problems that occurred occasionally during this etching process happened less often. The typical process flow is as follows:

1. Heated Transene-D-etch:

   (a) Carried out by heating of Transene-D and several H_2O beakers to 50 C° (Transene-D etch rate of Al_2O_3 of $\sim$1 nm/s).

(b) After immersion (e.g. for 10 s in the case of a 4 nm Al_2O_3-cap (>2x overetch)) the etch should be stopped by immersion of the sample into several beakers of heated H_2O over the course of 2 min followed by a cold water stop for >2 min as well as H_2O-rinsing (gentle to not stress the resist).

(c) Common issues: A heated etch as described here can be demanding in terms of resist adhesion, especially when the layer it adheres to, the Al_2O_3, is eaten up underneath. Depending on details of the resist coating, adhesion might be suboptimal, resulting in flaking of the resist during the etch, that, if unnoticed, causes deposition of metal in unwanted areas of the device in the consecutive fabrication step, often resulting in a loss of the sample. This can be overcome by using an adhesion promoter, e.g. AR 300-80 [268], which should be coated at 4k rpm and baked for 2 min at 60 C°. HMDS exhibits only a marginal adhesive effect in the case of PMMA.

2. TMAH-etch:

- Carried out by simple immersion of the sample into room-temperature AZ326 MIF, for example for 6.5 min for a 40 nm-thick dielectric (TMAH etch rate on $Al_2O_3 \sim 10$ nm/min - using some 50% over-etch here), followed by an H_2O-stop.
- Note that these alkaline TMAH developers attack BST, too. Visible deterioration of the BST around the bond pads for example can be used as an qualitative indication for a fully completed removal. Removing the Al_2O_3 cap with TMAH in contact areas of superconducting devices resulted in interfaces of lesser quality, showing multiple transition and jump features in dV/dI which suggest incomplete removal of the oxid similar to what has been observed for 40 C° Transene-D etching [174].

Wet-etching

Since surfaces can be degraded by oxidization and ion-bombardment related damage that negatively influences the quality of contact interfaces as well as coherent transport, wet etching is used to remove degraded parts as it is known for defect-free ablation of material. To remove and clean residual BST after NW-etching, 1:3 H_2SO_4(1 mol/l):H_2O_2(35 wt%) (dilute version of what is commonly known as 'Piranha-etch') cooled to $\sim$ 8 C° is used in a 1:8 ratio with DI-water, resulting in an lateral etch-rate of $\sim$12 nm/s on BST. Cooling is reported to result in more homogeneous etching that promotes smoother surfaces, thereby smoother

NW side-surfaces. For vertical wet-etching however, strong variations in etch speed are found that depend on the local defect landscape. For this reason, for vertical etching dry-etching should be used to remove the bulk of material.

Wet contact clean

For contact cleaning, a process shown by former group members to be beneficial for $BiSbTeSe_2$ was used. It consists of a O_2-RIE dry etch to ash resist residues after development ($Oxford$ RIE settings are 20 W, 50 sccm and 7-15 s etch) followed by a 30 s dip into 1:10 HCl(32%):H_2O. This process is summed up under the label 'ex-situ-cleaning'. It is noted that, strikingly, HCl is found to not attack BST itself significantly: HCl(32%):H_2O up to 1:1 ratio is not changing the height of BST film after 2 min exposure. Similar results are obtained for Hydrofluoric acid (HF) etching, where a dip for 6 min into 0.2 % HF resulted in an unchanged thickness in AFM. Unravelling the details of the non-trivial etch chemistry is of interest for further studies.

Transfer in Nitrogen-atmosphere

To form good superconducting contacts, the interface between electrode and material should be as clean as possible. Oxidization is considered the main adversary for good proximitization, for which reason the exposure of the contact areas after development and Al_2O_3 cap removal to air was minimized by a process that involves transferring the sample to the deposition chamber in a N_2-atmosphere created in a $Sigma - AldrichAtmos$ bag (Z564451).

This is done in the following way: The sample is in H_2O after the Al_2O_3-cap-removal-procedure to stop the etching process. The last etch-stop H_2O-beaker can then be transferred to a N_2-bag which is connected to the load-lock of the used deposition chamber. After sealing the bag, it can be flushed continuously with N_2 for about 15 min while in parallel pumping the bag/load-lock with the backing pump of it's turbopump, eventually creating a N_2-atmosphere in which the sample can be removed from the water without exposure to air. Note that the effort of this procedure is only reasonably beneficial when the time between breaking the vacuum after growth and capping is kept short (meaning that transfer to metallization without such a N_2-bag would add a significant amount of time to the overall ambient exposure). Additionally, this bag was not compatible with our Plassys deposition machine, hence electrode materials tried with this machine could have suffered from additional oxidization after cap-removal and contact clean.

Ar-InSitu-Cleaning

To test the effectiveness of Ar-InSitu-cleaning for BST, the consequences of removing 1-2 nm of material from the surface in-situ has been investigated for the available Mantis UHV sputter deposition machine. Devices consisting of two gate-tuneable Hall-bars in series were fabricated, while one channel was treated with the to be tested cleaning procedure and the other channel was kept pristine (Fig. 7.1 a). This way, growth related inhomogeneities and fabrication induced changes could be neglected, as directly neighbouring Hall-bars exposed to similar conditions where compared. A low power etching (60 W) was used, calibrated for our machine to remove $\sim$0.6 nm/min of material, and samples from the same BST-film were exposed to i) 7 s O_2-RIE (20 W, 50 sccm), 30 s of 1:3 HCl(32%):H_2O ('Ex-Situ-cleaning') plus 240 s Ar-in-situ cleaning, ii) 'Ex-Situ-cleaning' plus 30 s of Ar-in-situ cleaning and iii) 'Ex-Situ-cleaning' only. As shown in Figure 7.1 b, most strikingly, when $\sim$2.4 nm of material on one of the Hall-Bars is removed (240 s etch), the channel has a severely degraded appearance with a visible increase of roughness. 30 s of etching still shows a gentle change in surface morphology (Figure 7.1 c) while no changes are visible for just 'Ex-Situ-cleaning' (Figure 7.1 d). Simply based on the paradigm that the surface should not be visibly harmed, these results suggest that Ar-in-situ cleaning should be used only at lowest power for times below 30 s.

Superconducting Contacts

The following available contact metals have been considered for fabrication of TINW Josephson junctions on BST: Ti (thermally evaporated), Pt (sputtered) and Pd (sputtered) were tested as buffer layer materials which are commonly used to increase adhesion and to facilitate good contacts by more suitable work-function matching between material and metal electrode. As superconducting electrode materials, Nb (sputtered), V (thermally evaporated), Al (thermally evaporated) and Ta (sputtered) were accessible. Using Nb was most successful, which allowed to obtain the results discussed in chapter 4. Deposition in the available Mantis UHF sputter deposition machine has been carried out after loading the sample to a base pressure of <5e-10 Torr at 300 W, 70 sccm Ar-flow and with a substrate bias of 100 V. Other electrode material combinations have not been promising (see Table 3.5).

For example although Al can be successfully used together with a Ti-buffer layer in $BSTS_2$-flakes, no working Josephson Junctions could be obtained with this combination on bulk-insulating BST. In an early try on uncapped bulk-conducting

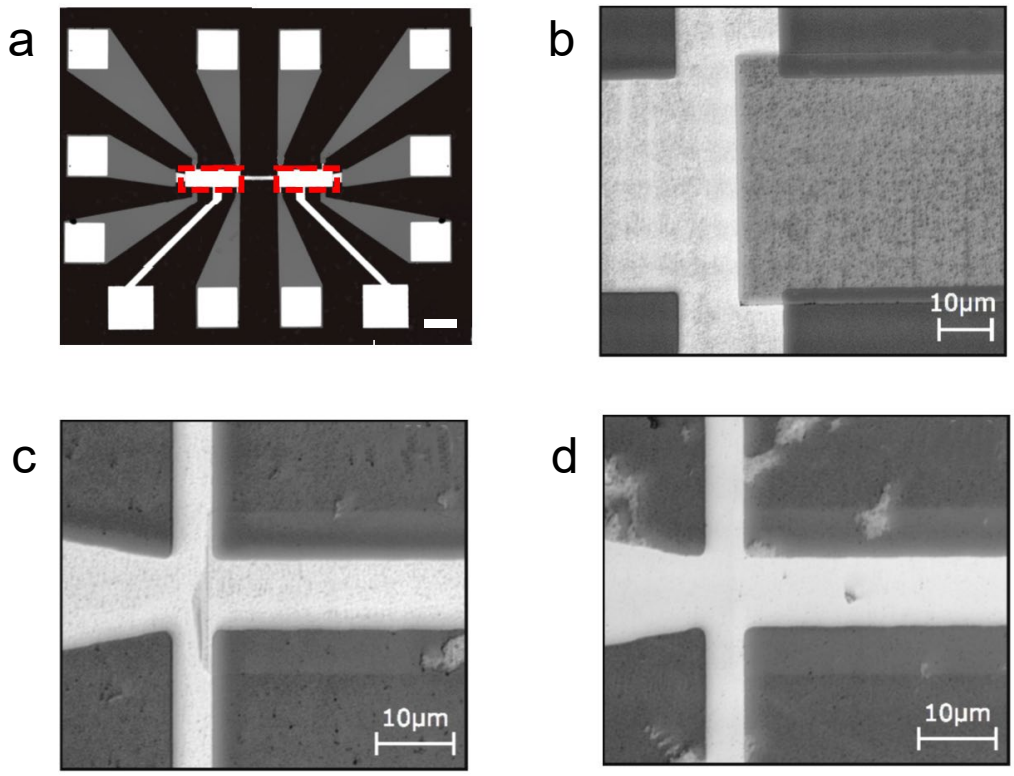

Figure 7.1: Ar In-Situ cleaning study on gated BST Hall-Bars. a, Laser-microscope image of a Hall-bar device with two independent and gate-able sections (marked red). Scale bar indicates 100 μm. **b,** SEM-image of the right Hall-bar section after exposure to the Ex-Situ-clean-procedure plus 240 s of 60 W Ar-InSitu-cleaning. **c,** Ex-Situ-clean-procedure plus 30 s of 60 W Ar-InSitu-cleaning and **d,** Ex-Situ-clean-procedure only.

BST, Ti/Al contacts did yield partial superconducting transitions. However, multiple tries on bulk-insulating BST by different group members yielded negative results, namely Josephson Junctions with contact resistances R_C of a few kΩ, which increased over time during handling of the sample at ambient conditions. Quickly capping the sample with Al_2O_3 after metallization did not help. These results suggested unfavourable degradation at the interface due chemical reactions.

V was reported to work on Bi_2Se_3 [38] and $BSTS_2$ flakes [205], but turned out to be challenging on BST thin films due to significant strain issues. This problem was mitigated by using stacks involving Ti and Al, but eventually contact resistances remained unpromising. In conjunction with the observation of aging found for Ti/Al contacts, reactive Ti was suspected to potentially cause some undesired interface reactions with BST or its oxide.

7.1.2 List of fabrication parameters

In the following, the fabrication processes for a typical top-gated normal-state transport TI-NW device as well as for a TI-NW device with superconducting contacts are listed in detail.

Selection criteria & quality of typically used BST
To promote successful experiments, BST films used are selected on the criteria listed in the following. In general, an optimum of the below-mentioned properties is desired, but practically often compromises are made, depending on the experiment and the availability of material.

- Electronic Transport properties: Carrier density n_{2D} & mobility μ
  - Bulk-insulating BST thin films selected for fabrication usually show properties similar to the ones depicted in chapter 4, 5.
  - Typically, a carrier density of $n_{2D} \leqslant 1 \times 10^{13}$ cm^{-2} is selected. Since fabrication is found to introduce a shift of the carrier type from n- to p-type as discussed earlier, usually n-type films are selected which if chosen correctly shift closer to CNP during fabrication.
  - As high as possible electron mobility μ is desired, typically at least $\mu \geqslant$ 300 cm^{-2}/Vs.
  - Samples with two-band transport, therefore a composition gradient along the crystallographic c-axis, are not used.
- Structural properties: Thickness & Morphology
  - Thickness: Typically, fabrication is optimized for films of thickness t = 16-25 nm. From experience, this results in the highest quality material and fits well with experimental requirements such as NW-cross-section. The thicker the film, the rougher it becomes.
  - Morphology: Typically, roughness from triangular terraces should be <3-5 nm and no holes should be visible. It is noted, that the morphology can significantly vary across the film due to temperature gradients during growth, something which is more easily seen in SEM than AFM. It is advised to consider this when positioning devices on the film.
- Growth related parameters:

- Due to the aforementioned aging, usually only films that are freshly grown less than 4 weeks ago are selected for fabrication, with the majority being much fresher (1-2 weeks from growth to final device).
- Capping times should be <10 min, preferably as fast as possible (considering ALD-capping related issues mentioned before).

Fabrication process flow: Normal-state TI-NW devices

1. Nanowire-etching:
   (a) Basic clean: Typically $\geqslant$2 min Aceton dip, $\geqslant$1 min IPA dip, both with weak ultrasonication and rinse upon transfer.
   (b) Coating: Coating PMMA A4 at 4K rpm (resulting in $\sim$220 nm thickness), followed by baking at 120 C$^\circ$ for 10 min and coating of conductive E-spacer resist at 2K rpm to be able to expose on insulating sapphire substrates without charging. The sample can be glued to a larger piece of Silicon with PMMA if it is too small to handle or shows severe edge bead.
   (c) EBL: 10 kV with 30 μm aperture, a base-dose of $\sim$120 μC/cm^2 and a beam speed of <10mm/s was chosen, while larger structures were written fast and with less accuracy by using larger apertures (beam currents) or step size.
   (d) Development: Clean E-spacer in 60 s DI water, followed by a thorough blow-dry. Development in 90 s MIBK:IPA (1:3), followed by a 30 s IPA stop + rinse.
   (e) Etching:
      i. O_2-RIE ash: 10 s of 20 W O_2-plasma at 50 sscm is used to remove residual resist after development (material still protected by Al_2O_3).
      ii. Ar-plasma etch: E.g. a 18 nm thick film is typically etched for $\sim$3.5 min in 300 W (50 sccm) to etch through the harder Al_2O_3-cap (removing already some of the BST, too), followed by a more gentle etch of $\sim$1.5 min of 20 W (50 sccm) to remove the remaining BST without damaging the NWs side-walls with high ion-energies too much. Exact etch-times depend on cap and film-thickness.
      iii. Wet etch: ((H_2SO_4:H_2O_2):H_2O) ((1:3):8) is used to remove residual BST as well as damaged material from the sidewalls of the NW. To ensure a more controlled etch, the etchant and DI water are cooled to $\sim$8 C$^\circ$. After etching, stop in DI water.

iv. Strong clean: To be able to remove plasma-hard-baked resist residues, cleaning in 80 C° N-Methyl-2-pyrrolidon (NMP) for >20 min is carried out. After brief ultrasonication in NMP, it is important to thoroughly clean NMP in Aceton, also with brief ultrasonication, to remove greasy NMP residues. Finish with an IPA clean.

2. Metallization:

   (a) Coating: Coat PMMA A4 at 4K rpm, followed by baking at 120 C° for 10 min and E-spacer coating at 2K rpm. Optionally, in later stages of the project an adhesion promoter (AR 300-80 new) was coated (4k rpm - 2 min bake at 60 C°) before PMMA to enhance process stability during etching.

   (b) EBL: 10 kV with 30 μm aperture, a base-dose of $\sim$120 μC/cm^2 and a beam speed of <10 mm/s was chosen, while larger structures were written fast and with less accuracy by using larger apertures (beam currents) or step size.

   (c) Development: Clean E-spacer in 60 s DI water, followed by a thorough blow-dry. Development in 90 s MIBK:IPA (1:3), followed by a 30 s IPA stop + rinse.

   (d) Contact clean:

      i. O_2-RIE clean: 10 s of 20 W O_2-plasma at 50 sscm is used to remove residual resist after development (material still protected by Al_2O_3).

      ii. Al_2O_3 cap-removal: As discussed earlier in subsection 7.1.1, typically by immersion in Transene-D heated to 50 C° for 10-15 s, followed by several etch-stops, first in 50 C° H_2O, then later in cold H_2O and with rinsing.

      iii. (Optional) Wet HCL clean: Dip into 1:10 HCl:H_2O for 30 s, followed by an etch-stop and rinse in DI-water. HCl:H_2O ratio was sometimes increased up to 1:3. Note that the resist tends to be brittle and weakly attached to the surface after the Transene-D etch, for which an adhesion promoter can help.

   (e) Metallization:

      i. Transfer to deposition chamber: Fast (typically <1 min) transfer to deposition chamber and vacuum after cap removal, or transfer without exposure to ambient conditions after cap-removal in N_2-atmosphere (see subsection 7.1.1).

ii. InSitu-clean: Typically for 5-10 s at the lowest power possible (43 W, at 20 sccm Ar-flow, 15 ° throttle valve, 1.05/1 A emission/discharge bias).

iii. Metal-deposition: 5/50 nm Pt/Au in common deposition settings

(f) Liftoff: >20 min in 80 C° NMP or >60 min room temperature NMP, followed by pipette blow of solvent in the beaker and weak ultrasonication depending on liftoff results. Finish with an Aceton clean (>2min, weak ultrasonication & rinse) and IPA clean. Soft metals like Pt/Au usually lift-off very easily and good results are obtained routinely.

3. Dielectric, Contact-pad opening & Top-gate:

(a) Dielectric deposition: Sample is typically covered with 40 nm Al_2O_3 grown in ALD at 80 C°.

(b) Contact pad opening:

- Exposure: Use EBL recipe similar to the ones mentioned above or preferably use faster Optical Laser Lithography.
- Optical Litho recipe:
  - Coating: AZ1505 spun at 4k rpm, followed by a 1 min bake at 100 C°.
  - Exposure: 10 mW 20-35% power (depending on dose-tests) + filter in Heidelberg Instruments μPG Laser Lithography machine
  - Development & Postbake: 20 s development in AZ326 MIF, followed by DI-water stop and rinse. Add a 1 min 120 C° postbake to increase resist stability during consecutive etching.
- Dielectric etching: As described in subsection 7.1.1, typically by immersion of the sample into room-temperature AZ326 MIF, for example for >6.5 min for a 40 nm-thick dielectric, followed by an etch-stop in DI water. Also possible to do it with Transene-D.

(c) Top-gate fabrication

i. Exposure: Basic EBL or optical lithography with recipes as mentioned above.

ii. Metal-deposition: 5/50 nm Pt/Au with common deposition parameters.

iii. Liftoff: Aceton, potentially heated to 60° to speed up the process, or NMP followed by pipette blow and mild ultrasonication, Aceton rinse and IPA-clean.

Fabrication process flow: Superconducting TI-NW devices
The fabrication of superconducting TI-NW devices resembles that of normal-state devices. However, very careful attention needs to be paid to sensitive contact clean and metallization parameters, as they are crucial and for the success-rate. Exemplary, below a recipe for the deposition of Nb-contacts.

1. Nanowire-etching:
   (a) Analog to above listed normal-state device nanowire-etching.
2. Metallization:
   (a) Coating: Coat PMMA A4 at 4K rpm, followed by baking at 120 C° for 10 min and E-spacer coating at 2K rpm. Optionally, in later stages of the project an adhesion promoter (AR 300-80 new) was coated (4k rpm - 2 min bake at 60 C°) before PMMA to enhance process stability during etching.
   (b) EBL: 10 kV with 20/60 μm aperture, a base-dose of $\sim$120 μC/cm^2 and a beam speed of <10 mm/s was chosen, while larger structures were written fast and with less accuracy by using larger apertures (beam currents) or step size. To achieve reliable and small gaps, refocus close to the NWs. Typically, refocusing once for 4 devices is sufficient. Proximity-error-correction (PEC) gave no reliable results with BST on sapphire as it frequently caused underexposed but barely visible resist residues to remain in the contact areas.
   (c) Development: Clean E-spacer in 60 s DI water, followed by a thorough blow-dry. Development in 90 s MIBK:IPA (1:3), followed by a 30 s IPA stop + rinse.
   (d) Contact clean & metallization:
      i. O_2-RIE: 10 s of 20 W O_2-plasma at 50 sscm is used to remove residual resist after development.
      ii. Al_2O_3 cap-removal: As discussed in subsection 7.1.1, typically done by 10-15 s etching in 50 C° Transene-D followed by several DI water etch stops to remove a 4 nm Al_2O_3 cap.
      iii. (Optional) Wet HCL clean: Dip into 1:10 HCl:H_2O for 30 s, followed by an etch-stop and rinse in DI-water (adhesion promoter advised).
      iv. Metallization (as discussed in subsection 7.1.1):

- Metallization-chamber preparations: Check pressure of chamber (preferably <5e-10 Torr) and whether sample holder can be biased. Presputter metal (Nb) target without having the sample in the main chamber.
- (Optional) N_2-atmosphere transfer: Fast transfer of the sample in DI water from the etch stop to the N_2-bag, 15 min N_2-flush & pump, then remove it from the DI-water and blow it dry for loading (as specified in subsection 7.1.1).
- InSitu-clean: Typically for 5-10 s at the lowest power possible (43 W, at 20 sccm Ar-flow, 15 ° throttle valve, 1.05/1 A emission/discharge bias) as specified in subsection 7.1.1.
- Metal-deposition: 45/5 nm Nb/Au with common deposition settings (using a 300 V substrate bias).

(e) Liftoff: >20 min in 80 C° NMP plus overnight room temperature NMP, followed by pipette blow of solvent in the beaker and weak ultrasonication depending on liftoff results. Finish with an Aceton clean (>2min, weak ultrasonication & rinse) and IPA clean. Nb is difficult to lift-off due to it's hardness and 'fencing' (sidewall deposition during sputtering causing causing 'fences' of metal at the lift-off edges).

7.2 Appendix B: Exploration of other 3D TI nanowires

7.2.1 VLS-grown BST NW

As discussed earlier, the most common preparation technique to obtain narrow nanowires is from Vapour-Liquid-Solid (VLS) growth in a sealed quartz tube in a tube furnace. After exploring such growth in first attempts together with Dingxun Fan, successful growth of sub-100 nm and μm-long $(Bi_{1-x}Sb_x)_2Te_3$ (BST) TINWs was achieved, as shown in Figure 7.2a. Transport characterization enabled first optimization of the compensation to later achieve bulk-insulating behaviour. Further development by Felix Münning and Oliver Breunig lead to the first successful observation of quantum confinement of the Dirac surface states in bulk-insulating BST TINWs as a function of gate-tuning of the chemical potential across the system's Dirac point [26].

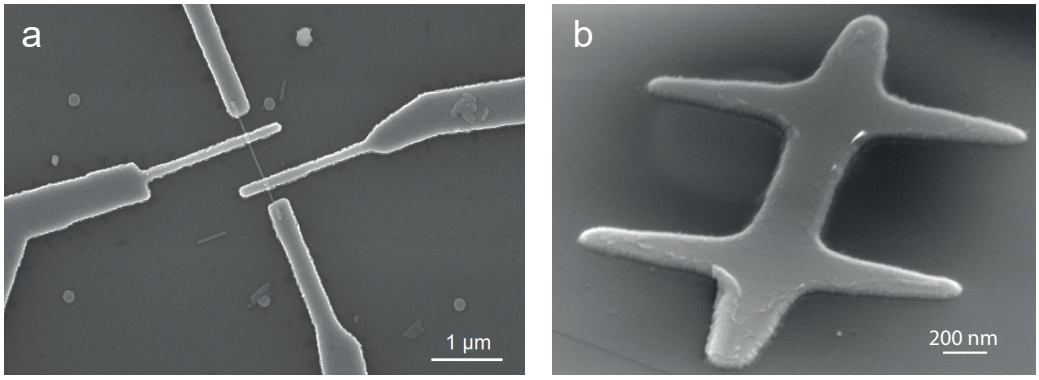

Figure 7.2: Other investigated types of TINWs and nano-ribbons prepared in early stages of this work. a, SEM image of a narrow VLS-grown BST TINW contacted with Pt/Au leads. **b,** Tilted-angle SEM image of a 200 nm wide TI nano-ribbon in Hall bar shape etched from a BSTS2-flake to estimate the potential of preparing etched BSTS2-NWs. The proposed pattering technique results in smooth side surfaces for flake-NWs down to sub-100 nm width without visible indications of degradation.

7.2.2 NWs etched from exfoliated BSTS2 flakes

$BiSbTeSe_2$ is a quaternary 3D TI compound that is considered to be one of the most bulk-insulating TI materials to date. Thin flakes exfoliated from $BiSbTeSe_2$ bulk single crystals have been reported to exhibit comparably clean transport characteristics and robust proximity-induced superconductivity in TI-S-TI Josephson junctions [1, 108]. Though infeasible for scaling due to the requirement of finding and marking individual randomly distributed flakes, in principle it is possible to prepare etched TINWs in the same way as reported for thin films. This approach has been succesfully tested in early stages of this work and was shown to result in NWs in Hall bar geometry with smooth side surfaces that show no indications of fabrication induced degradation (Figure 7.2b). More recent yet unpublished work by Junya Feng shows the promise of this approach and makes it interesting to explore etched flake TINWs further.

BIBLIOGRAPHY

[1] Y. Ando, "Topological insulator materials", Journal of the Physical Society of Japan **82**, 102001 (2013).

[2] H. F. Legg, M. Rößler, F. Münning, D. Fan, O. Breunig, A. Bliesener, G. Lippertz, A. Uday, A. A. Taskin, D. Loss, J. Klinovaja, and Y. Ando, "Giant magnetochiral anisotropy from quantum-confined surface states of topological insulator nanowires", Nature Nanotechnology **17**, 696–700 (2022).

[3] M. Rößler, D. Fan, F. Münning, H. F. Legg, A. Bliesener, G. Lippertz, A. Uday, R. Yazdanpanah, J. Feng, A. Taskin, and Y. Ando, "Top-Down Fabrication of Bulk-Insulating Topological Insulator Nanowires for Quantum Devices", Nano Letters **23**, 2846–2853 (2023).

[4] J Manousakis, A Altland, D Bagrets, R Egger, and Y. Ando, "Majorana qubits in a topological insulator nanoribbon architecture", Phys. Rev. B **95**, 165424 (2017).

[5] T. Karzig, C. Knapp, R. M. Lutchyn, P. Bonderson, M. B. Hastings, C. Nayak, J. Alicea, K. Flensberg, S. Plugge, Y. Oreg, C. M. Marcus, and M. H. Freedman, "Scalable designs for quasiparticle-poisoning-protected topological quantum computation with Majorana zero modes", Phys. Rev. B **95**, 235305 (2017).

[6] A Cook and M Franz, "Majorana fermions in a topological-insulator nanowire proximity-coupled to an s-wave superconductor", Phys. Rev. B **84**, 201105 (2011).

[7] O. Breunig and Y. Ando, "Opportunities in topological insulator devices", Nature Reviews Physics **4**, 184–193 (2022).

[8] F. Dominguez, F. Hassler, and G. Platero, "Dynamical detection of Majorana fermions in current-biased nanowires", Phys. Rev. B **86**, 140503 (2012).

[9] H. F. Legg, D. Loss, and J. Klinovaja, "Superconducting diode effect due to magnetochiral anisotropy in topological insulators and Rashba nanowires", Phys. Rev. B **106**, 104501 (2022).

[10] E. Majorana, "Teoria simmetrica dell'elettrone e del positrone", Il Nuovo Cimento (1924-1942) **14**, 171–184 (1937).

[11] J. Alicea, "New directions in the pursuit of Majorana fermions in solid state systems", Reports on Progress in Physics **75** (2012).

[12] L. Fu and C. L. Kane, "Superconducting Proximity Effect and Majorana Fermions at the Surface of a Topological Insulator", Phys. Rev. Lett. **100**, 96407 (2008).

[13] A. Kitaev, "Fault-tolerant quantum computation by anyons", Annals of Physics **303**, 2–30 (2003).

[14] C. Nayak, S. H. Simon, A. Stern, M. Freedman, and S. Das Sarma, "Non-Abelian anyons and topological quantum computation", Rev. Mod. Phys. **80**, 1083–1159 (2008).

[15] S. Nadj-Perge, I. K. Drozdov, J. Li, H. Chen, S. Jeon, J. Seo, A. H. MacDonald, B. A. Bernevig, and A. Yazdani, "Observation of Majorana fermions in ferromagnetic atomic chains on a superconductor", Science **346**, 602–607 (2014).

[16] Q. L. He, L. Pan, A. L. Stern, E. C. Burks, X. Che, G. Yin, J. Wang, B. Lian, Q. Zhou, E. S. Choi, K. Murata, X. Kou, Z. Chen, T. Nie, Q. Shao, Y. Fan, S.-C. Zhang, K. Liu, J. Xia, and K. L. Wang, "RETRACTED: Chiral Majorana fermion modes in a quantum anomalous Hall insulator–superconductor structure", Science **357**, 294–299 (2017).

[17] L. Fu and C. L. Kane, "Superconducting Proximity Effect and Majorana Fermions at the Surface of a Topological Insulator", Phys. Rev. Lett. **100**, 96407 (2008).

[18] E. Prada, P. San-Jose, M. W. A. de Moor, A. Geresdi, E. J. H. Lee, J. Klinovaja, D. Loss, J. Nygård, R. Aguado, and L. P. Kouwenhoven, "From Andreev to Majorana bound states in hybrid superconductor–semiconductor nanowires", Nature Reviews Physics **2**, 575–594 (2020).

[19] R. S. Deacon, J Wiedenmann, E Bocquillon, F Domínguez, T. M. Klapwijk, P Leubner, C Brüne, E. M. Hankiewicz, S Tarucha, K Ishibashi, H Buhmann, and L. W. Molenkamp, "Josephson Radiation from Gapless Andreev Bound States in HgTe-Based Topological Junctions", Physical Review X **021011**, 1–7 (2017).

[20] M. Kayyalha, D. Xiao, R. Zhang, J. Shin, J. Jiang, F. Wang, Y.-F. Zhao, R. Xiao, L. Zhang, K. M. Fijalkowski, P. Mandal, M. Winnerlein, C. Gould, Q. Li, L. W. Molenkamp, M. H. W. Chan, N. Samarth, and C.-Z. Chang, "Absence of evidence for chiral Majorana modes in quantum anomalous Hall-superconductor devices", Science **367**, 64–67 (2020).

[21] M. Valentini, F. Peñaranda, A. Hofmann, M. Brauns, R. Hauschild, P. Krogstrup, P. San-Jose, E. Prada, R. Aguado, and G. Katsaros, "Nontopological zero-bias peaks in full-shell nanowires induced by flux-tunable Andreev states", Science **373**, 82–88 (2021).

[22] S. Frolov, "Quantum computing's reproducibility crisis: Majorana fermions", Nature **592**, 350–352 (2021).

[23] H. Peng, K. Lai, D. Kong, S. Meister, Y. Chen, X.-L. Qi, S.-C. Zhang, Z.-X. Shen, and Y. Cui, "Aharonov-Bohm interference in topological insulator nanoribbons", Nature Materials **9**, 225–229 (2010).

[24] S. S. Hong, Y. Zhang, J. J. Cha, X.-L. Qi, and Y. Cui, "One-Dimensional Helical Transport in Topological Insulator Nanowire Interferometers", Nano Letters **14**, 2815–2821 (2014).

[25] L. A. Jauregui, M. T. Pettes, L. P. Rokhinson, L. Shi, and Y. P. Chen, "Magnetic field-induced helical mode and topological transitions in a topological insulator nanoribbon", Nature Nanotechnology **11**, 345–351 (2016).

[26] F. Münning, O. Breunig, H. F. Legg, S. Roitsch, D. Fan, M. Rößler, A. Rosch, and Y. Ando, "Quantum confinement of the Dirac surface states in topological-insulator nanowires", Nat. Commun. **12**, 1–6 (2021).

[27] P. Liu, J. R. Williams, and J. J. Cha, "Topological nanomaterials", Nature Reviews Materials **4**, 479–496 (2019).

[28] S. Cho, B. Dellabetta, R. Zhong, J. Schneeloch, T. Liu, G. Gu, M. J. Gilbert, and N. Mason, "Aharonov-Bohm oscillations in a quasi-ballistic three-dimensional topological insulator nanowire", Nature Communications **6**, 1–5 (2015).

[29] S. Cho, R. Zhong, J. A. Schneeloch, G. Gu, and N. Mason, "Kondo-like zero-bias conductance anomaly in a three-dimensional topological insulator nanowire", Scientific Reports **6**, 21767 (2016).

[30] M. Bai, X.-K. Wei, J. Feng, M. Luysberg, A. Bliesener, G. Lippertz, A. Uday, A. A. Taskin, J. Mayer, and Y. Ando, "Proximity-induced superconductivity in $(\mathrm{Bi}_{1-x}\mathrm{Sb}_x)_2\mathrm{Te}_3$ topological-insulator nanowires", Communications Materials **3**, 20 (2022).

[31] J. Kölzer, D. Rosenbach, C. Weyrich, T. W. Schmitt, M. Schleenvoigt, A. R. Jalil, P. Schüffelgen, G. Mussler, V. E. S. IV, D. Grützmacher, H. Lüth, and T. Schäpers, "Phase-coherent loops in selectively-grown topological insulator nanoribbons", Nanotechnology **31**, 325001 (2020).

[32] D. Rosenbach, N. Oellers, A. R. Jalil, M. Mikulics, J. Kölzer, E. Zimmermann, G. Mussler, S. Bunte, D. Grützmacher, H. Lüth, and T. Schäpers, "Quantum Transport in Topological Surface States of Selectively Grown Bi_2Te_3 Nanoribbons", Advanced Electronic Materials **6**, 2000205 (2020).

[33] J. Ziegler, R. Kozlovsky, C. Gorini, M.-H. Liu, S. Weishäupl, H. Maier, R. Fischer, D. A. Kozlov, Z. D. Kvon, N Mikhailov, and Others, "Probing spin helical surface states in topological HgTe nanowires", Phy. Rev. B **97**, 35157 (2018).

[34] R. Fischer, J. Picó-Cortés, W. Himmler, G. Platero, M. Grifoni, D. A. Kozlov, N. N. Mikhailov, S. A. Dvoretsky, C. Strunk, and D. Weiss, "4π-periodic supercurrent tuned by an axial magnetic flux in topological insulator nanowires", Phys. Rev. Research **4**, 13087 (2022).

[35] J Wiedenmann, E Bocquillon, R. S. Deacon, S Hartinger, O Herrmann, T. M. Klapwijk, L Maier, C Gould, A Oiwa, K Ishibashi, S Tarucha, H Buhmann, L. W. Molenkamp, C Ames, and C Bru, "4π-periodic Josephson supercurrent in HgTe-based topological Josephson junctions", Nature Communications **7**, 1–7 (2016).

[36] E. Bocquillon, R. S. Deacon, J. Wiedenmann, P. Leubner, T. M. Klapwijk, C. Brüne, K. Ishibashi, H. Buhmann, and L. W. Molenkamp, "Gapless Andreev bound states in the quantum spin Hall insulator HgTe", Nature Nanotechnology **12**, 137–143 (2017).

[37] P. Schüffelgen, D. Rosenbach, C. Li, T. W. Schmitt, M. Schleenvoigt, A. R. Jalil, S. Schmitt, J. Kölzer, M. Wang, B. Bennemann, U. Parlak, L. Kibkalo, S. Trellenkamp, T. Grap, D. Meertens, M. Luysberg, G. Mussler, E. Berenschot, N. Tas, A. A. Golubov, A. Brinkman, T. Schäpers, and D. Grützmacher, "Selective area growth and stencil lithography for in situ fabricated quantum devices", Nature Nanotechnology **14**, 825–831 (2019).

[38] K. Le Calvez, L. Veyrat, F. Gay, P. Plaindoux, C. B. Winkelmann, H. Courtois, and B. Sacépé, "Joule overheating poisons the fractional ac Josephson effect in topological Josephson junctions", Communications Physics **2**, 4 (2019).

[39] B. de Ronde, C. Li, Y. Huang, and A. Brinkman, "Induced Topological Superconductivity in a $BiSbTeSe_2$-Based Josephson Junction", Nanomaterials **10**, 794 (2020).

[40] D. Rosenbach, T. W. Schmitt, P. Schüffelgen, M. P. Stehno, C. Li, M. Schleenvoigt, A. R. Jalil, G. Mussler, E. Neumann, S. Trellenkamp, A. A. Golubov, A. Brinkman, D. Grützmacher, and T. Schäpers, "Reappearance of first Shapiro step in narrow topological Josephson junctions", Science Advances **7**, eabf1854 (2021).

[41] E. Bocquillon, J. Wiedenmann, R. S. Deacon, T. M. Klapwijk, H. Buhmann, and L. W. Molenkamp, "Microwave Studies of the Fractional Josephson Effect in HgTe-Based Josephson Junctions", in *Topological matter: lectures from the topological matter school 2017* (Springer International Publishing, Cham, 2018), pp. 115–148.

[42] P. Schüffelgen, D. Rosenbach, C. Li, T. Schmitt, M. Schleenvoigt, A. R. Jalil, J. Kölzer, M. Wang, B. Bennemann, U. Parlak, L. Kibkalo, M. Luysberg, G. Mussler, A. A. Golubov, A. Brinkman, T. Schäpers, and D. Grützmacher, "Boosting Transparency in Topological Josephson Junctions via Stencil Lithography", arXiv:1711.01665 (2018).

[43] S. M. Zhang, P. and Mudi, S. and Pendharkar, M. and Lee, J. S. and Dempsey, C. P. and McFadden, A. P. and Harrington, S. D. and Dong, J. T. and Wu, H. and Chen, A. -H. and Hocevar, M. and Palmstrøm, C. J. and Frolov, "Missing odd-order Shapiro steps do not uniquely indicate fractional Josephson effect", arXiv:2211.08710 (2023).

[44] B. H. Elfeky, J. J. Cuozzo, N. Lotfizadeh, W. F. Schiela, S. M. Farzaneh, W. M. Strickland, D. Langone, E. Rossi, and J. Shabani, "Evolution of 4π-Periodic Supercurrent in the Presence of an In-Plane Magnetic Field", ACS Nano **17**, 4650–4658 (2023).

[45] Y. Ando, "Topological insulator materials", Journal of the Physical Society of Japan **82**, 1–32 (2013).

[46] M. Z. Hasan and C. L. Kane, "Colloquium: Topological insulators", Reviews of Modern Physics **82**, 3045–3067 (2010).

[47] X. L. Qi and S. C. Zhang, "Topological insulators and superconductors", Reviews of Modern Physics **83** (2011).

[48] C. Beenakker, "Search for Majorana Fermions in Superconductors", Annual Review of Condensed Matter Physics **4**, 113–136 (2013).

[49] M. Sato and Y. Ando, "Topological superconductors: a review", Reports on Progress in Physics **80**, 76501 (2017).

[50] M. Tinkham and J. C. Wheatley, "Introduction to Superconductivity", Physics Today **29**, 57 (1976).

[51] R. Gross, A. Marx, and F. Deppe, *Applied superconductivity: Josephson effect and superconducting electronics* (De Gruyter, 2016).

[52] K. v. Klitzing, G Dorda, and M Pepper, "New Method for High-Accuracy Determination of the Fine-Structure Constant Based on Quantized Hall Resistance", Phys. Rev. Lett. **45**, 494–497 (1980).

[53] R. B. Laughlin, "Quantized Hall conductivity in two dimensions", Phys. Rev. B **23**, 5632–5633 (1981).

[54] D. J. Thouless, M. Kohmoto, M. P. Nightingale, and M. den Nijs, "Quantized Hall Conductance in a Two-Dimensional Periodic Potential", Phys. Rev. Lett. **49**, 405–408 (1982).

[55] C. L. Kane, "Chapter 1 - Topological Band Theory and the Z_2 Invariant", in *Topological insulators*, Vol. 6, edited by M. Franz and L. Molenkamp, Contemporary Concepts of Condensed Matter Science (Elsevier, 2013), pp. 3–34.

[56] C.-K. Chiu, J. C. Y. Teo, A. P. Schnyder, and S. Ryu, "Classification of topological quantum matter with symmetries", Rev. Mod. Phys. **88**, 35005 (2016).

[57] M. V. Berry, "Quantal phase factors accompanying adiabatic changes", Proceedings of the Royal Society of London. A. Mathematical and Physical Sciences **392**, 45–57 (1984).

[58] J. C. Solem and L. C. Biedenharn, "Understanding geometrical phases in quantum mechanics: An elementary example", Foundations of Physics **23**, 185–195 (1993).

[59] C. L. Kane and E. J. Mele, "Quantum Spin Hall Effect in Graphene", Phys. Rev. Lett. **95**, 226801 (2005).

[60] C. L. Kane and E. J. Mele, "Z_2 Topological Order and the Quantum Spin Hall Effect", Phys. Rev. Lett. **95**, 146802 (2005).

[61] B. A. Bernevig and S.-C. Zhang, "Quantum Spin Hall Effect", Phys. Rev. Lett. **96**, 106802 (2006).

[62] B. A. Bernevig, T. L. Hughes, and S.-C. Zhang, "Quantum Spin Hall Effect and Topological Phase Transition in HgTe Quantum Wells", Science **314**, 1757–1761 (2006).

[63] M. König, S. Wiedmann, C. Brüne, A. Roth, H. Buhmann, L. W. Molenkamp, X.-L. Qi, and S.-C. Zhang, "Quantum Spin Hall Insulator State in HgTe Quantum Wells", Science **318**, 766–770 (2007).

[64] F. Schindler, A. M. Cook, M. G. Vergniory, Z. Wang, S. S. P. Parkin, B. A. Bernevig, and T. Neupert, "Higher-order topological insulators", Science Advances **4**, eaat0346 (2018).

[65] M. C. Rechtsman, J. M. Zeuner, Y. Plotnik, Y. Lumer, D. Podolsky, F. Dreisow, S. Nolte, M. Segev, and A. Szameit, "Photonic Floquet topological insulators", Nature **496**, 196–200 (2013).

[66] M Hafezi, S Mittal, J Fan, A Migdall, and J. M. Taylor, "Imaging topological edge states in silicon photonics", Nature Photonics **7**, 1001–1005 (2013).

[67] M. A. Bandres, S. Wittek, G. Harari, M. Parto, J. Ren, M. Segev, D. N. Christodoulides, and M. Khajavikhan, "Topological insulator laser: Experiments", Science **359**, eaar4005 (2018).

[68] F. D. M. Haldane and S Raghu, "Possible Realization of Directional Optical Waveguides in Photonic Crystals with Broken Time-Reversal Symmetry", Phys. Rev. Lett. **100**, 13904 (2008).

[69] J. Ningyuan, C. Owens, A. Sommer, D. Schuster, and J. Simon, "Time- and Site-Resolved Dynamics in a Topological Circuit", Phys. Rev. X **5**, 21031 (2015).

[70] G. Jotzu, M. Messer, R. Desbuquois, M. Lebrat, T. Uehlinger, D. Greif, and T. Esslinger, "Experimental realization of the topological Haldane model with ultracold fermions", Nature **515**, 237–240 (2014).

[71] M Aidelsburger, M Lohse, C Schweizer, M Atala, J. T. Barreiro, S Nascimbène, N. R. Cooper, I Bloch, and N Goldman, "Measuring the Chern number of Hofstadter bands with ultracold bosonic atoms", Nature Physics **11**, 162–166 (2015).

[72] R. Fleury, A. B. Khanikaev, and A. Alù, "Floquet topological insulators for sound", Nature Communications **7**, 11744 (2016).

[73] R. Süsstrunk and S. D. Huber, "Observation of phononic helical edge states in a mechanical topological insulator", Science **349**, 47–50 (2015).

[74] Y. L. Chen, J. G. Analytis, J.-H. Chu, Z. K. Liu, S.-K. Mo, X. L. Qi, H. J. Zhang, D. H. Lu, X Dai, Z Fang, S. C. Zhang, I. R. Fisher, Z Hussain, and Z.-X. Shen, "Experimental Realization of a Three-Dimensional Topological Insulator, Bi_2Te_3", Science **325**, 178–181 (2009).

[75] J. H. Davies, *The physics of low-dimensional semiconductors: an introduction* (Cambridge University Press, 1997).

[76] A. K. Geim and K. S. Novoselov, "The rise of graphene", Nature Materials **6**, 183–191 (2007).

[77] A. Chatterjee, P. Stevenson, S. De Franceschi, A. Morello, N. P. de Leon, and F. Kuemmeth, "Semiconductor qubits in practice", Nature Reviews Physics **3**, 157–177 (2021).

[78] R. A. Webb, S Washburn, C. P. Umbach, and R. B. Laibowitz, "Observation of $\frac{h}{e}$ Aharonov-Bohm Oscillations in Normal-Metal Rings", Phys. Rev. Lett. **54**, 2696–2699 (1985).

[79] A. Bachtold, C. Strunk, J.-P. Salvetat, J.-M. Bonard, L. Forró, T. Nussbaumer, and C. Schönenberger, "Aharonov–Bohm oscillations in carbon nanotubes", Nature **397**, 673–675 (1999).

[80] Y. Zhang, K. He, C.-Z. Chang, C.-L. Song, L.-L. Wang, X. Chen, J.-F. Jia, Z. Fang, X. Dai, W.-Y. Shan, S.-Q. Shen, Q. Niu, X.-L. Qi, S.-C. Zhang, X.-C. Ma, and Q.-K. Xue, "Crossover of the three-dimensional topological insulator Bi2Se3 to the two-dimensional limit", Nature Physics **6**, 584–588 (2010).

[81] J. H. Bardarson, P. W. Brouwer, and J. E. Moore, "Aharonov-Bohm Oscillations in Disordered Topological Insulator Nanowires", Physical Review Letters **105**, 156803 (2010).

[82] J. H. Bardarson and J. E. Moore, "Quantum interference and Aharonov–Bohm oscillations in topological insulators", Reports on Progress in Physics **76**, 56501 (2013).

[83] F. de Juan, J. H. Bardarson, and R. Ilan, "Conditions for fully gapped topological superconductivity in topological insulator nanowires", SciPost Phys. **6**, 60 (2019).

[84] H. F. Legg, D. Loss, and J. Klinovaja, "Majorana bound states in topological insulators without a vortex", Phys. Rev. B **104**, 165405 (2021).

[85] A. M. Cook, M. M. Vazifeh, and M. Franz, "Stability of Majorana fermions in proximity-coupled topological insulator nanowires", Physical Review B - Condensed Matter and Materials Physics **86**, 1–17 (2012).

[86] M. Atzori, C. Train, E. A. Hillard, N. Avarvari, and G. L. J. A. Rikken, "Magneto-chiral anisotropy: From fundamentals to perspectives", Chirality **33**, 844–857 (2021).

[87] G. L. J. A. Rikken, J Fölling, and P Wyder, "Electrical Magnetochiral Anisotropy", Phys. Rev. Lett. **87**, 236602 (2001).

[88] G. L. J. A. Rikken and P Wyder, "Magnetoelectric Anisotropy in Diffusive Transport", Phys. Rev. Lett. **94**, 16601 (2005).

[89] Y. Tokura and N. Nagaosa, "Nonreciprocal responses from non-centrosymmetric quantum materials", Nat. Commun. **9**, 3740 (2018).

[90] P. He, S. S. L. Zhang, D. Zhu, Y. Liu, Y. Wang, J. Yu, G. Vignale, and H. Yang, "Bilinear magnetoelectric resistance as a probe of three-dimensional spin texture in topological surface states", Nat. Phys. **14**, 495–499 (2018).

[91] T. Morimoto and N. Nagaosa, "Chiral anomaly and giant magnetochiral anisotropy in noncentrosymmetric Weyl semimetals", Phys. Rev. Lett. **117**, 146603 (2016).

[92] T Ideue, K Hamamoto, S Koshikawa, M Ezawa, S Shimizu, Y Kaneko, Y Tokura, N Nagaosa, and Y Iwasa, "Bulk rectification effect in a polar semiconductor", Nat. Phys. **13**, 578–583 (2017).

[93] G. L. J. A. Rikken and N Avarvari, "Strong electrical magnetochiral anisotropy in tellurium", Phys. Rev. B **99**, 245153 (2019).

[94] Y. Wang, H. F. Legg, T. Boemerich, J. Park, A. A. Taskin, A. Rosch, and Y. Ando, "Gigantic magnetochiral anisotropy in the topological semimetal $ZrTe_5$", arXiv:2011.03329 (2020).

[95] G. Eilenberger, "Transformation of Gorkov's equation for type II superconductors into transport-like equations", Zeitschrift für Physik A Hadrons and nuclei **214**, 195–213 (1968).

[96] G Seidel and P. H. Keesom, "Specific Heat of Gallium and Zinc in the Normal and Superconducting States", Phys. Rev. **112**, 1083–1088 (1958).

[97] N. E. Phillips, "Low-Temperature Heat Capacities of Gallium, Cadmium, and Copper", Phys. Rev. **134**, A385–A391 (1964).

[98] W Meissner and R Ochsenfeld, "Ein neuer Effekt bei Eintritt der Supraleitfähigkeit", Naturwissenschaften **21**, 787–788 (1933).

[99] F London, H London, and F. A. Lindemann, "The electromagnetic equations of the supraconductor", Proceedings of the Royal Society of London. Series A - Mathematical and Physical Sciences **149**, 71–88 (1935).

[100] J Bardeen, L. N. Cooper, and J. R. Schrieffer, "Microscopic Theory of Superconductivity", Phys. Rev. **106**, 162–164 (1957).

[101] J Bardeen, L. N. Cooper, and J. R. Schrieffer, "Theory of Superconductivity", Phys. Rev. **108**, 1175–1204 (1957).

[102] P.-G. De Gennes, *Superconductivity of metals and alloys* (CRC press, 1966).

[103] G. E. Blonder, M Tinkham, and T. M. Klapwijk, "Transition from metallic to tunneling regimes in superconducting microconstrictions: Excess current, charge imbalance, and supercurrent conversion", Phys. Rev. B **25**, 4515–4532 (1982).

[104] T. M. Klapwijk, G. E. Blonder, and M Tinkham, "Explanation of subharmonic energy gap structure in superconducting contacts", Physica B+C **109-110**, 1657–1664 (1982).

[105] M Bode, "Spin-polarized scanning tunnelling microscopy", Rep. Prog. Phys. **66**, 523–582 (2003).

[106] T. M. Klapwijk, "Proximity Effect From an Andreev Perspective", Journal of Superconductivity **17**, 593–611 (2004).

[107] M Octavio, M Tinkham, G. E. Blonder, and T. M. Klapwijk, "Subharmonic energy-gap structure in superconducting constrictions", Phys. Rev. B **27**, 6739–6746 (1983).

[108] S. Ghatak, O. Breunig, F. Yang, Z. Wang, A. A. Taskin, and Y. Ando, "Anomalous Fraunhofer patterns in gated Josephson junctions based on the bulk-insulating topological insulator $BiSbTeSe_2$", Nano Letters **18**, 5124–5131 (2018).

[109] J T Edwards and D J Thouless, "Numerical studies of localization in disordered systems", Journal of Physics C: Solid State Physics **5**, 807 (1972).

[110] A. Altland, Y. Gefen, and G. Montambaux, "What is the Thouless Energy for Ballistic Systems?", Phys. Rev. Lett. **76**, 1130–1133 (1996).

[111] P Dubos, H Courtois, B Pannetier, F. K. Wilhelm, A. D. Zaikin, and G Schön, "Josephson critical current in a long mesoscopic S-N-S junction", Phys. Rev. B **63**, 64502 (2001).

[112] G Tkachov and E. M. Hankiewicz, "Helical Andreev bound states and superconducting Klein tunneling in topological insulator Josephson junctions", Phys. Rev. B **88**, 75401 (2013).

[113] H.-J. Kwon, V. M. Yakovenko, and K Sengupta, "Fractional ac Josephson effect in unconventional superconductors", Low Temperature Physics **30**, 613–619 (2004).

[114] L. Fu and C. L. Kane, "Josephson current and noise at a superconductor / quantum-spin-Hall-insulator / superconductor junction", Phys. Rev. B **79**, 161408 (2009).

[115] R. Ilan, J. H. Bardarson, H.-S. Sim, and J. E. Moore, "Detecting perfect transmission in Josephson junctions on the surface of three dimensional topological insulators", New Journal of Physics **16**, 053007 (2014).

[116] B. D. Josephson, "Possible new effects in superconductive tunnelling", Physics Letters **1**, 251–253 (1962).

[117] B. D. Josephson, "The discovery of tunnelling supercurrents", Rev. Mod. Phys. **46**, 251–254 (1974).

[118] S. Shapiro, "Josephson Currents in Superconducting Tunneling: The Effect of Microwaves and Other Observations", Phys. Rev. Lett. **11**, 80–82 (1963).

[119] F Dominguez, O Kashuba, E Bocquillon, J Wiedenmann, R. S. Deacon, T. M. Klapwijk, G Platero, L. W. Molenkamp, B Trauzettel, and E. M. Hankiewicz, "Josephson junction dynamics in the presence of 2π- and 4π-periodic supercurrents", Phys. Rev. B **95**, 195430 (2017).

[120] H Kamata, R. S. Deacon, S Matsuo, K Li, S Jeppesen, L Samuelson, H. Q. Xu, K Ishibashi, and S Tarucha, "Anomalous modulation of Josephson radiation in nanowire-based Josephson junctions", Phys. Rev. B **98**, 41302 (2018).

[121] L. P. Rokhinson, X. Liu, and J. K. Furdyna, "The fractional a.c. Josephson effect in a semiconductor-superconductor nanowire as a signature of Majorana particles", Nature Physics **8**, 795–799 (2012).

[122] C. Li, J. C. D. Boer, B. D. Ronde, S. V. Ramankutty, E. V. Heumen, Y. Huang, A. D. Visser, A. A. Golubov, M. S. Golden, and A. Brinkman, "4π-periodic Andreev bound states in a Dirac semimetal", Nature Materials **17** (2018).

[123] J. Picó-Cortés, F. Dominguez, and G. Platero, "Signatures of a 4π-periodic supercurrent in the voltage response of capacitively shunted topological Josephson junctions", Phys. Rev. B **96**, 125438 (2017).

[124] D. Rainis and D. Loss, "Majorana qubit decoherence by quasiparticle poisoning", Phys. Rev. B **85**, 174533 (2012).

[125] A. E. Svetogorov, D. Loss, and J. Klinovaja, "Quasiparticle poisoning in trivial and topological Josephson junctions", Phys. Rev. B **105**, 174519 (2022).

[126] P. J. de Visser, J. J. A. Baselmans, P Diener, S. J. C. Yates, A Endo, and T. M. Klapwijk, "Number Fluctuations of Sparse Quasiparticles in a Superconductor", Phys. Rev. Lett. **106**, 167004 (2011).

[127] S. M. Albrecht, E. B. Hansen, A. P. Higginbotham, F Kuemmeth, T. S. Jespersen, J Nygård, P Krogstrup, J Danon, K Flensberg, and C. M. Marcus, "Transport Signatures of Quasiparticle Poisoning in a Majorana Island", Phys. Rev. Lett. **118**, 137701 (2017).

[128] M Snelder, M Veldhorst, A. A. Golubov, and A Brinkman, "Andreev bound states and current-phase relations in three-dimensional topological insulators", Phys. Rev. B **87**, 104507 (2013).

[129] Y. Takeshige, S. Matsuo, R. S. Deacon, K. Ueda, Y. Sato, Y.-F. Zhao, L. Zhou, C.-Z. Chang, K. Ishibashi, and S. Tarucha, "Experimental study of ac Josephson effect in gate-tunable $(\mathrm{Bi}_{1-x}\mathrm{Sb}_x)_2\mathrm{Te}_3$ thin-film Josephson junctions", Phys. Rev. B **101**, 115410 (2020).

[130] A De Cecco, K Le Calvez, B Sacépé, C. B. Winkelmann, and H Courtois, "Interplay between electron overheating and ac Josephson effect", Phys. Rev. B **93**, 180505 (2016).

[131] M. C. Dartiailh, J. J. Cuozzo, B. H. Elfeky, W. Mayer, J. Yuan, K. S. Wickramasinghe, E. Rossi, and J. Shabani, "Missing Shapiro steps in topologically trivial Josephson junction on InAs quantum well", Nature Communications **12**, 78 (2021).

[132] N. Argaman, "Nonequilibrium Josephson-like effects in wide mesoscopic SNS junctions", Superlattices and Microstructures **25**, 861–875 (1999).

[133] C.-K. Chiu and S Das Sarma, "Fractional Josephson effect with and without Majorana zero modes", Phys. Rev. B **99**, 35312 (2019).

[134] A. C. Potter and L. Fu, "Anomalous supercurrent from Majorana states in topological insulator Josephson junctions", Phys. Rev. B **88**, 121109 (2013).

[135] B Baxevanis, V. P. Ostroukh, and C. W. J. Beenakker, "Even-odd flux quanta effect in the Fraunhofer oscillations of an edge-channel Josephson junction", Phys. Rev. B **91**, 41409 (2015).

[136] S. Hart, H. Ren, M. Kosowsky, G. Ben-Shach, P. Leubner, C. Brüne, H. Buhmann, L. W. Molenkamp, B. I. Halperin, and A. Yacoby, "Controlled finite momentum pairing and spatially varying order parameter in proximitized HgTe quantum wells", Nature Physics **13**, 87–93 (2017).

[137] A. Q. Chen, M. J. Park, S. T. Gill, Y. Xiao, D. Reig-i Plessis, G. J. MacDougall, M. J. Gilbert, and N. Mason, "Finite momentum Cooper pairing in three-dimensional topological insulator Josephson junctions", Nature Communications **9**, 3478 (2018).

[138] H. F. Legg, K. Laubscher, D. Loss, and J. Klinovaja, "Parity protected superconducting diode effect in topological Josephson junctions", arXiv:2301.13740 (2023).

[139] B. Pal, A. Chakraborty, P. K. Sivakumar, M. Davydova, A. K. Gopi, A. K. Pandeya, J. A. Krieger, Y. Zhang, M. Date, S. Ju, N. Yuan, N. B. M. Schröter, L. Fu, and S. S. P. Parkin, "Josephson diode effect from Cooper pair momentum in a topological semimetal", Nature Physics **18**, 1228–1233 (2022).

[140] L. Fu and C. L. Kane, "Topological insulators with inversion symmetry", Physical Review B - Condensed Matter and Materials Physics **76**, 1–17 (2007).

[141] D Hsieh, D Qian, L Wray, Y Xia, Y. S. Hor, R. J. Cava, and M. Z. Hasan, "A topological Dirac insulator in a quantum spin Hall phase", Nature **452**, 970–974 (2008).

[142] H. Zhang, C.-X. Liu, X.-L. Qi, X. Dai, Z. Fang, and S.-C. Zhang, "Topological insulators in $\mathrm{Bi_2Se_3}$, $\mathrm{Bi_2Te_3}$ and $\mathrm{Sb_2Te_3}$ with a single Dirac cone on the surface", Nature Physics **5**, 438–442 (2009).

[143] C.-X. Liu, X.-L. Qi, H. Zhang, X. Dai, Z. Fang, and S.-C. Zhang, "Model Hamiltonian for topological insulators", Phys. Rev. B **82**, 45122 (2010).

[144] J. Zhang, C.-Z. Chang, Z. Zhang, J. Wen, X. Feng, K. Li, M. Liu, K. He, L. Wang, X. Chen, Q.-K. Xue, X. Ma, and Y. Wang, "Band structure engineering in $\mathrm{(Bi_{1-x}Sb_x)_2Te_3}$ ternary topological insulators", Nature Communications **2**, 574 (2011).

[145] D. Kong, J. J. Cha, K. Lai, H. Peng, J. G. Analytis, S. Meister, Y. Chen, H. J. Zhang, I. R. Fisher, Z. X. Shen, and Y. Cui, "Rapid Surface Oxidation as a Source of Surface Degradation Factor for $\mathrm{Bi_2Se_3}$", ACS Nano **5**, 4698–4703 (2011).

[146] Z. Alpichshev, J. G. Analytis, J.-H. Chu, I. R. Fisher, Y. L. Chen, Z. X. Shen, A Fang, and A Kapitulnik, "STM Imaging of Electronic Waves on the Surface of Bi_2Te_3: Topologically Protected Surface States and Hexagonal Warping Effects", Phys. Rev. Lett. **104**, 16401 (2010).

[147] L. Fu, "Hexagonal Warping Effects in the Surface States of the Topological Insulator Bi_2Te_3", Phys. Rev. Lett. **103**, 266801 (2009).

[148] A. Bliesener, "Molecular Beam Epitaxy Growth of Topological Materials", PhD thesis (Universität zu Köln, 2020).

[149] D. Kong, Y. Chen, J. J. Cha, Q. Zhang, J. G. Analytis, K. Lai, Z. Liu, S. S. Hong, K. J. Koski, S.-K. Mo, Z. Hussain, I. R. Fisher, Z.-X. Shen, and Y. Cui, "Ambipolar field effect in the ternary topological insulator $(Bi_{1-x}Sb_x)_2Te_3$ by composition tuning", Nature Nanotechnology **6**, 705–709 (2011).

[150] L. He, X. Kou, and K. L. Wang, "Review of 3D topological insulator thin-film growth by molecular beam epitaxy and potential applications", physica status solidi (RRL) – Rapid Research Letters **7**, 50–63 (2013).

[151] A. A. Taskin, Z. Ren, S. Sasaki, K. Segawa, and Y. Ando, "Observation of dirac holes and electrons in a topological insulator", Physical Review Letters **107**, 1–4 (2011).

[152] B. Skinner, T. Chen, and B. I. Shklovskii, "Why Is the Bulk Resistivity of Topological Insulators So Small?", Phys. Rev. Lett. **109**, 176801 (2012).

[153] B Skinner, T Chen, and B. I. Shklovskii, "Effects of bulk charged impurities on the bulk and surface transport in three-dimensional topological insulators", Journal of Experimental and Theoretical Physics **117**, 579–592 (2013).

[154] Y. Huang and B. I. Shklovskii, "Disorder effects in topological insulator nanowires", Physical Review B **104**, 1–7 (2021).

[155] B. I. Shklovskii and A. L. Efros, *Electronic Properties of Doped Semiconductors*, 1st ed. (Springer-Verlag Berlin Heidelberg 1984, 1984).

[156] B. I. Shklovskii, "Simple model of Coulomb disorder and screening in graphene", Phys. Rev. B **76**, 233411 (2007).

[157] J Martin, N Akerman, G Ulbricht, T Lohmann, J. H. Smet, K von Klitzing, and A Yacoby, "Observation of electron-hole puddles in graphene using a scanning single-electron transistor", Nature Physics **4**, 144–148 (2008).

[158] F Amet, J. R. Williams, A. G. F. Garcia, M Yankowitz, K Watanabe, T Taniguchi, and D Goldhaber-Gordon, "Tunneling spectroscopy of graphene-boron-nitride heterostructures", Phys. Rev. B **85**, 73405 (2012).

[159] S Samaddar, I Yudhistira, S Adam, H Courtois, and C. B. Winkelmann, "Charge Puddles in Graphene near the Dirac Point", Phys. Rev. Lett. **116**, 126804 (2016).

[160] Y. Huang and B. I. Shklovskii, "Disorder effects in topological insulator thin films", Physical Review B **103**, 165409 (2021).

[161] H. Beidenkopf, P. Roushan, J. Seo, L. Gorman, I. Drozdov, Y. S. Hor, R. J. Cava, and A. Yazdani, "Spatial fluctuations of helical Dirac fermions on the surface of topological insulators", Nature Physics **7**, 939–943 (2011).

[162] N Borgwardt, J Lux, I Vergara, Z. Wang, A. A. Taskin, K. Segawa, P. H. M. van Loosdrecht, Y. Ando, A Rosch, and M Grüninger, "Self-organized charge puddles in a three-dimensional topological material", Phys. Rev. B **93**, 245149 (2016).

[163] M. Bagchi, L. Pitz-Paal, C. P. Grams, O. Breunig, N. Borgwardt, Z. Wang, Y. Ando, M. Grüninger, and J. Hemberger, "Large positive magnetoconductivity at microwave frequencies in the compensated topological insulator $BiSbTeSe_2$", Phys. Rev. B **99**, 161121 (2019).

[164] T Knispel, W Jolie, N Borgwardt, J Lux, Z. Wang, Y. Ando, A Rosch, T Michely, and M Grüninger, "Charge puddles in the bulk and on the surface of the topological insulator BiSbTeSe 2 studied by scanning tunneling microscopy and optical spectroscopy", Phys. Rev. B **96**, 195135 (2017).

[165] T. Bömerich, J. Lux, Q. T. Feng, and A. Rosch, "Length scale of puddle formation in compensation-doped semiconductors and topological insulators", Phys. Rev. B **96**, 75204 (2017).

[166] A. A. Taskin, S. Sasaki, K. Segawa, and Y. Ando, "Achieving surface quantum oscillations in topological insulator thin films of $\mathrm{Bi_2Te_3}$", Advanced Materials **24**, 5581–5585 (2012).

[167] F. Yang, A. A. Taskin, S. Sasaki, K. Segawa, Y. Ohno, K. Matsumoto, and Y. Ando, "Top gating of epitaxial $\mathrm{(Bi_{1-x}Sb_x)_2Te_3}$ topological insulator thin films", Applied Physics Letters **104**, 161614 (2014).

[168] B. F. Gao, P Gehring, M Burghard, and K Kern, "Gate-controlled linear magnetoresistance in thin $\mathrm{Bi_2Se_3}$ sheets", Applied Physics Letters **100** (2012).

[169] Y. Xu, I. Miotkowski, C. Liu, J. Tian, H. Nam, N. Alidoust, J. Hu, C. K. Shih, M. Z. Hasan, and Y. P. Chen, "Observation of topological surface state quantum Hall effect in an intrinsic three-dimensional topological insulator", Nature Physics **10**, 956–963 (2014).

[170] Z. Ren, A. A. Taskin, S. Sasaki, K. Segawa, and Y. Ando, "Large bulk resistivity and surface quantum oscillations in the topological insulator Bi2 Te2 Se", Physical Review B - Condensed Matter and Materials Physics **82**, 1–4 (2010).

[171] T Arakane, T Sato, S Souma, K Kosaka, K Nakayama, M Komatsu, T Takahashi, Z. Ren, K. Segawa, and Y. Ando, "Tunable Dirac cone in the topological insulator $(Bi_{2-x}Sb_xTe_{3-y}Se_y$", Nature Communications **3**, 636 (2012).

[172] A. A. Taskin, S. Sasaki, K. Segawa, and Y. Ando, "Manifestation of Topological Protection in Transport Properties of Epitaxial $\mathrm{Bi_2Se_3}$ Thin Films", Phys. Rev. Lett. **109**, 66803 (2012).

[173] L. Bretheau, J. I.-j. Wang, R. Pisoni, K. Watanabe, and T. Taniguchi, "Tunnelling spectroscopy of Andreev states in graphene", Nature Physics **13**, 756–760 (2017).

[174] N. Zapata, "Fabrication and Characterization of Josephson Junctions on Topological Insulating Nanowires", PhD thesis (University of Cologne, 2021).

[175] A. A. Volykhov, J. Sánchez-Barriga, A. P. Sirotina, V. S. Neudachina, A. S. Frolov, E. A. Gerber, E. Y. Kataev, B. Senkovsky, N. O. Khmelevsky, A. Y. Aksenenko, N. V. Korobova, A. Knop-Gericke, O. Rader, and L. V. Yashina, "Rapid Surface Oxidation of $\mathrm{Sb_2Te_3}$ as Indication for a Universal Trend in the Chemical Reactivity of Tetradymite Topological Insulators", Chemistry of Materials **28**, 8916–8923 (2016).

[176] L. V. Yashina, J. Sánchez-Barriga, M. R. Scholz, A. A. Volykhov, A. P. Sirotina, V. Neudachina S., M. E. Tamm, A. Varykhalov, D. Marchenko, G. Springholz, G. Bauer, A. Knop-Gericke, and O. Rader, "Negligible Surface Reactivity of Topological Insulators $\mathrm{Bi_2Se_3}$ and $\mathrm{Bi_2Te_3}$ towards Oxygen and Water", ACS Nano **7**, 5181–5191 (2013).

[177] M. Brahlek, Y. S. Kim, N. Bansal, E. Edrey, and S. Oh, "Surface versus bulk state in topological insulator $\mathrm{Bi_2Se_3}$ under environmental disorder", Applied Physics Letters **99**, 2009–2012 (2011).

[178] V. A. Golyashov, K. A. Kokh, S. V. Makarenko, K. N. Romanyuk, I. P. Prosvirin, A. V. Kalinkin, O. E. Tereshchenko, A. S. Kozhukhov, D. V. Sheglov, S. V. Eremeev, S. D. Borisova, and E. V. Chulkov, "Inertness and degradation of (0001) surface of Bi_2Se_3 topological insulator", Journal of Applied Physics **112**, 113702 (2012).

[179] H Bando, K Koizumi, Y Oikawa, K Daikohara, V. A. Kulbachinskii, and H Ozaki, "The time-dependent process of oxidation of the surface of Bi_2Te_3 studied by x-ray photoelectron spectroscopy", Journal of Physics: Condensed Matter **12**, 5607–5616 (2000).

[180] J. H. Guo, F. Qiu, Y. Zhang, H. Y. Deng, G. J. Hu, X. N. Li, G. L. Yu, and N. Dai, "Surface oxidation properties in a topological insulator Bi_2Te_3 film", Chinese Physics Letters **30**, 6801 (2013).

[181] A. J. Green, S. Dey, Y. Q. An, B. O'Brien, S. O'Mullane, B. Thiel, and A. C. Diebold, "Surface oxidation of the topological insulator Bi_2Se_3", Journal of Vacuum Science & Technology A **34**, 61403 (2016).

[182] M. T. Edmonds, J. T. Hellerstedt, A. Tadich, A. Schenk, K. M. Odonnell, J. Tosado, N. P. Butch, P. Syers, J. Paglione, and M. S. Fuhrer, "Stability and surface reconstruction of topological insulator Bi_2Se_3 on exposure to atmosphere", Journal of Physical Chemistry C **118**, 20413–20419 (2014).

[183] H.-S. Kim, T.-H. Hwang, N.-H. Kim, Y. Hou, D. Yu, H.-S. Sim, and Y.-J. Doh, "Adjustable Quantum Interference Oscillations in Sb-Doped Bi_2Se_3 Topological Insulator Nanoribbons", ACS Nano **14**, 14118–14125 (2020).

[184] A. A. Volykhov, J. Sa, M. Batuk, C. Callaert, J. Hadermann, A. P. Sirotina, V. S. Neudachina, A. I. Belova, N. V. Vladimirova, and M. E. Tamm, "Can surface reactivity of mixed crystals be predicted from their counterparts? A case study", Journal of Materials Chemistry C **6**, 8941–8949 (2018).

[185] C. R. Thomas, M. K. Vallon, M. G. Frith, H. Sezen, S. K. Kushwaha, R. J. Cava, J. Schwartz, and S. L. Bernasek, "Surface Oxidation of $Bi_2\mathrm{Te}, \mathrm{Se}_3$ Topological Insulators Depends on Cleavage Accuracy", Chemistry of Materials **28**, 35–39 (2016).

[186] R. J. Macedo, S. E. Harrison, T. S. Dorofeeva, J. S. Harris, and R. A. Kiehl, "Nanoscale Probing of Local Electrical Characteristics on MBE-Grown Bi_2Te_3 Surfaces under Ambient Conditions", Nano Letters **15**, 4241–4247 (2015).

[187] K. L. Scipioni, Z. Wang, Y. Maximenko, F. Katmis, C. Steiner, and V. Madhavan, "Role of defects in the carrier-tunable topological-insulator $(Bi_{1-x}Sb_x)_2Te_3$ thin films", Phys. Rev. B **97**, 125150 (2018).

[188] A. Eckmann, A. Felten, A. Mishchenko, L. Britnell, R. Krupke, K. S. Novoselov, and C. Casiraghi, "Probing the Nature of Defects in Graphene by Raman Spectroscopy", Nano Letters **12**, 3925–3930 (2012).

[189] S. J. Pearton, R. J. Shul, and F. Ren, "A Review of Dry Etching of GaN and Related Materials", MRS Internet Journal of Nitride Semiconductor Research **5**, 11 (2000).

[190] R Cheung, Y. H. Lee, C. M. Knoedler, K. Y. Lee, T. P. Smith, and D. P. Kern, "Sidewall damage in n+-GaAs quantum wires from reactive ion etching", Applied Physics Letters **54**, 2130–2132 (1989).

[191] I. Childres, J. Tian, I. Miotkowski, and Y. Chen, "AFM and Raman studies of topological insulator materials subject to argon plasma etching", Philosophical Magazine **93**, 681–689 (2013).

[192] H. Peng, W. Dang, J. Cao, Y. Chen, D. Wu, W. Zheng, H. Li, Z.-X. Shen, and Z. Liu, "Topological insulator nanostructures for near-infrared transparent flexible electrodes", Nature Chemistry **4**, 281–286 (2012).

[193] R. F. Egerton, P Li, and M Malac, "Radiation damage in the TEM and SEM", Micron **35**, 399–409 (2004).

[194] K Kuroda, M Arita, K Miyamoto, M Ye, J Jiang, A Kimura, E. E. Krasovskii, E. V. Chulkov, H Iwasawa, T Okuda, K Shimada, Y Ueda, H Namatame, and M Taniguchi, "Hexagonally Deformed Fermi Surface of the 3D Topological Insulator Bi_2Se_3", Phys. Rev. Lett. **105**, 76802 (2010).

[195] A. Taskin, *Protective capping for $(Bi_{1-x}Sb_x)_2Te_3$ thin-films*, tech. rep. (II. Institute of Physics - University of Cologne, 2020).

[196] P. Stevic, *Kavli Nanolab Delft Equipment - Transene D - Aluminum Etching SOP*, 2018.

[197] M. J. L. Sourribes, I Isakov, M Panfilova, and P. A. Warburton, "Minimization of the contact resistance between InAs nanowires and metallic contacts", Nanotechnology **24**, 45703 (2013).

[198] Ö. Gül, H. Zhang, F. K. de Vries, J. van Veen, K. Zuo, V. Mourik, S. Conesa-Boj, M. P. Nowak, D. J. van Woerkom, M. Quintero-Pérez, M. C. Cassidy, A. Geresdi, S. Koelling, D. Car, S. R. Plissard, E. P. A. M. Bakkers, and L. P. Kouwenhoven, "Hard Superconducting Gap in InSb Nanowires", Nano Letters **17**, 2690–2696 (2017).

[199] H. Zhang, Ö. Gül, S. Conesa-Boj, M. P. Nowak, M. Wimmer, K. Zuo, V. Mourik, F. K. de Vries, J. van Veen, M. W. A. de Moor, J. D. S. Bommer, D. J. van Woerkom, D. Car, S. R. Plissard, E. P. A. M. Bakkers, M. Quintero-Pérez, M. C. Cassidy, S. Koelling, S. Goswami, K. Watanabe, T. Taniguchi, and L. P. Kouwenhoven, "Ballistic superconductivity in semiconductor nanowires", Nature Communications **8**, 16025 (2017).

[200] Ö. Gül, H. Zhang, J. D. Bommer, M. W. De Moor, D. Car, S. R. Plissard, E. P. Bakkers, A. Geresdi, K. Watanabe, T. Taniguchi, and L. P. Kouwenhoven, "Ballistic Majorana nanowire devices", Nature Nanotechnology **13**, 192–197 (2018).

[201] V. E. Calado, S Goswami, G Nanda, M Diez, A. R. Akhmerov, K Watanabe, T Taniguchi, T. M. Klapwijk, and L. M. K. Vandersypen, "Ballistic Josephson junctions in edge-contacted graphene", Nature Nanotechnology **10**, 761–764 (2015).

[202] I. V. Borzenets, F Amet, C. T. Ke, A. W. Draelos, M. T. Wei, A Seredinski, K Watanabe, T Taniguchi, Y Bomze, M Yamamoto, S Tarucha, and G Finkelstein, "Ballistic Graphene Josephson Junctions from the Short to the Long Junction Regimes", Phys. Rev. Lett. **117**, 237002 (2016).

[203] S. Charpentier, L. Galletti, G. Kunakova, R. Arpaia, Y. Song, R. Baghdadi, S. M. Wang, A. Kalaboukhov, E. Olsson, F. Tafuri, D. Golubev, J. Linder, T. Bauch, and F. Lombardi, "Induced unconventional superconductivity on the surface states of Bi2Te3 topological insulator", Nature Communications **8**, 2019 (2017).

[204] T. W. Schmitt, M. R. Connolly, M. Schleenvoigt, C. Liu, O. Kennedy, J. M. Chávez-Garcia, A. R. Jalil, B. Bennemann, S. Trellenkamp, F. Lentz, E. Neumann, T. Lindström, S. E. de Graaf, E. Berenschot, N. Tas, G. Mussler, K. D. Petersson, D. Grützmacher, and P. Schüffelgen, "Integration of Topological Insulator Josephson Junctions in Superconducting Qubit Circuits", Nano Letters **22**, 2595–2602 (2022).

[205] P. Umesh, "Poojitha Umesh PhD Thesis - under preparation", PhD thesis (University of Cologne, 2022).

[206] D. T. Chuss and N. G. S. F. Center, *Cosmic Background Explorer*.

[207] Oxford Instruments, *Principles of dilution refrigeration*, 2022.

[208] G Batey, A. J. Matthews, and M Patton, "A new ultra-low-temperature cryogen-free experimental platform", Journal of Physics: Conference Series **568**, 32014 (2014).

[209] F. Pobell, *Matter and Methods at Low Temperatures* (Springer, 2007).

[210] QDevil, *QDevil Company Website*, 2022.

[211] Zurich Instruments, *Principles of lock-in detection and the state of the art*, 2022.

[212] O. Breunig, "Thermodynamics of the Spin-Chain Compounds Cs2CoCl4 and Cu(C4H4N2)(NO3)2", PhD thesis (University of Cologne, 2015).

[213] Quantum Design, *Physical Property Measurement System (PPMS)*, 2022.

[214] R. M. Lutchyn, E. P. A. M. Bakkers, L. P. Kouwenhoven, P Krogstrup, C. M. Marcus, and Y Oreg, "Majorana zero modes in superconductor–semiconductor heterostructures", Nature Reviews Materials **3**, 52–68 (2018).

[215] M. Aghaee and E. Al., "InAs-Al hybrid devices passing the topological gap protocol", Phys. Rev. B **107**, 245423 (2023).

[216] R Yoshimi, A Tsukazaki, Y Kozuka, J Falson, K. S. Takahashi, J. G. Checkelsky, N Nagaosa, M Kawasaki, and Y Tokura, "Quantum Hall effect on top and bottom surface states of topological insulator $(\mathrm{Bi}_{1-x}\mathrm{Sb}_x)_2\mathrm{Te}_3$ films", Nature Communications **6**, 6627 (2015).

[217] F. Yang, A. A. Taskin, S. Sasaki, K. Segawa, Y. Ohno, and K. Matsumoto, "Dual-Gated Topological Insulator Thin-Film Device for Efficient Fermi-Level Tuning", ACS Nano **9**, 4050–4055 (2015).

[218] N. Koirala, M. Brahlek, M. Salehi, L. Wu, J. Dai, J. Waugh, T. Nummy, M.-G. Han, J. Moon, Y. Zhu, D. Dessau, W. Wu, N. P. Armitage, and S. Oh, "Record Surface State Mobility and Quantum Hall Effect in Topological Insulator Thin Films via Interface Engineering", Nano Letters **15**, 8245–8249 (2015).

[219] A. A. Taskin, H. F. Legg, F. Yang, S. Sasaki, Y. Kanai, K. Matsumoto, A. Rosch, and Y. Ando, "Planar Hall effect from the surface of topological insulators", Nature Communications **8**, 1340 (2017).

[220] M. Lang, L. He, F. Xiu, X. Yu, J. Tang, Y. Wang, X. Kou, W. Jiang, A. V. Fedorov, and K. L. Wang, "Revelation of Topological Surface States in $\mathrm{Bi}_2\mathrm{Se}_3$ Thin Films by In Situ Al Passivation", ACS Nano **6**, 295–302 (2012).

[221] P Ngabonziza, R Heimbuch, N de Jong, R. A. Klaassen, M. P. Stehno, M Snelder, A Solmaz, S. V. Ramankutty, E Frantzeskakis, E van Heumen, G Koster, M. S. Golden, H. J. W. Zandvliet, and A Brinkman, "In situ spectroscopy of intrinsic $\mathrm{Bi}_2\mathrm{Te}_3$ topological insulator thin films and impact of extrinsic defects", Phys. Rev. B **92**, 35405 (2015).

[222] F. Xiu, L. He, Y. Wang, L. Cheng, L.-t. Chang, M. Lang, G. Huang, X. Kou, Y. Zhou, X. Jiang, Z. Chen, J. Zou, A. Shailos, and K. L. Wang, "Manipulating surface states in topological insulator nanoribbons", Nature Nanotechnology **6**, 216–221 (2011).

[223] V. E. Sacksteder and Q. Wu, "Quantum interference effects in topological nanowires in a longitudinal magnetic field", Phys. Rev. B **94**, 205424 (2016).

[224] J Dufouleur, L Veyrat, A Teichgräber, S Neuhaus, C Nowka, S Hampel, J Cayssol, J Schumann, B Eichler, O. G. Schmidt, B Büchner, and R Giraud, "Quasiballistic Transport of Dirac Fermions in a Bi_2Se_3 Nanowire", Phys. Rev. Lett. **110**, 186806 (2013).

[225] B Al'tshuler, A Aronov, and B Spivak, "The Aharonov-Bohm Effect in Disordered Conductors", JETP Lett. **33**, 94 (1981).

[226] K Flensberg, J. B. Hansen, and M Octavio, "Subharmonic energy-gap structure in superconducting weak links", Phys. Rev. B **38**, 8707–8711 (1988).

[227] D. Laroche, D. Bouman, D. J. van Woerkom, A. Proutski, C. Murthy, D. I. Pikulin, C. Nayak, R. J. J. van Gulik, J. Nygård, P. Krogstrup, L. P. Kouwenhoven, and A. Geresdi, "Observation of the 4π-periodic Josephson effect in indium arsenide nanowires", Nature Communications **10**, 245 (2019).

[228] K. Ueda, S. Matsuo, H. Kamata, Y. Sato, Y. Takeshige, K. Li, L. Samuelson, H. Xu, and S. Tarucha, "Evidence of half-integer Shapiro steps originated from nonsinusoidal current phase relation in a short ballistic InAs nanowire Josephson junction", Phys. Rev. Research **2**, 33435 (2020).

[229] A. V. Galaktionov and A. D. Zaikin, "Quantum interference and supercurrent in multiple-barrier proximity structures", Phys. Rev. B **65**, 184507 (2002).

[230] F. Ando, Y. Miyasaka, T. Li, J. Ishizuka, T. Arakawa, Y. Shiota, T. Moriyama, Y. Yanase, and T. Ono, "Observation of superconducting diode effect", Nature **584**, 373–376 (2020).

[231] H. Isobe, S.-Y. Xu, and L. Fu, "High-frequency rectification via chiral Bloch electrons", Sci. Adv. **6**, eaay2497 (2020).

[232] K Yasuda, A Tsukazaki, R Yoshimi, K. S. Takahashi, M Kawasaki, and Y Tokura, "Large Unidirectional Magnetoresistance in a Magnetic Topological Insulator", Phys. Rev. Lett. **117**, 127202 (2016).

[233] K. Yasuda, T. Morimoto, R. Yoshimi, M. Mogi, A. Tsukazaki, M. Kawamura, K. S. Takahashi, M. Kawasaki, N. Nagaosa, and Y. Tokura, "Large non-reciprocal charge transport mediated by quantum anomalous Hall edge states", Nature Nanotechnology **15**, 831–835 (2020).

[234] C. Baumgartner, L. Fuchs, A. Costa, S. Reinhardt, S. Gronin, G. C. Gardner, T. Lindemann, M. J. Manfra, P. E. Faria Junior, D. Kochan, J. Fabian, N. Paradiso, and C. Strunk, "Supercurrent rectification and magnetochiral effects in symmetric Josephson junctions", Nature Nanotechnology **17**, 39–44 (2021).

[235] K. Yasuda, H. Yasuda, T. Liang, R. Yoshimi, A. Tsukazaki, K. S. Takahashi, N. Nagaosa, M. Kawasaki, and Y. Tokura, "Nonreciprocal charge transport at topological insulator/superconductor interface", Nat. Commun. **10**, 2734 (2019).

[236] H. Wu, Y. Wang, Y. Xu, P. K. Sivakumar, C. Pasco, U. Filippozzi, S. S. P. Parkin, Y.-J. Zeng, T. McQueen, and M. N. Ali, "The field-free Josephson diode in a van der Waals heterostructure", Nature **604**, 653–656 (2022).

[237] R. S. Souto, M. Leijnse, and C. Schrade, "Josephson Diode Effect in Supercurrent Interferometers", Phys. Rev. Lett. **129**, 267702 (2022).

[238] M. Gupta, G. V. Graziano, M. Pendharkar, J. T. Dong, C. P. Dempsey, C. Palmstrøm, and V. S. Pribiag, "Gate-tunable superconducting diode effect in a three-terminal Josephson device", Nature Communications **14**, 3078 (2023).

[239] C. Ciaccia, R. Haller, A. C. C. Drachmann, T. Lindemann, M. J. Manfra, C. Schrade, and C. Schönenberger, "Gate-tunable Josephson diode in proximitized InAs supercurrent interferometers", Physical Review Research **5** (2023).

[240] S. Reinhardt, T. Ascherl, A. Costa, J. Berger, S. Gronin, G. C. Gardner, T. Lindemann, M. J. Manfra, J. Fabian, D. Kochan, C. Strunk, and N. Paradiso, "Link between supercurrent diode and anomalous Josephson effect revealed by gate-controlled interferometry", arXiv:2308.01061 (2023).

[241] V Krstić, S Roth, M Burghard, K Kern, and G. Rikken, "Magneto-chiral anisotropy in charge transport through single-walled carbon nanotubes", The Journal of chemical physics **117**, 11315–11319 (2002).

[242] S. S. L. Zhang and G. Vignale, "Theory of bilinear magneto-electric resistance from topological-insulator surface states", in Spintronics xi, Vol. 10732, SPIE Conference Series (2018), p. 1073215.

[243] M Inglot, V. K. Dugaev, E. Y. Sherman, and J Barnaś, "Enhanced photogalvanic effect in graphene due to Rashba spin-orbit coupling", Phys. Rev. B **91**, 195428 (2015).

[244] Y. Zhang, T. Holder, H. Ishizuka, F. de Juan, N. Nagaosa, C. Felser, and B. Yan, "Switchable magnetic bulk photovoltaic effect in the two-dimensional magnet CrI_3", Nat. Commun. **10**, 3783 (2019).

[245] P. Bhalla, A. H. MacDonald, and D. Culcer, "Resonant Photovoltaic Effect in Doped Magnetic Semiconductors", Phys. Rev. Lett. **124**, 87402 (2020).

[246] P. Středa, P. and Šeba, "Antisymmetric Spin Filtering in One-Dimensional Electron Systems with Uniform Spin-Orbit Coupling", Phys. Rev. Lett. **90**, 256601 (2003).

[247] B. Braunecker, G. I. Japaridze, J. Klinovaja, and D. Loss, "Spin-selective Peierls transition in interacting one-dimensional conductors with spin-orbit interaction", Phys. Rev. B **82**, 45127 (2010).

[248] H Köhler, "Anisotropic g-Factor of the Conduction Electrons in Bi_2Te_3", Phys. Status Solidi (B) **75**, 127–136 (1976).

[249] A. A. Taskin, H. F. Legg, F. Yang, S. Sasaki, Y. Kanai, K. Matsumoto, A. Rosch, and Y. Ando, "Planar Hall effect from the surface of topological insulators", Nature Communications **8**, 1340 (2017).

[250] F. Pop, P. Auban-Senzier, E. Canadell, G. L. J. A. Rikken, and N. Avarvari, "Electrical magnetochiral anisotropy in a bulk chiral molecular conductor", Nat. Commun. **5**, 3757 (2014).

[251] P. He, S. M. Walker, S. S.-L. Zhang, F. Y. Bruno, M. S. Bahramy, J. M. Lee, R. Ramaswamy, K. Cai, O. Heinonen, G. Vignale, F Baumberger, and H. Yang, "Observation of Out-of-Plane Spin Texture in a $SrTiO_3(111)$ Two-Dimensional Electron Gas", Phys. Rev. Lett. **120**, 266802 (2018).

[252] "Nonlinear magnetotransport shaped by Fermi surface topology and convexity", Nat. Commun. **10**, 1290 (2019).

[253] T Guillet, C Zucchetti, Q Barbedienne, A Marty, G Isella, L Cagnon, C Vergnaud, H Jaffrès, N Reyren, J.-M. George, A Fert, and M Jamet, "Observation of Large Unidirectional Rashba Magnetoresistance in Ge(111)", Phys. Rev. Lett. **124**, 27201 (2020).

[254] R. Wakatsuki, Y. Saito, S. Hoshino, Y. M. Itahashi, T. Ideue, M. Ezawa, Y. Iwasa, and N. Nagaosa, "Nonreciprocal charge transport in noncentrosymmetric superconductors", Sci. Adv. **3**, e1602390 (2017).

[255] F Qin, W Shi, T Ideue, M Yoshida, A Zak, R Tenne, T Kikitsu, D Inoue, D Hashizume, and Y Iwasa, "Superconductivity in a chiral nanotube", Nat. Commun. **8**, 14465 (2017).

[256] J Lustikova, Y Shiomi, N Yokoi, N Kabeya, N Kimura, K Ienaga, S Kaneko, S Okuma, S Takahashi, and E Saitoh, "Vortex rectenna powered by environmental fluctuations", Nat. Commun. **9**, 4922 (2018).

[257] C. O. Avci, J. Mendil, G. S. D. Beach, and P. Gambardella, "Origins of the Unidirectional Spin Hall Magnetoresistance in Metallic Bilayers", Phys. Rev. Lett. **121**, 87207 (2018).

[258] C. O. Avci, K. Garello, A. Ghosh, M. Gabureac, S. F. Alvarado, and P. Gambardella, "Unidirectional spin Hall magnetoresistance in ferromagnet/normal metal bilayers", Nat. Phys. **11**, 570–575 (2015).

[259] T. Li, S. Kim, S.-J. Lee, S.-W. Lee, T. Koyama, D. Chiba, T. Moriyama, K.-J. Lee, K.-J. Kim, and T. Ono, "Origin of threshold current density for asymmetric magnetoresistance in Pt/Py bilayers", Appl. Phys. Express **10**, 73001 (2017).

[260] Y. Yin, D.-S. Han, M. C. H. de Jong, R. Lavrijsen, R. A. Duine, H. J. M. Swagten, and B. Koopmans, "Thickness dependence of unidirectional spin-Hall magnetoresistance in metallic bilayers", Appl. Phys. Lett. **111**, 232405 (2017).

[261] C Lidig, J Cramer, L. Weißhoff, T. Thomas, T Kessler, M Kläui, and M Jourdan, "Unidirectional Spin Hall Magnetoresistance as a Tool for Probing the Interfacial Spin Polarization of Co_2MnSi", Physical Review Applied **11**, 044039 (2019).

[262] K. Olejník, V Novák, J Wunderlich, and T Jungwirth, "Electrical detection of magnetization reversal without auxiliary magnets", Physical Review B **91**, 180402 (2015).

[263] T Yokouchi, N Kanazawa, A Kikkawa, D Morikawa, K Shibata, T Arima, Y Taguchi, F Kagawa, and Y Tokura, "Electrical magnetochiral effect induced by chiral spin fluctuations", Nat. Commun. **8**, 866 (2017).

[264] Y. Lv, J. Kally, D. Zhang, J. S. Lee, M. Jamali, N. Samarth, and J.-P. Wang, "Unidirectional spin-Hall and Rashba-Edelstein magnetoresistance in topological insulator-ferromagnet layer heterostructures", Nat. Commun. **9**, 111 (2018).

[265] Y. Fan, Q. Shao, L. Pan, X. Che, Q. He, G. Yin, C. Zheng, G. Yu, T. Nie, M. R. Masir, A. H. MacDonald, and K. L. Wang, "Unidirectional Magneto-Resistance in Modulation-Doped Magnetic Topological Insulators", Nano Lett. **19**, 692–698 (2019).

[266] R. Aoki, Y. Kousaka, and Y. Togawa, "Anomalous Nonreciprocal Electrical Transport on Chiral Magnetic Order", Phys. Rev. Lett. **122**, 57206 (2019).

[267] M. Bai, F. Yang, M. Luysberg, J. Feng, A. Bliesener, G. Lippertz, A. A. Taskin, J. Mayer, and Y. Ando, "Novel self-epitaxy for inducing superconductivity in the topological insulator $(\mathrm{Bi}_{1-x}\mathrm{Sb}_x)_2\mathrm{Te}_3$", Phys. Rev. Materials **4**, 94801 (2020).

[268] S Vaitiekėnas, G. W. Winkler, B van Heck, T Karzig, M.-T. Deng, K Flensberg, L. I. Glazman, C Nayak, P Krogstrup, R. M. Lutchyn, and C. M. Marcus, "Flux-induced topological superconductivity in full-shell nanowires", Science **367**, eaav3392 (2020).

DATA AVAILABILITY

Samples measured during preparation of this work are stored in the group's laboratory and recipes for growth and fabrication are given in the text and publications. The collected data is stored on work-group internal hardware and backed-up by central data management.

LIST OF PUBLICATIONS

1. **Top-Down Fabrication of Bulk-Insulating Topological Insulator Nanowires for Quantum Devices**

   Rößler, M., Fan, D., Münning, F., Legg, H.F., Bliesener, A., Lippertz, G., Uday, A., Yazdanpanah, R., Feng, J., Taskin, A.A., Ando, Y.
   Nano Letters 23 (7), 2846-2853 (2023).

2. **Giant magnetochiral anisotropy from quantum-confined surface states of topological insulator nanowires.**

   Rößler, M.*, Legg, H.F.*, Münning, F., Fan, D., Breunig, O., Bliesener, A., Lippertz, G., Uday, A., Taskin, A., Loss, D., Klinovaja, J., Ando, Y.
   Nature Nanotechnology 17, 696–700 (2022).

3. **Quantum confinement of the Dirac surface states in topological-insulator nanowires.**

   Münning, F.*, Breunig, O.*, Legg, H.F.*, Roitsch, S., Fan, D., **Rößler, M.**, Rosch, A., Ando, Y.
   Nature Communications 12, 1038 (2021).

   *Equal contribution

ACKNOWLEDGEMENTS

Studying physics wasn't something that came to me naturally but something that I slowly gravitated to because, with much reverence, I was fascinated by it from an early age on. I share Christopher Nolan's vision in 'The Prestige': Physics, even more so quantum physics, is the closest one can come to real magic, something which I was practicing since the age of six. That is why pursuing a PhD in physics on exploring the properties of particles and materials frequently described as 'peculiar' is a dream come true. Exerting the right balance of detail-work and vision, following others and trusting one's own independent belief is what enabled these results and is what I am grateful for to have learned from incredible supervisors, colleagues and friends along this journey. After all, this is what science is about, being allowed to learn and to explore ideas that one deems fascinating, in a sportive way, with an educated independence and the hope to help to create a better future. Both the latter are achieved only by hard work and the grace of the ones acknowledged in the following.

Foremost I am most grateful to Ando-sensei, for your guidance, example of work ethics, high standards and open way of sharing your views. All that accounts for the majority of my growth in the past years and shaped my understanding of scientific eminence for the rest of my life. Also, I would like to thank the other members of the examination committee, Prof. Erwann Bocquillon and Prof. Alex Altland. I felt encouraged and supported by your always welcoming kindness and am truly honored to have such experts give their blessings to my work.

Already on the first day, joining Ando-lab felt like the start of a very important chapter of my life and it was an honor not only due to the work we could do, but more so because of the people involved:

Dingxun, your kind, supportive and knowledgeable nature to me made us a Postdoc-PhD dream team in which I felt you are the older stepbrother I never had. Your backing enabled this work to take off, so may bonds forged in the cleanroom, a place we both felt home in, never break. In this context, I couldn't had wished for more support on our projects than received from Félix and even

more so Nicolas. I always looked forward to your 'I have a question' and our discussions in what we called a 'Team etched TINW', so I immensely enjoyed our reunion in Vegas, partying with the big shots.

A broader family I am indebted to is 'Team Transport'. Felix, I couldn't have done it without your skills with the Matrix as well as your fine taste in wordplay and I'll always be open to your crazy new ideas. Also, a big thanks to Oli, for being a fundamental constant in this lab and for somehow essentially running almost everything. Junya, your experience and the too infrequently tapped into treasures of code in your vast python libraries made me re-evaluate my work many times and I am grateful for your always critical comments. Jakob, I immensely enjoyed you joining the lab's roster and apart from your always warm and welcoming support your understatement in the face of your outstanding skills is setting a high bar to what it means to be a Postdoc. Furthermore, many thanks for your guidance in Honkong and at late nights in the low-temperature lab Mengmeng, for being such a good friend Pooji, for your strong leadership on the lab spirit front Luc, and for many cheerful memories also beyond Halligalli and the occasional Keks-Pausen, Ella.

A particularly dear 'thank you' belongs to my second (in-law?) family 'Team-MBE'. To only name a few reasons apart from being beloved friends, to Andrea for the best photographs, MBE1 and MBE2 films as well as trailblazing what it means to be a PhD in Ando-lab, to Gertjan for always doing the most reliable and precise work as well as for relentless belief in my beard product line (at least giving me the feeling), and to Anju for always brightening up the lab and the (proclaimed) best BST film of my life. Thanks to Alexey for the countless times you without hesitation or time constraint made the effort to share your unfathomable experience on various aspects of science and thanks to Roozbeh for living up to a legacy of BST growth.

Ando-lab thrives from its diversity, and many others contribute to make it a place I call home. Many thanks to Sweta for inspiring everyone with your uncommon interpretation of scientific independence as well as for providing an always reliable cookie lifeline, and to Jens for an always open door for an exchange on science and dark humour. Chris, Yongjian, the calm and kind seniority with which you seem to approach the chaotic waters of academia leaves me with humility and I look forward to see you continue to thrive in independence. In addition to these colleagues, many more current and former fine lab members contributed

to my great experience in our lab. Jonas, Linh, Adrian, Cornelius, Rich, Elmore, Michel, Rafael and also Lionel, Zhiwei, Subhamoy and especially the wise Fan, all of you helped or inspired me many times for which I will dearly remember you.

This work is also embossed by the one-man army we call 'Theory support', Henry, on whose leggwork not only I could always count, a debt no whiskey in the world is expensive enough to repay for. May you share an appropriately aged one with Prof. Daniel Loss and Prof. Jelena Klinovaja to convey my gratitude.

In PH2, I am particularly grateful to Christoph Grams, Daniel Rosenbach as well as the ML4Q and CRC staff for the always kind support, and to Timur, Lucy and Harald to have covered our back so we could focus on science. Outside Cologne, I wholeheartedly appreciated our sportive and yet supportive competition with the teams in Jülich lead by Prof. Thomas Schäpers and Peter Schüffelgen.

Widening the scope, I also want to acknowledge my roots and am grateful for the not forgotten teachings, friendships and memes of my former scientific home at Hendrik Bluhm's lab, JARA-IQI RWTH Aachen. You shaped my understanding and first steps of what it means to be a physicist Hendrik, and Rob McNeil and Matthias Künne of what it means to excel in nano-fabrication. Benni Joecker, Jan Klos, Daniel Jirovec, Patrick Bethke, Tim Botzem, Michi Mol, Pascal Cerfontaine, Arne Hollmann and Tim Leonhardt, also you I thank dearly for your support and comradeship.

Most importantly, therefore at last, this work is dedicated to the ones I love, my friends and my family. Everyone who took part knows, and since you are too many to list appropriately, a humble: Danke für deine Anteilnahme und Unterstützung - auch du hast diese Arbeit ermöglicht, und das hat mir viel bedeutet.

STATEMENT OF AUTHORSHIP

Hiermit versichere ich an Eides statt, dass ich die vorliegende Dissertation selbstständig und ohne die Benutzung anderer als der angegebenen Hilfsmittel und Literatur angefertigt habe. Alle Stellen, die wörtlich oder sinngemäß aus veröffentlichten und nicht veröffentlichten Werken dem Wortlaut oder dem Sinn nach entnommen wurden, sind als solche kenntlich gemacht. Ich versichere an Eides statt, dass diese Dissertation noch keiner anderen Fakultät oder Universität zur Prüfung vorgelegen hat; dass sie - abgesehen von unten angegebenen Teilpublikationen und eingebundenen Artikeln und Manu-skripten - noch nicht veröffentlicht worden ist sowie, dass ich eine Veröffentlichung der Dissertation vor Abschluss der Promotion nicht ohne Genehmigung des Promotionsausschusses vornehmen werde. Die Bestimmungen dieser Ordnung sind mir bekannt. Darüber hinaus erkläre ich hiermit, dass ich die Ordnung zur Sicherung guter wissenschaftlicher Praxis und zum Umgang mit wissenschaftlichem Fehlverhalten der Universität zu Köln gelesen und sie bei der Durchführung der Dissertation zugrundeliegenden Arbeiten und der schriftlich verfassten Dissertation beachtet habe und verpflichte mich hiermit, die dort genannten Vorgaben bei allen wissenschaftlichen Tätigkeiten zu beachten und umzusetzen. Ich versichere, dass die eingereichte elektronische Fassung der eingereichten Druckfassung vollständig entspricht.

Teilpublikationen (*Equal contribution):

1. **Rößler, M.***, Legg, H.F.*, Münning, F., Fan, D., Breunig, O., Bliesener, A., Lippertz, G., Uday, A., Taskin, A., Loss, D., Klinovaja, J., Ando, Y. Giant magnetochiral anisotropy from quantum-confined surface states of topological insulator nanowires. Nature Nanotechnology 17, 696–700 (2022).
2. **Rößler, M.**, Fan, D., Münning, F., Legg, H.F., Bliesener, A., Lippertz, G., Uday, A., Yazdanpanah, R., Feng, J., Taskin, A.A., Ando, Y. Top-Down Fabrication of Bulk-Insulating Topological Insulator Nanowires for Quantum Devices. Nano Letters 23, 7, 2846-2853 (2023).

Datum, Name und Unterschrift:
Matthias Rößler, 25.09.2023